Experimental and theoretical investigation on road pavements and materials through ground-penetrating radar

ROMA TRE
UNIVERSITÀ DEGLI STUDI

SCUOLA DOTTORALE IN INGEGNERIA
SEZIONE SCIENZE DELL'INGEGNERIA CIVILE

CICLO DEL CORSO DI DOTTORATO
XXVI

Experimental and theoretical investigation on road pavements and materials through ground-penetrating radar

Dottorando:
Fabio Tosti

Docente Guida:
Prof. dott. ing. Andrea Benedetto

Coordinatore:
Prof. dott. ing. Aldo Fiori

Collana delle tesi di Dottorato di Ricerca
In Scienze dell'Ingegneria Civile
Università degli Studi Roma Tre
Tesi n° 48

To the memory of my mother

Sommario

L’utilizzo delle tecnologie non-distruttive (NDT) nel settore dell’ingegneria delle infrastrutture viarie è in continua e progressiva ascesa, e la necessità di sviluppare ed adottare nuovi standard di misurazione, basati sulla conoscenza approfondita degli strumenti di indagine e dei materiali costruttivi, per la verifica ed il monitoraggio avanzati dello stato di degrado e delle caratteristiche prestazionali delle pavimentazioni, sta sempre più emergendo. Una serie di fattori di varia natura ha contribuito alla crescita della domanda in questo ambito. Principalmente, il progresso tecnologico, sia hardware che software, degli strumenti di misura, l’intrinseca bassa rappresentatività e l’elevata intrusività delle tradizionali tecniche di controllo e monitoraggio, e gli effetti dell’attuale crisi economica che colpisce oramai da più di un lustro le economie di tutto il globo, hanno orientato ricercatori, professionisti, ed utilizzatori in genere, ad un impiego più diffuso ed efficace di tecnologie non-distruttive, stimolando anche l’interesse di governi ed enti locali per la notevole capacità di raccogliere un numero elevato di informazioni in tempi relativamente molto brevi.

In questo quadro generale, il ground-penetrating radar (GPR) o georadar può ragionevolmente essere ritenuto come la tecnologia non-distruttiva con maggiori potenzialità di utilizzo in molti settori scientifici e campi di applicazione, particolarmente in quello stradale, in virtù della sua elevata capacità di rilevare e, in parte, quantificare l’assetto della struttura profonda di una pavimentazione.

La maggior parte delle applicazioni radar in ambito stradale riguarda la stima degli spessori degli strati di pavimentazione e, più in generale, la valutazione delle sue caratteristiche geometriche profonde, che necessita in ogni caso del supporto di carotaggi per la calibrazione del sistema. Minor rilevo è stato invece dato negli anni alla possibilità di indagare le cause di degrado e le caratteristiche prestazionali di un’infrastruttura, in un’ottica di ottimizzazione delle strategie di nuova realizzazione, manutenzione e ripristino.

Il presente studio si pone come obiettivo principale quello di migliorare gli attuali processi di gestione e manutenzione delle pavimentazioni stradali, per prevenire fenomeni di ammaloramento e danno strutturale, anche ai fini del controllo della sicurezza di esercizio.

Più specificamente, sono state indagate quelle caratteristiche fisico-meccaniche critiche per lo sviluppo di situazioni di degrado nella pavimentazione. Per ognuna di queste grandezze sono stati calibrati dei modelli sperimentali alla scala di laboratorio, a cui è seguita una fase di validazione su scala reale per la definizione dei modelli finali. Inoltre, è stata analizzata l'efficacia di alcuni sistemi radar convenzionali e non, differenti per caratteristiche elettroniche e configurazione di indagine, e di varie tecniche di analisi del segnale.

Nel Capitolo 1 viene introdotto il problema relativo al monitoraggio delle pavimentazioni e dei materiali stradali, attraverso uno stato dell'arte sulle tecnologie non-distruttive e sull'impiego del GPR, con un dettaglio maggiore per utilizzi nel campo stradale.

Nel Capitolo 2 vengono trattati i princìpi della teoria elettromagnetica, su cui si fonda il funzionamento del radar. Con particolare attenzione vengono poi illustrati i fondamenti della teoria dello scattering alla Rayleigh, su cui si basa parte del presente studio.

Nel Capitolo 3 vengono esposti i risultati di un'indagine sperimentale per la stima del campo spaziale di umidità in un sottofondo. L'analisi ha previsto l'utilizzo di un sistema radar a trascinamento con antenne accoppiate a terra, avente frequenze centrali di indagine pari a 600 MHz e 1600 MHz. Sono state impiegate due tecniche di analisi del segnale: il metodo della riflettività superficiale è stato utilizzato per la stima del contenuto volumetrico di acqua nel sottosuolo attraverso la valutazione della permittività dielettrica relativa del mezzo indagato, e a sua volta implementata in un modello petrofisico di natura empirica; i valori dedotti sono stati quindi confrontati con le misure di umidità derivate localmente mediante sonde capacitive. L'applicazione del metodo di Rayleigh ha previsto invece la ricostruzione della struttura spaziale del campo di umidità nel dominio delle frequenze, confrontata dunque con quella valutata nel dominio del tempo attraverso il metodo della riflettività superficiale. I risultati hanno dimostrato come il GPR possa essere utilizzato efficacemente anche per misure di piccola scala (area di indagine ≤ 0.01 m^2), e come la tecnica dello scattering alla Rayleigh si riveli efficace per la stima del campo di umidità, senza bisogno di prelievi distruttivi per la calibrazione, o di leggi petrofisiche che richiedano la conoscenza del tipo di terreno da indagare.

Il Capitolo 4 è stato a sua volta dedicato alla indagine di un'ulteriore caratteristica fisica preminente per lo sviluppo di situazioni di degrado

strutturale negli strati portanti della pavimentazione, ovvero il contenuto di argilla. Analogamente all'approccio seguito per la stima dell'umidità, diversi strumenti radar e tecniche di analisi del segnale sono state tra di loro confrontate. La fase di sperimentazione in laboratorio ha previsto l'utilizzo di tre tipologie di materiale sciolto tipicamente utilizzato per la realizzazione degli strati profondi di pavimentazione. Tali materiali, classificabili all'interno dei gruppi A1, A2, e A3 della classifica AASHTO, sono stati progressivamente inquinati con crescenti percentuali di argilla comprese tra il 2% e il 25%, permettendo di studiare il fenomeno in un campo sufficientemente ampio. Due modelli di previsione sono stati sviluppati utilizzando informazioni nel dominio delle frequenze, ottenute attraverso la tecnica dello scattering alla Rayleigh, e informazioni sulla misura della permittività dei campioni di suolo attraverso l'uso di un sistema radar stepped frequency continuous-wave (SFCW) e di tecniche di analisi basate sull'inversione dei dati misurati nel dominio delle frequenze. I risultati hanno permesso di ottenere utili indicazioni sul tipo di tecnica di analisi e sulla tipologia di sistema radar più idonei da utilizzare in funzione della natura del terreno da studiare e dei quantitativi di argilla attesi.

Nel Capitolo 5 viene descritta la possibilità di derivare informazioni sulle caratteristiche di resistenza e deformazione di una pavimentazione stradale a partire dalle proprietà dielettriche. In particolare, vengono presentati due studi volti ad indagare il fenomeno sugli strati non legati e sui terreni di sottofondo, e sugli strati legati in conglomerato bituminoso. Entrambi i modelli di previsione si sono rivelati validi, restituendo valori di modulo elastico delle strutture indagate di buona approssimazione rispetto al dato misurato con strumentazione light falling weight deflectometer (LFWD).

Il Capitolo 6 contiene le conclusioni del lavoro e le raccomandazioni generali emerse dall'analisi dei risultati ottenuti.

Nell'Appendice A, sono descritti gli strumenti radar utilizzati per le attività svolte nell'ambito del Dottorato di Ricerca.

Abstract

Ground-penetrating radar (GPR) is being increasingly used over the last years in a wide range of applications, due to its flexibility and high potential to provide characterization and imaging of structures and materials. Overall, several reasons are contributing to increase the demand for the use of this tool and non-destructive testing techniques (NDTs) in general. Amongst all, it is worth citing technological advances of both hardware and software elements, an intrinsic lower significance of measurements provided by traditional monitoring techniques along with their greater invasiveness in measuring processes and, last but not least, the impacts of Global Economic Crisis on the use of economic resources affecting for years countries worldwide. The combination of such factors has led the interest of several skill profiles spanning from researchers, practitioners and end-users in general, and focused the attention of governments and local authorities on the high capabilities to gather a large amount of information in a relatively short time of surveying.

In the field of pavement engineering, GPR has been used since the early 1980s mostly focusing on the geometrical characterization of road structure, by evaluating layer thicknesses. Minor care has been given to the analysis of the main causes of damage and performance properties of pavements, in order to improve management of infrastructural asset through effective and efficient maintenance and rehabilitation actions, as well as to provide best conditions in design of new roads.

In that regard, this thesis is aimed to give a useful contribution also in the perspective of road safety issues by improving current processes of management and maintenance of road asset, along with the design of new roads, and provide effective support for the application and practical use of the tools described. Efforts have been spent in order to detect and quantify those physical and strength characteristics of road materials and subgrade soils that are relevant causes of damage, such that an effective planning of supporting actions for maintenance, rehabilitation and design of new roads may be timely performed.

Three main topics are addressed, namely: *i)* the evaluation of moisture spatial field in subgrade soils through a self-consistent frequency-based technique and the analysis of radar support scale in small-scale

measurements of water content; *ii)* the potential to detect and quantify clay content in load-bearing layers and subgrade soils through different GPR tools and signal processing techniques, and *iii)* the possibility to infer strength and deformation characteristics of both bound, unbound pavement structures, and subgrade soils from their electric properties.
The results are encouraging for applications in the field of pavement engineering.

Contents

List of Figures

List of Tables

List of Symbols

The following list shows the key symbols used in the Chapters of this thesis.

A	*area or Rayleigh scattering method regression coefficient or signal amplitude*
a	*structural layer coefficient or linear variation rate of σ(f)*
$a(\omega)$	*incident field*
$\vec{B}$	*magnetic field density*
B	*Rayleigh scattering method regression coefficient*
b	*index (model regression parameter)*
$\mathbf{b}$	*parameter vector*
$b(\omega)$	*backscattered field*
c	*speed of light in free space or index (model regression parameter)*
$\vec{D}$	*electric flux density*
d	*distance or diameter*
E	*elastic modulus*
$\vec{E}$	*electrical field intensity*
$E_x(\omega)$	*x-directed electric field at the field point*
e	*void ratio*
f	*frequency or function () or volume fraction*
f_P	*frequency peak of the GPR signal spectrum*

$G_{xx}^{\uparrow}(\omega)$	*layered medium Green's function*
$\boldsymbol{G}_{\boldsymbol{xx}}^{*\uparrow}$	*vector accounting for the observed Green's functions*
$\boldsymbol{G}_{\boldsymbol{xx}}^{\uparrow}$	*vector accounting for the simulated Green's functions*
$g_{xx}^{\uparrow}$	*inverse Fourier transform of the measured and modeled responses in the frequency domain*
h	*layer thickness*
I	*intensity of the electromagnetic wave*
i	*observations (index)*
$\vec{J}$	*total current density*
j	*number of layers*
$J_x(\omega)$	*unit-strength x-directed electric source at the source point*
k	*index (model regression parameter)*
m	*layer drainage coefficient*
n	*index of refraction or number of measurements or observables or porosity*
P	*percent passing sieve size*
p	*homogenization variable*
Q	*quality factor*
R	*correlation coefficient or distance of the observer to the particle or reflection coefficient*
R^2	*coefficient of determination*
$R_i(\omega)$	*antenna global reflection coefficient in free space*

$R_s(\omega)$	*global reflection coefficient for the field incident from the layered medium onto the field point*
r	*radius*
$S_{11}(\omega)$	*raw radar signal*
$T_i(\omega)$	*global transmission coefficient for fields incident from the radar reference plane onto the point source*
$T_s(\omega)$	*global transmission coefficient for fields incident from the field point onto the radar reference plane*
t	*time*
v	*EM wave propagation velocity in the medium*
w	*gravimetric water content*
w_L	*liquidity limit*
w_S	*shrinkage limit*
x	*general variable or scattering size parameter or x-distance*
y	*y-distance*
z	*z-distance*
α	*attenuation constant or dielectric geometric factor or dielectric parameter*
β	*index (model regression parameter) or phase constant*
Γ	*reflection coefficient*
δ	*deflection or loss angle*
Δ	*difference*
ε	*complex dielectric permittivity*

ε'	*real part of dielectric permittivity*
ε''	*imaginary part of dielectric permittivity*
ε^*	*complex apparent permittivity*
ε_0	*dielectric permittivity of free space*
ε_r	*dieletric permittivity of a multi-phase medium*
ζ	*amplification coefficient (model regression parameter)*
η	*amplification coefficient (model regression parameter)*
θ	*angle of scattering or bulk stress or volumetric water content*
ι	*amplitude scale coefficient (model regression parameter)*
κ	*complex wave number*
λ	*signal wavelength*
μ	*index (model regression parameter) or magnetic permeability or mean value of a distribution*
μ_0	*magnetic permeability of free space*
ν	*Poisson's ratio*
ϕ	*porosity*
π	*3.1416 or index (model regression parameter)*
ρ_{bulk}	*bulk density*
ρ_s	*particle density*
σ	*electrical conductivity or standard deviation of a distribution or stress*
τ	*index (model regression parameter) or relaxation time*

$\varphi(\mathbf{b})$	*objective function minimizing the parameter vector* **b**
χ	*amplitude-strength interaction coefficient (model regression parameter)*
ω	*angular frequency or index (model regression parameter)*

List of Acronyms and Abbreviations

The following list shows the acronyms and abbreviations used in the Chapters of this thesis.

2-D	*two dimensional*
3-D	*three dimensional*
AASHTO	*American Association of State Highway and Transportation Officials*
AVHRR	*advanced very high-resolution radiometer*
ADC	*digital-to-analog converter*
ASTM	*American Society for Testing and Materials*
CBR	*California bearing ratio*
CRIM	*complex refractive index model*
DCPT	*dynamic cone penetration test*
DEM	*differential effective medium*
DSP	*digital signal processor*
EM	*electromagnetic*
ER	*electrical resistivity*
EMA	*effective medium approximation*
EMI	*electromagnetic induction*
ER	*electrical resistivity*
FCC	*Federal Communications Commission*
FHWA	*Federal Highway Administration*

FFT	*fast Fourier Transform*
FT	*Fourier Transform*
FWD	*falling weight deflectometer*
GMCS	*global multilevel coordinate search*
GPR	*ground-penetrating radar*
GSSI	*Geophysical Survey Systems, Inc.*
HBD	*hemispherical butterfly dipole*
HF	*high frequency*
HP	*Hewlett Packard Company*
HH	*horizontal transmit and horizontal receive*
HMA	*hot mix asphalt*
IDS	*Ingegneria dei Sistemi S.p.A.*
IFFT	*inverse fast Fourier Transform*
IR	*infrared termography*
LFWD	*light falling weight deflectometer*
MF	*medium frequency or Multi Frequency*
NCHRP	*National Cooperative Highway Research Program*
NDE	*non-destructive evaluation*
NDT	*non-destructive technique*
PEC	*perfect electric conductor*
PI	*plasticity index*
PMS	*pavement management system*

PRF	*pulse repetition frequency*
RCS	*radar cross section*
RMSE	*root-mean-square error*
RX	*receiver*
RSA	*runway safety area*
SFCW	*stepped frequency continuous-wave*
SMA	*SubMiniature version A*
SN	*structural number*
SNR	*signal-to-noise-ratio*
TDR	*time domain reflectometry*
TEM	*transverse electromagnetic*
TX	*transmitter*
UWB	*ultra-wide bandwidth*
VDC	*Volts of direct current*
vis-NIR	*visible and near infrared*
VNA	*vector network analyzer*
VV	*vertical transmit and vertical receive*
W/C-ratio	*water/cement ratio*
WARR	*wide angle reflection refraction*

1. Introduction

1.1 Background

Over the last decades, road engineer activities are being increasingly focused on a proper management of infrastructural asset through effective and efficient maintenance actions, whereas demand for new constructions is slowly lowering. New construction is more demanded, generally speaking, in developing countries, where the need for elementary connections is stronger and expenditure priorities have been addressed to ensure basic services such as education, primary health care, water supply, local markets, and economic opportunities. In this regard, economic improvements come across putting the remote parts of the country more nearly upon the level with those in the neighborhood of the town. In a later stage and more recently, a rising decay in performing sustainable operations and maintenance of such new-built infrastructures is being observed and has become a growing issue in a large number of developing countries. Notwithstanding the shortcomings in the quality provided for maintenance processes of many infrastructures, maintenance is much more widespread in developed countries. Such emphasized difference cannot be uniquely due to a miss of funding. Technical issues related to the lack of both planning and information on the state of the road network should be also encountered.

Inherently, three main factors can address to sustainable maintenance systems namely *i)* the lack of economic resources, partly due to Global Economic Crisis impacts, that cause a lowering of new constructions demand; *ii)* well-distributed existing assets that meets the current requirements of mobility, and *iii)* progressive aging of existing assets.

Traditional inspection methods aimed at road infrastructures maintenance rely on the use of destructive techniques, such as coring, drilling or otherwise removing part of the structure to allow inner visual inspections (e.g., bridge deck inspections). Despite the high reliability of such techniques, they reveal as expensive and time-consuming. In addition, results can not be extended to long distances if compared to the large-scale extension usually required for road inspections.

Various non-destructive testing or evaluation (NDT/NDE) techniques have therefore been developed to enable more efficient assessment of road pavements and materials. The use of these techniques is of particular interest as they are faster, more cost efficient, can be performed in-situ, do not require remedial action, and can therefore be performed over a large

surface area. Nevertheless, because pavement structure can be represented as a multi-layered medium made from complex inhomogeneous material of which the properties and deterioration mechanisms depend on various parameters, much work is still required to improve the reliability of these non-destructive techniques.
In such context, new challenges may be faced on a more effective use of NDTs for cutting the cost of road maintenance and improving road conditions.

1.2 An overview of non-destructive methods

Detection and classification of defects and damages in the investigated media are the main aims of non-destructive testing or evaluation (NDT/NDE) methods [Maierhofer, 2010], while it is not always possible to quantify their magnitude. In particular, such aims include the determination of position and dimensions of heterogeneities, when changes in physical properties inside a homogeneous domain occur.
Over the recent years, repair and maintenance of constructions are being increasingly planned in a broad field of investigations through the use of these techniques.
The most common include concrete testing [Beutel et al., 2008; Dérobert et al., 2008; Dérobert and Berenger, 2010], inspection for ancient building safeguard [Ranalli et al., 2004; Solla et al., 2011], for land use purposes [Fenning and McCannt, 1995; Minet et al., 2011] and modern infrastructures safety, characterization of stone masonries [Binda et al., 1998, 2005; Diamanti and Redman, 2012; Helmerich et al., 2012], and bridge decks inspection [Benedetto et al., 2012b; Hugenschmidt and Mastrangelo, 2006; Saarenketo and Soderqvist, 1994]
In pavement engineering, driving safety is strictly related to pavement surface conditions [Tighe et al., 2000]. Cracks, potholes, and surface deformations generate sudden vertical accelerations on the vehicle tires, thereby decreasing the effective friction between tires and pavement. Such road damages are mostly related to a lowering of the bearing ratio of the load-bearing layers and subgrade soils [Diefenderfer et al., 2005]. Previous research has demonstrated that structural damage in road pavement depends on the moisture percentage in sub-asphalt courses [Benedetto and Pensa, 2007]. In particular, in the case of clayey unbound layers, the infiltration of water through the pavement causes the transport of plastic materials. This type of damage is classified as pumping and it is caused by several factors, such as inadequate compaction during construction, poor

mix design, high level of water table, and poor drainage [Al-Qadi et al., 2004; Tosti and Benedetto, 2012].
It is worth mentioning that any standard monitoring best practices should take into account for using NDT methods at the beginning of any engineering work, as a reference zero point in the life of structure. In this respect and in order to provide more effective monitoring, NDT methods can be applied repeatedly over longer periods.
Nevertheless, the normal practice provides the use of NDTs in different scenarios of conditions and age of the structure, as well as at different stages of its life, such that a full monitoring of the evolution of damages in the structure is partially possible.
As of today, conventional destructive methods are still needed for calibrating measurements by NDTs, although technological and research advances are more and more limiting the use of core samples [Maierhofer et al., 2010].
Overall, NDT methods can be classified into acoustic, optical, and electromagnetic (EM); this Section includes a brief description of each group.

1.2.1 Acoustic methods

Acoustic methods rely on the basic principle of sound waves propagation, wherein the variation in spatial resolution is a function of the frequency bandwidth of the emitted and detected signals. Traditionally, most of the applications provide the measure of the propagation time of impulses, although some researches are also focused on amplitude analyses. Amongst the most widely used acoustic methods we can cite acoustic and ultrasonic emissions, and impact echo [Beutel et al., 2008; Sidney, 2003].
In pavement engineering applications, several methods closely related to seismic are used for the testing of asphalt pavements. Falling weight deflectometer (FWD) has found widespread use over the last decades [American Society for Testing and Materials, 2005; Belt et al., 2006; National Cooperative Highway Research Program, 2008]. Basically, it applies a dynamic load through a circular plate that is lowered to the pavement surface. The echo from the pavement surface is then measured by sensors coupled with the surface. Therefore, the deflection bowl inferred from such echo is used to assess the structural condition and to identify weaknesses in any of the pavement layers. More recently, the light falling weight deflectometer (LFWD) was developed as a portable version of FWD to overcome accessibility problems of more cumbersome devices in

roads under construction [Alshibli et al., 2005]. The influence domain of deflections induced by LFWD in various types of subgrade soils under different instrument configurations has been recently analysed [Benedetto et al., 2012c]. Overall, high potential was found for LFWD-based models of ruts prediction in unpaved soils [Benedetto et al., 2014].

1.2.3 Optical methods

Many applications based on optical methods have been carried out in civil engineering since many years up to nowadays. Amongst the most common to be cited, photogrammetry has been widely used for topographical mapping, while the qualitative measurement of deformations is usually performed through laser scanner, laser vibrometer, and speckle interferometry [Maierhofer et al., 2010].
Optical methods have long been used in civil engineering for topographical mapping, for the quantitative measurement of deformations, e.g., using photogrammetry, laser scanner, laser vibrometer, speckle interferometry and stereography [Maierhofer et al., 2010]. Other methods are based on the record of direct images of the surface, e.g., digital photography, videoscopy, thermography [Gary, 2003], or rely on spectral analyses of the investigated object.

1.2.4 Electromagnetic methods

The analysis of propagation velocity of electromagnetic waves in materials is the main method that underlies electromagnetic techniques. Basically, EM methods rely on the transmission/reflection of short electromagnetic impulses, with antenna systems being capable to emit and detect them. Dielectric permittivity is the parameter that controls the propagation velocity and, in this respect, moisture content highly influences its value. As regards conductivity and dielectric losses, they affect the attenuation of the electromagnetic wave energy.
Amongst the most widespread EM methods, we can cite radar, electrical resistivity (ER), optical, termographic, potential field methods, and capacimetry.

1.2.5 Other methods

Infrared thermography (IR) is a broadly used technique that operates in the infrared range of the electromagnetic spectrum. Within this range, pictures or movies are recorded. IR allows to map the surface temperature of

pavement, so that defects influenced by temperature, such as delaminations or blisters can be detected.

1.3 Ground-penetrating radar: state of the art

Ground-penetrating radar was firstly used in traffic infrastructure surveys in the first half of 1970s by the Federal Highway Administration (FHWA) for testing in tunnel applications (for a review, see Morey [1998]). Later in 1985, the FHWA developed the first vehicle-mounted GPR system for highways. With regard to the rest of the world, Canada [Carter et al., 1992; Manning and Holt, 1983] and Scandinavia [Berg, 1984; Ulriksen, 1982] were other active areas where the instrument was tested among the late 1970s and the early 1980s. Following the inspections carried out in Finland in 1986 (for a review, see Saarenketo [1992]), the method started to become a routine survey in later years for both road design and rehabilitation purposes [Saarenketo and Scullion, 1994; Saarenketo and Scullion, 2000], even acting as a pavement design and quality control tool [Saarenketo, 1999; Scullion and Saarenketo, 1998]. In the following years between the late 1980s and early 1990s, research efforts were mostly devoted to pavement thickness measurements [Scullion et al., 1992; Maser, 1994], detection of voids underneath concrete slabs [Scullion et al., 1994], and deteriorated areas in bridge decks [Alongi et al., 1992]. Most of these surveys were carried out by using high-frequency air-launched antennas [e.g., Scullion et al., 1992]. In the second half of 1990s, the most widespread applications still included measurements of pavement layer thickness, detection of voids and bridge delamination, measurements of depth to steel dowels and depth to bedrock, detection of buried objects, asphalt stripping and scour around bridge support. In this regard, best results were achieved for thickness measurements, while poor results were obtained for void and asphalt stripping areas detections [Morey, 1998].

Starting from the 80s, GPR has been used in other parts of Europe such as UK, wherein research was mostly addressed to concrete structures [Alani et al., 2013, 2014; Millard et al., 1993] and pavement testing [Ballard, 1992, 1993; Daniels, 1996], France [Daniels, 1996], and the Netherlands [Hopman and Beuving, 2002], being pavement testing and thickness measurements the most common applications, respectively.

Nowadays, GPR can be considered as the most flexible geophysical engineering tool having the greatest number of applications in transportation engineering. Saarenketo [2009] has broadly divided GPR applications into four main categories namely *i)* surveys needed in design

of a new road, *ii)* surveys carried out for the rehabilitation design of an existing road, *iii)* quality control or quality assurance surveys on a road project, and *iv)* surveys carried out for pavement management systems [e.g., Al-Qadi and Lahouar, 2004; Al-Qadi et al., 2004; Alani et al., 2013, 2014; Benedetto, 2010; Benedetto, 2013; Benedetto and Pensa, 2007; Benedetto and Tosti 2013; Plati and Loizos, 2013; Saarenketo and Scullion, 2000]. Several types of information mostly concerning bound and unbound pavement structures, subgrade soils, and moisture contents can be provided by GPR. This Section includes a short description of the major applications carried out over the past years according to the type of layer and road materials.

1.3.1 Main road applications

1.3.1.1 Subgrade surveys

According to Saarenketo and Scullion [1994], three categories may be included in GPR-based subgrade surveys and site investigations namely *i)* new road alignment and site investigations, *ii)* strengthening and widening of an existing road, and *iii)* design of a new roadway alongside the existing road intended as a source of information. In all these cases, the application of GPR techniques varies, although the survey purpose is the same.

Within subgrade quality analyses, it is relatively easy to identify coarse gravel, grained gravel, sand, and glacial till soils from the GPR data [Saarenketo, 2009]. Good results have been also found for organic peat soils [Doolittle and Rebertus, 1988; Laamrani et al., 2013; Saarenketo et al., 1992; Ulriksen, 1982; van Dam et al., 2002].

Out of many research and application findings, it has been demonstrated how relatively good signal penetration can be achieved in silty soils.

On the contrary, one of the main issue is related to GPR-based surveys carried out on clayey soils. Mineralogy and clay content of soils are the main factors affecting penetration depth of the GPR signal. According to Saarenketo [2009], GPR signal penetration in Scandinavian clay soil areas is normally about 2 m, which is not enough for highway design purposes. Doolittle and Rebertus [1988] argued that a penetration depth of 5 m has been achieved in areas of Site Oxidic soils, while radar signals penetrated only 0.15 m in montmorillonitic soils. Other studies have been more recently carried out in laboratory environment to analyse the electromagnetic response of clayey soils in both dry and wet conditions [Benedetto, 2004; Benedetto, 2010, Patriarca et al. 2013; Saarenketo,

1998], although few efforts have been spent to quantify clay content in soils [e.g., Jacobsen and Schjønning, 1993].
By using GPR data, it is also possible to determine many soil types by exploiting their soil-specific geological structure, dielectric, and electrical conductivity properties [e.g., Benedetto and Benedetto, 2002; Saarenketo, 1998]. A valuable support to GPR data for locating the depth of overburden and bedrock is given by FWD survey data, through the interpretation of FWD deflection bowl shape and FWD backcalculation algorithms [Saarenketo and Scullion, 2000].
Moisture evaluation in subgrade soils is another important issue due to the high influence exerted by water on their strength and deformation properties. Outcomes from research argued that when calculating soil water content or soil type from dielectrics of subgrade soil layers two main issues should be taken into account namely *i)* the need of ground-truth data to confirm the GPR interpretation, and *ii)* the frequency-dependence of soil dielectric permittivity. In this regard and in order to provide more effective detection of moisture and its distribution in subgrade soil layers, research efforts should be devoted to improve analyses in the GPR frequency domain. Thus, more self-consistent methods and accurate EM behavior characterizations of a wider range of road materials over a relevant frequency bandwidth could be developed, also by using different radar systems.

1.3.1.2 Unbound pavement layers surveys

Unbound pavement structures are located between the subgrade soil and top bound layers. Traditionally, materials used for unbound pavement structure are crushed gravel, crushed hard rock, ballast or macadam and natural soils, such as gravel and sand poorly sensitive to water infiltration and frost effects. Most of the applications related to unbound layer surveys have been focused on thicknesses measurement [Al-Qadi et al., 2002; Loizos and Plati, 2007b; Maser, 2002a] and moisture evaluation [Al-Qadi et al., 2004; Muller, 2012]. At present, many issues remain unexplored or partially addressed. Clay pumping in sub-base layer is one of the main cause of pavement structural damaging, as the upward passage of the smallest clay slurry particles from the subgrade reduces tensile strength of load-bearing layers. In this regard and similarly to the case of subgrade soils, more efforts should be devoted on the possibility to *i)* detect clay, and *ii)* estimate its content in compacted loose material. In addition, strength and deformation properties of unbound pavement materials have not been

likewise investigated up to nowadays. A dynamic cone penetration test (DCPT), dynamic triaxial tests and a permanent deformation test were used for relating dielectric properties of different base materials to their water content and strength and deformation properties [Kolisoja et al., 2002; Saarenketo, 1998; Saarenketo and Scullion 1995, 1996]. Results proved the importance of the dielectric value to act as an effective indicator of strengths more than the moisture content. In addition, the authors argued that each aggregate type has a unique relationship between material dielectrics and moisture content. At present, laboratory testing on controlled strength-induced characteristics of different unbound materials could be carried out for a better understanding of this occurrence, together with ground-truth validation by using typical NDT acoustic instrumentation (e.g., FWD techniques).

1.3.1.3 Bound pavement layer and wearing courses

Bound materials are located in the top part of the pavement structure of roads and airfields, and include *i)* bound base course, and *ii)* pavement and wearing course, or just one of them. Traditionally, bitumen and cement are the most common binding agents used for construction of bound layers in case of asphalt and concrete pavements, respectively. Nonetheless, other agents have been used in a fewer cases.

In case of bituminous pavement thickness evaluation, GPR predictions can reach an accuracy of 3-5 % on the average, without using cores for validation [Saarenketo, 2009]. Overestimation of asphalt thicknesses may be encountered when assessing older pavements through surface reflection techniques, as the surface dielectric value of the pavement is estimated from the asphalt surface [Al-Qadi et al., 2002]. Another important issue is concerned to thin layer thickness estimation, whereby the use of high-frequency pulsed radar allows for detecting layers having few millimeters thick [Dérobert et al., 2002].

Moreover, defects in bituminous pavement have been widely investigated within their various occurrences. Damaging events such as stripping [Cardimona et al., 2003], segregation [Sebesta and Scullion, 2002], cracking [Benedetto, 2013; Saarenketo and Scullion, 1994], and moisture barriers [Saarenketo and Scullion, 2000] have been faced over the past two decades. As of today, few contributions exist on the possibility to investigate mechanical properties of bound layers through radar data [Loizos and Plati, 2011; Plati and Loizos, 2012, 2013] in order to provide more time-efficient GPR surveys both for rehabilitation design, quality

control, and for possible widening of pavement management system (PMS) data bases.

1.3.1.4 Concrete pavement

Amongst the main issues to face in concrete pavement, voids beneath the joints, cracking, and delamination are traditionally the major defects to repair. The location of voids under concrete pavement was one of the first uses of GPR in this field of application [Kovacs and Morey, 1983]. In addition, it has been demonstrated that the minimum dimension of voids detectable, is a function of the antenna system configuration (i.e., ground- or air- coupled GPR systems) [Saarenketo and Scullion, 1994, 2000]. Saarenketo and Scullion [2000] investigated the possibility to understand the water saturation of voids under concrete pavement, even in case of void volume occupied uniquely by air. As mentioned, other widespread applications have concerned the location and detection of dowels and anchors around the concrete slab joints [Alani et al., 2014; Maierhofer and Kind, 2002], the detection of delamination [Alani et al., 2013; Hugenschmidt and Loser, 2008; Huston et al., 2000], and the measurement of asphalt overlay thickness [Maser, 2002b]. One main issue of GPR-based measurements in concrete pavements is related to the exact location of layer interfaces. In particular, due both to the similar electrical properties of concrete and base course, and to higher signal attenuation in concrete, it can be difficult to distinguish their interface [Cardimona et al., 2003].

1.3.2 Ground-penetrating radar systems

1.3.2.1 Pulsed GPR systems

Impulse GPR is the most common GPR system used especially for the relative easiness of data interpretation and the possibility to extend its use over a large variety of applications and in many different disciplines [Daniels, 2004; Jol, 2009; Slob et al., 2010]. Such system can be considered as an amplitude-modulated radar that provides the transmission of the signal as a very short pulse (~10^{-9} s) with a wide spectrum, whereby the absolute bandwidth is generally greater than 1 GHz. In this regard, pulsed GPR systems are also called ultra-wide bandwidth (UWB) radars. According to the Federal Communications Commission (FCC) [2002], a device is considered UWB if it has a fractional bandwidth greater than 0.25 or if its bandwidth occupies 1.5 GHz or more of spectrum when its center frequency is greater than 6 GHz.

The physical principle of an impulse GPR system is based on sending a short EM pulse through the antenna to the ground and then recording the pulses reflected from the surface and the internal non-homogeneities. The two-way travel time to the targets can therefore be measured in the time domain between the reflected pulses.
The electronic configuration provides a trigger pulse that is first generated in the radar control unit, to be then sent to a transceiver. The pulse is here modulated and amplified to become a bipolar transmit pulse with a much higher amplitude and bandwidth. The pulse is therefore sent to the ground through the transmitting antenna, such that the reflected signal can be collected by the receiving antenna and transmitted to the receiver circuitry. Such pulses are produced in a large number by the pulse generator at a fixed pulse repetition frequency (PRF).
The entire reflected signal is digitized through a digital-to-analog converter (ADC) and then transferred to a digital signal processor (DSP), where it is amplified and filtered according to the user-selected parameters. The collected data is finally displayed for immediate interpretation and is stored on magnetic media for later processing.
One main benefit from the use of such GPR system is related to its pulsed nature, which can transmit high peak power EM pulses in order to ensure an appropriate depth of penetration, with an overall low average power.

1.3.2.2 SFCW radar systems

Synthetic pulse GPR, also called stepped frequency continuous-wave (SFCW) radar, operates in the frequency domain. The system provides linear increments of a frequency sweep over a chosen bandwidth performed between two specific start and stop frequencies. The amplitude and phase of energy scattered from subsurface objects are indicated by the reflected energy, which is received as a function of frequency. The received-to-emitted signal is sampled during the sweep and recorded as a function of frequency, i.e., at each discrete frequency [Koppenjan, 2009]. The amplitude and phase of the reflected signals are therefore precisely measured and recorded for each frequency step, through the Fourier Transform (FT) of the reflected signal. The time domain signal from which the detection and range information are extracted, is then reconstructed through the application of a simple inverse fast Fourier Transform (IFFT) to the recorded samples. Alternative methods for detection and range estimation can also be applied directly in the frequency domain.

Amongst the several advantages arising from the use of stepped-frequency radar, we can broadly cite *i)* the controlled transmission frequencies, *ii)* efficient use of power, and *iii)* efficient sampling of ultra-wideband signals. The collection of complex reflection functions that allow complex processing algorithms and the control of the amplitude information, are enabled by these systems. With regard to the main drawbacks on the use of SFCW radars, relatively high costs of electronics together with its complexity and the lack of commercial software for signal processing can be mentioned.

Most of the SFCW radar applications include detection of landmines [Langman and Inggs, 1998; Nicolaescu and Van Genderen, 2008; Soldovieri et al., 2011], through-wall imaging and motion detection [Biying et al., 2011], and the accurate characterization of subsurface dielectric properties [Lambot et al., 2004b].

In the field of pavement engineering, a lower number of applications than those with pulsed GPR systems is encountered. Starting from the early 2000s, SFCW radars have been mostly used to detect concrete pavements, [Dérobert et al., 2001; Dérobert et al., 2002; Eide 2002; Huston et al., 2000], concrete degradation processes [Dérobert et al., 2009], and thickness of very thin pavements [Dérobert et al., 2002]. In addition, laboratory applications of SFCW radar systems have been focused on the characterization of layered media [Lambot et al., 2007; Minet et al., 2010], although the complexity related to a real multi-layered pavement structure, as well as to the response of the most common encountered road materials to an applied EM field [Patriarca, 2013], needs to be deepen. Special care should be first given to detect the EM properties of load-bearing layer materials as a function of water and clay contents, in order to prevent structural damages due to the loss of bearing ratio.

1.3.3 Ground-penetrating radar antennas

Radar systems need transmitting and receiving antennas, which transform electrical signals to and from vector EM fields. According to the number of antennas used, a GPR system can be mono-static (i.e., transmitting and receiving antennas are coincident), bi-static (i.e., one antenna is used for transmission and another antenna is used for reception), or multi-static (several combinations of sources and receivers are possible). Depending on the deployment of antennas, GPR systems are classified as air-coupled (or launched), or ground-coupled systems. A brief description within the use

of the above two configurations in road engineering applications is included in this Subsection.

1.3.3.1 Air-coupled systems

Antennas in air-coupled systems for civil engineering applications are typically 150 mm to 500 mm above the surface. Most air-coupled antenna types are transverse electromagnetic (TEM), although hemispherical butterfly dipole (HBD) types have also been used in road surveys.
These systems produce a relatively clean radar signal and allow for highway speed surveys [Loizos and Plati, 2007a]. According to Saarenketo and Scullion [2000], both layer thickness and layer dielectrics can be computed through signal processing in case of defect-free pavements. Traditionally, air-coupled antenna systems are pulsed radar systems generally operating in the range 0.5 GHz–2.5 GHz, with the most common center frequency being 1.0 GHz. Antenna height from the ground ranges usually between 0.3 m and 0.5 m. Penetration depth varies typically from 0.5 m up to 0.9 m [Lahouar et al., 2002]. The low potential of this latter can be considered as the main drawback of these systems, since part of the EM energy, sent by the antenna, is reflected back by the pavement surface. On the contrary, advantages broadly include *i)* independence between antenna coupling and changes in pavement properties, *ii)* measurements repeatability, useful for quality control surveys, *iii)* full speed analysis avoiding any constraints to traffic.

1.3.3.1 Ground-coupled systems

Antennas in ground-coupled systems are in full contact with the ground, thereby allowing for a higher signal depth of penetration at the same frequency. In particular, during data acquisition these antennas maintain contact with pavement or they are suspended just above it. Ground-coupled antennas for civil engineering applications are usually in the form of bowtie dipoles, and operate in a wide range of center frequencies from 80 MHz to 1500 MHz, that must be chosen according to the objective of the survey. In addition, high vertical resolution allows for detecting thin targets, such as pavement cracks [Benedetto, 2013], cables and reinforcement bars in concrete structures [Alani et al., 2014; Stryk et al., 2013]. Notwithstanding the higher signal penetrations and resolutions than those of the air-launched radar systems, some problems arising from surface coupling and antenna ringing may cause difficulties in obtaining representative information without the use of proper signal processing. Another drawback with respect

to air-coupled antenna systems is represented by a lower data collection speed, normally ranging from 5 km/h to 30 km/h, which greatly affects the productivity of such radar systems. Aiming to both optimize such intrinsic gap between these two systems as well as the efficiency and effectiveness of radar road surveys, the combined use of air-coupled and ground-coupled systems should be improved for carrying out, respectively, PMS surveys at the network level, and detailed analyses of the most damaged areas, when emerging from GPR air-launched investigations.

1.4 Statement of the problem

Investigation on road pavements and materials through ground-penetrating radar has started since the late 1980s, when increasing demand for road rehabilitation projects motivated the use of high-performing NDTs. GPR-based applications in road engineering were originally focused on geometrical observation of subsurface pavement structure, namely on layer thickness measurements [Scullion et al., 1992; Maser, 1994]. Many efforts have been then devoted to measuring the effects of pavement damages, such as stripping [Cardimona et al., 2003], segregation [Sebesta and Scullion, 2002] and cracking [Benedetto, 2013; Saarenketo and Scullion, 1994] in bituminous pavements, or delamination [Alani et al., 2013; Hugenschmidt and Loser, 2008; Huston et al., 2000] and voids beneath joints [Kovacs and Morey, 1983; Saarenketo and Scullion, 2000] in concrete pavement structures. Though a large amount of GPR-based applications is available on subsurface observation of pavement structure and on the effects of unsuitable pavement project designs or high traffic load actions, fewer contributions currently exist on the possibility to detect changes in relevant physical (e.g., water and clay contents) and strength characteristics (e.g., layer moduli) of road materials and subgrade soils.

Various experimental and theoretical approaches have been developed through the evaluation of electromagnetic parameters by signal processing in the time domain, thereby requiring the use of core drillings at spatial intervals along the road route [Saarenketo et al., 2000]. On the contrary, a lower amount of research works exists on the use of more self-consistent GPR methods, e.g., methods based on frequency domain analyses of the GPR signal, which can help to interpret the response of road materials regardless of the use of destructive sampling [Benedetto et al., 2010; Lambot et al., 2004]. In this regard, the use of SFCW radars in pavement engineering applications [Dérobert et al., 2002] is not yet adequately matched to that of pulsed radar systems, so that additional information on

road materials behaviors under changing physical conditions could be provided.
Overall, there is thus still some uncertainty as to the exact nature of the relationships between electromagnetic responses and parameters indicative of pavement condition, as well as the influence of the interactions between these parameters on the electromagnetic response of road materials.
Materials EM behavior can be macroscopically described by many models in literature. In this thesis, laboratory experiments are firstly carried out considering multi-phase soil mixtures composed by several constituents (solid, liquid and gas) in order to investigate the response of typical road materials to an applied EM field. On-site validations are therefore carried out through ground-truth measurements, to test the ability of material characterization and of relevant physical parameters detection having no or little a-priori information.

1.5 Thesis objectives

To overcome the aforementioned problems, this research proposes a contribution to advance the non-destructive investigation on road pavements and materials by using ground-penetrating radar techniques. This investigation will allow the following contributions:

- Development of a self-consistent approach for evaluating subsurface moisture spatial field at the large scale of surveying by avoiding the use of destructive samplings;
- Development of models by using different signal processing techniques for predicting clay content in load-bearing layers;
- Development of prediction models for inferring strength characteristics of both bound, unbound pavement structures and subgrade soils from their electric properties;
- Evidence of the effectiveness of frequency-based analyses of the GPR signal to interpret the response of road materials;
- Evidence of the potential of SFCW radars on the reconstruction of EM properties of typical road materials.

Several practical implications may result from this work. Firstly, by improving the reliability of in-situ investigation on road pavements and materials conditions, the implementation of these techniques may be focused on quality control surveys as part of a performance-based approach in construction. Secondly, the use, even combined, of several GPR signal

processing techniques may improve the non-destructive monitoring of damages in pavement as part of a structural health monitoring strategy to serve as an early warning of critical areas prior to major irreversible damages. Thirdly, a great contribution on the possibility to more easily update predictive service life models can be provided whether the amount of relevant physical parameters (e.g., water and clay contents) and the loss of layer moduli may be quantified more accurately.

1.6 Thesis outline

This document is divided into six chapters and one appendix, in the manner described as follows:

- Chapter 1 provides an introduction about the research and its objective, following the main open issues arising from the analysis of the state of the art on the use of GPR in road engineering applications from the beginning to the present day.
- Chapter 2 presents the fundamentals of electromagnetic theory that form the basis of the techniques used to investigate conditions of road pavements and materials as part of this thesis.
- Chapter 3 describes the in-situ application of the Rayleigh scattering method in order to evaluate subsurface moisture spatial field. In addition, the potential of GPR to detect moisture content at the small scale (area ≤ 0.01 m^2) by using a common permittivity estimation technique, was investigated by comparing GPR-based moisture with moisture content measured by eight capacitance probes, fairly evenly placed over the entire surveyed area. Tests were conducted over a 16m×16m study site consisting of an unpaved natural soil. Results showed the good potential of the Rayleigh scattering method to provide mapping of subsurface moisture spatial distribution, when compared to traditional GPR-based approaches for volumetric water content estimation. Furthermore, good results were obtained by comparing moisture measurements at the small scale.
- Chapter 4 describes the ability of GPR to evaluate clay content in unbound pavement layers and subgrade soils using different processing techniques, namely the Rayleigh scattering method, the full-waveform inverse modeling, and the signal picking technique. Laboratory experiments were carried out on three types of soil samples classified by AASHTO [2011] as A1, A2, and A3, with

growing amounts of bentonite clay from 2% up to 25% by weight. Two prediction models were developed based on, respectively, *i)* the use of the Rayleigh scattering method by spectral analysis of the investigated road materials under different clay abundances, and *ii)* the use of volumetric mixing models to assess the capability of indirectly retrieving the clay content, from permittivity estimation by full-waveform inverse modeling. The good potential arising from the use of a SFCW radar system is also demonstrated.

- Chapter 5 presents the possibility to infer strength characteristics of both bound, unbound pavement structures and subgrade soils from their electric properties. A prediction model of subgrade moduli was proposed as a result of laboratory calibration tests, by measuring the electromagnetic response of soil samples under known conditions of growing compaction, and validation tests on unpaved soil, whose mechanical properties were measured through LFWD. As far as concerns bound bituminous layers, the prediction model was developed by comparing the elastic moduli inferred from LFWD measurements and the amplitudes of reflected GPR signals, over a 30m×4m flexible pavement test site. Both the models showed promising results when compared to the ground-truth strength data.
- Chapter 6 is a summary of the main findings and it concludes the present research by providing recommendations for future challenges and developments.

Appendix A contains a detailed description of different ground-penetrating radar tools used to non-destructively investigate road pavements and materials whitin the framework of the activities described in this thesis.

2. Electromagnetic fundamentals

2.1 GPR principles

2.1.1 Generation of EM waves

To appreciate the capabilities and limitations of the GPR sensing technology and to be able to fully exploit this tool, it is necessary to understand the characteristics and behavior of radio waves. Understanding the theory of EM waves, grasping the principles of their generation and reception, will provide the GPR user a better understanding of the art and science of radar interpretation.

Without loss of generality, discussion on electromagnetic fundamentals in this Section are limited to the propagation of uniform plane waves. Nevertheless, more complicated wave fronts can be described as a combination of plane waves. The success of GPR is based on EM waves operating in the frequency range where displacement currents dominate and losses associated with conduction currents are minimal [Reppert et al., 2000]. Short EM impulses from GPR propagate in the medium having pulse duration of $\leq$ 1 ns. The GPR technology relies on Maxwell's equations [Maxwell, 1865], which describe the propagation of EM waves in a medium. In particular, Maxwell's equations describing the wave propagation in a conductive dielectric are as follows:

$$\nabla \times \vec{E} = -\frac{\partial(\vec{B})}{\partial t} \tag{2.1.1}$$

$$\nabla \times \vec{H} = \vec{J} + \frac{\partial(\vec{D})}{\partial t} \tag{2.1.2}$$

In harmonic regime, Equations (2.1.1) and (2.1.2) can be written as:

$$\nabla \times \vec{E} = -j \cdot \omega \cdot \mu \cdot \vec{H} \tag{2.1.3}$$

$$\nabla \times \vec{H} = (\sigma + j \cdot \omega \cdot \varepsilon) \cdot \vec{E} \tag{2.1.4}$$

where $\vec{E}$ is the electric field (or electric field intensity) vector, $\vec{D}$ is the electric induction (or electric field density) vector, $\vec{H}$ is the magnetic field (or magnetic field intensity) vector, $\vec{B}$ is the magnetic induction (or magnetic field density) vector, $\vec{J}$ is the total current density (including both free and bound current) vector. $\sigma = \sigma' - j\,\sigma''$ is the complex conductivity of the medium. It describes how well the medium conducts electric current. At higher frequencies the response time can become significant, thereby resulting in an out-of-phase component. The imaginary part of the conductivity is related to this out-of-phase polarization component and is usually small at most radar frequencies. $\varepsilon = \varepsilon' - j\,\varepsilon''$ is the complex permittivity of the medium. The real part of the permittivity ε' is a measure of the ability of the medium to be polarized under an electric field. For the high frequency range, the dipoles can not follow the fast change in magnitude of the electric field, and the polarization will be out-of-phase, causing a relaxation phenomenon. The imaginary part of the permittivity relates to this out-of-phase polarization component and can not be neglected at most radar frequencies. μ is the permeability of the medium. If the material is non-ferrous, the approximation $\mu \approx \mu_0$ is valid. ε_0 is the permittivity of free space, also called the dielectric constant. μ_0 is the permeability of free space, also called the magnetic constant.
In Equation (2.1.4), it can be noticed that for conductive dielectrics, the macroscopic parameters σ and ε always occur in the combination $\sigma + j\,\omega\,\varepsilon$. Splitting up the two parameters in their real and imaginary part, this combination can be rewritten as follows:

$$\sigma + j\cdot\omega\cdot\varepsilon = \left(\sigma' + \omega\cdot\varepsilon''\right) + j\cdot\omega\cdot\left(\varepsilon' - \frac{\sigma''}{\omega}\right) = \sigma_e + j\cdot\omega\cdot\varepsilon_e \qquad (2.1.5)$$

where $\sigma_e = \sigma' + \omega\,\varepsilon''$ is defined as the real effective conductivity, and $\varepsilon_e = \varepsilon' - \sigma''\,\omega_e$ is defined as the real effective permittivity.
The real effective conductivity determines a current in-phase with the electric field, while the real effective permittivity is related to a current out-of-phase with the electric field. It is also useful to define ε^*, i.e., the complex apparent permittivity, as:

$$j\cdot\omega\cdot\varepsilon^* = \sigma_e + j\cdot\omega\cdot\varepsilon_e \qquad (2.1.6)$$

and the loss tangent, tan δ, as:

$$\tan\delta = \frac{\sigma_e}{\omega \cdot \varepsilon_e} \tag{2.1.7}$$

Therefore, by using Equation (2.1.7) in Equation (2.1.6), the complex apparent permittivity can be expressed as a function of the loss tangent:

$$\varepsilon^* = \varepsilon_e \cdot (1 - j \cdot \tan\delta) \tag{2.1.8}$$

Thus, by exploiting the definition of the complex apparent permittivity, Equation (2.1.4) can be written as:

$$\nabla \times \vec{H} = j \cdot \omega \cdot \varepsilon^* \cdot \vec{E} \tag{2.1.9}$$

From algebraic simplifications and substitutions, the wave equation describing the electric field wave propagation in a lossy dielectric medium is found as follows:

$$\nabla^2 \vec{E} + \varepsilon^* \cdot \mu \cdot \omega^2 \cdot \vec{E} = 0 \tag{2.1.10}$$

Finally, the solution of Equation (2.1.10), representing a harmonic plane wave propagating in the direction κ can be written as:

$$\vec{E} = \vec{E}_0 \cdot e^{-j \cdot \vec{k} \cdot \vec{r}} \tag{2.1.11}$$

with the wave number $\kappa = |\vec{\kappa}|$ given by:

$$\kappa = \omega \cdot \sqrt{\varepsilon^* \cdot \mu} \tag{2.1.12}$$

The wave number κ is complex and can be separated into real and imaginary parts:

$$j\kappa = \alpha + j \cdot \beta \tag{2.1.13}$$

Accordingly, the plane wave solution (Equation (2.1.11)) can be written as:

Accordingly, the plane wave solution (Equation (2.1.11)) can be written as:

$$\vec{E} = \vec{E}_0 \cdot e^{-\vec{\alpha}\cdot\vec{r}} \cdot e^{-j\cdot\vec{\beta}\cdot\vec{r}} \tag{2.1.14}$$

The first exponential term represents the attenuation of the plane wave in a lossy medium. The rate is specified by α, the attenuation constant. The second exponential term represents the propagation, while the phase is controlled by the phase constant β. The constants are given by:

$$\alpha = \omega \cdot \sqrt{\mu \cdot \varepsilon_e} \cdot \sqrt{0.5 \cdot \left(\sqrt{1 + \tan^2 \delta} - 1\right)} \tag{2.1.15}$$

$$\beta = \omega \cdot \sqrt{\mu \cdot \varepsilon_e} \cdot \sqrt{0.5 \cdot \left(\sqrt{1 + \tan^2 \delta} + 1\right)} \tag{2.1.16}$$

It can be seen from Equation (2.1.15) that the attenuation of the EM wave in a conductive medium is due to both the conductive and dielectric effects. Reference tables, reporting the attenuation and relative permittivity of various materials and soils at different radar frequencies can be found in literature [Daniels, 2004; Von Hippel, 1995]. The attenuation in the soil can increase drastically with frequency. Hence, the choice of the frequency band of a GPR system will strongly influence the maximum penetration depth of the system.

2.1.2 Propagation of EM waves in dielectrics

Electric properties of materials are determined by electrical conductivity, permittivity and permeability. The permittivity is the most important parameter for GPR, because at a high frequency any material behaves as dielectric. The electromagnetic wave behavior in subsurface material is strongly dependent on its electrical conductivity, and the electrical conductivity is usually controlled by water. When a material is conductive, the electromagnetic field is diffusive and can not propagate as an electromagnetic wave. When it is resistive, or dielectric, an electromagnetic field can propagate as an electromagnetic wave. Electromagnetic induction (EMI) sensors, which are usually referred to metal detectors, use this frequency range because penetration into the soil is easier. Nonetheless, GPR uses electromagnetic waves and its interpretation is easier because the diffusion effect is not so considerable. When using higher frequencies, any material behaves as dielectric because the displacement current dominates

the conducting current, and the electromagnetic field propagates as a wave, although the attenuation gets higher. GPR measures the reflected electromagnetic wave from the subsurface structure. The velocity and reflectivity of the electromagnetic wave in soil is characterized by the dielectric constant (permittivity) of the soil. When the dielectric constant of the soil is ε_r, the velocity in this material is given by:

$$v = \frac{c}{\sqrt{\varepsilon_r}} \tag{2.1.17}$$

where c is the speed of light in free space (3×10^8 m/s) and ε_r is the material's relative permittivity. When the electromagnetic wave velocity is known, by measuring the travel time Δt we can estimate the depth h of the reflecting object as follows:

$$h = (v \cdot \Delta t)/2 \tag{2.1.18}$$

The travel time is defined as the amount of time from the being transmitted to signal and the time signal is received, which corresponds to the propagation time from the reflecting object. The reflection occurs, when the electromagnetic wave encounters any electrically inhomogeneous material.

The most significant electrically inhomogeneous material is metal. Any buried metallic material such as pipes and cables are quite easily detected by GPR. Nevertheless, it is worth noting that even an insulating material can be an electrically inhomogeneous material. Insulating material is referred to as dielectric material, and its characteristics are defined by the dielectric constant. Commonly, the dielectric constant is also defined as permittivity.

When an electromagnetic wave is incident to a flat boundary of two different materials having dielectric constant equal to ε_1 and ε_2, respectively, the electromagnetic wave (whose amplitude can be considered normalized to 1) is reflected by the boundary and its amplitude is Γ. In particular, Γ is defined as the reflection coefficient of a boundary and is given by:

$$\Gamma = \frac{\sqrt{\varepsilon_1} - \sqrt{\varepsilon_2}}{\sqrt{\varepsilon_1} + \sqrt{\varepsilon_2}} \tag{2.1.19}$$

Equation (2.1.19) shows that the amplitude of the reflected wave is defined by the ratio of the dielectric constants of the two materials. The reflection coefficient Γ takes a value in the interval [-1; 1]. If the lower material is metal, the reflection coefficient is equal to -1 and it takes the maximum amplitude. Therefore, the reflection from metallic material is always very obvious. This condition stands even when the metallic material is a thin sheet, because all the electromagnetic energy is reflected by the metal.

In a GPR measurement the radar target has a finite size, thereby it is not actually infinitely large. Generally, a larger target reflects stronger signals, when the size of the target is smaller than that of the wavelength. The reflectivity of an isolated target is measured by its radar cross section (RCS). When the scattering object is small, the RCS is proportional to the size of the objects. The dielectric constant of subsurface material is based on rocks, and soils, which vary in their constituent material themselves. Nevertheless, the dielectric constant of these materials is similar, and the water contained in the material is the most significant factor affecting the value of the dielectric constant. From Equation (2.1.19), it is possible to understand any change of water conditions in the soil and geological formations which can cause the electromagnetic reflection. Overall, the dielectric constant of the rock and soil material in dry conditions has a value between 3 and 5, while the dielectric constant of the water is equal to 81.

In that regard, it is easy to understand how the dielectric constant of the soil changes with soil moisture. Therefore, although the material of the soil is homogeneous, when moisture is not homogeneously distributed, the electromagnetic wave can be reflected by the soil. This condition frequently causes strong "clutter", namely as reflections from targets. Therefore, inhomogeneous moisture in the soil, small stones, and gravel included in the soil are common causes of the clutter. Another source of clutter in GPR is the reflection from the ground surface. Most of the GPR systems are scanned very close to the ground surface, such that strong reflection can be received from the ground surface as a result of a large dielectric constant between air and soil.

Finally, it is worth mentioning that the clutter is not random noise. In fact, when having time-varying random noise, it can be measured over time and then the random signal can be removed by time averaging. Nonetheless, clutter in the radar is a deterministic signal, and stable in time. Therefore, it can not be removed by the time-averaging method. When the reflection from the target is weak and the noise level is high, we can achieve a better signal-to-noise-ratio (SNR) by increasing the transmission power. It is

possible, when the transmission signal is propagated through a highly homogeneous medium, such as air. In the case of GPR, a completely different situation occurs. Although a higher power signal is transmitted, the signal strength ratio of the reflection from soil and clutter does not change. The SNR can be improved by increasing transmission power, only for the system noise. However, the system noise is a time-varying random noise, and the noise level can be decreased by averaging the received signal over a long time. Since buried object are static targets, the GPR system can stay at one location and acquire the received data for a longer time to increase the SNR value. This situation is valid for most GPR surveys, and therefore the transmission power of GPR can be very weak.

2.1.3 Main theories of scattering

Geometrical optics, or ray optics, describes how the light propagates in terms of "rays". Light rays are defined to propagate in a rectilinear fashion as far as they travel in a homogeneous medium. Rays curve (and may split in two different rays) at the interface between two media, may curve in a medium where the refractive index changes, and may be absorbed and reflected.

When light is incident on an interface between two transparent optical media—such as between air and glass or between water and glass—four options can occur to the incident light: *i*) it can be partly or totally reflected at the interface; *ii*) it can be scattered in random directions at the interface; *iii*) it can be partly transmitted via refraction at the interface and enter the second medium; *iv*) it can be partly absorbed in either medium. When light reflects from a plane surface, the angle that the reflected ray makes with the normal (i.e., with the line perpendicular to the surface) at the point of incidence is always equal to the angle the incident ray makes with the same normal. The incident ray, reflected ray, and normal always lie in the same plane. Commonly, this is known in literature as the "Law of Reflection". Mirrors with curved surfaces can be modeled by ray-tracing, using the law of reflection at each point on the surface. For mirrors with parabolic surfaces, parallel rays incident on the mirror produce reflected rays that converge at a common focus. Other curved surfaces may also focus light, although some aberrations may occur due to the diverging shape. In particular, spherical mirrors exhibit spherical aberration.

When light is incident at an interface, it will be partly reflected and partly transmitted. The bending of light rays at an interface between two optical media is called "refraction". Overall, refraction occurs when light travels

through an area of space that has a changing index of refraction. The two transparent optical media that form an interface are distinguished from one another by a constant called the "index of refraction", generally labeled with the symbol *n*. The index of refraction for any transparent optical medium is defined as the ratio of the speed of light in a vacuum to the speed of light in the medium: $n = c / v$, where c is the speed of light in free space (vacuum) and v is the speed of light in the medium.

Overall, the greater the index of refraction of a medium, the lower the speed of light in that medium and the more light is bent in going from air into the medium. Snell's law of refraction relates the sines of the angles of incidence and refraction at an interface between two optical media to the indexes of refraction of the two media: $n_i \sin \theta_i = n_r \sin \theta_r$ where n_i and n_r are the index of refraction in the incident and in the refracting medium, respectively, while θ_i and θ_r are the angles of incidence and of refraction, respectively.

Various consequences of Snell's Law include the fact that for light rays traveling from a material with a high index of refraction to a material with a low index of refraction, it is possible for the interaction with the interface to result in zero transmission. This phenomenon is called total internal reflection and allows for fiber optics technology. As light signals travel down a fiber optic cable, it undergoes total internal reflection allowing for essentially no light lost over the length of the cable.

Snell's Law can be used to predict the deflection of light rays as they pass through "linear media" as long as the indexes of refraction and the geometry of the media are known.

As regards the scattering problem, it can be described as a physical process that causes radiation to deviate from a straight trajectory. We can see this phenomenon also in terms of reflection: when a plane surface is made of microscopic irregularities, we would get diffuse instead of specular reflection. The same concept is observed for radiation passing through a transparent medium: when having non-uniformities (e.g., particles, bubbles, droplets, density fluctuations) some of the radiation will deviate from its original trajectory. In a physical description of the phenomenon, we distinguish between two types of scattering, namely elastic and inelastic. Elastic scattering involves no (or a very small) loss or gain of energy by the radiation, whereas inelastic scattering does involve some change in the energy of the radiation. If the radiation is substantially or completely extinguished by the interaction (losing a significant proportion of its energy), the process is known as absorption. When radiation is only

scattered by one localized scattering center, this is called "single scattering". Single scattering can usually be treated as a random phenomenon, often described by some probability distribution. Usually, many scattering centers are present, so that the radiation may scatter several times, which is known as "multiple scattering". Light scattering and absorption are the two major physical processes contributing to the visible appearance of physical objects. The spectral distribution of absorption determines the color of a surface, while the amount of scattering determines whether the surface is mirror-like or not.

The scattering process may be thought of as the redirection of the signal that takes place when an electromagnetic wave (i.e., the incident signal) encounters an obstacle or non-homogeneity, i.e., the scattering particle. As the EM wave interacts with the discrete particle, the electron orbits within the particle's constituent molecules are perturbed periodically with the same frequency as the electric field of the incident wave. The oscillation or perturbation of the electron cloud results in a periodic separation of charge within the molecule, which is called an induced dipole moment. The oscillating induced dipole moment is revealed to be as a source of EM radiation, thereby resulting in scattered signal. Hence, scattering is not simply a matter of incident EM waves "bouncing" off the surface of an encountered object.

Formal scattering theory may be categorized in terms of two theoretical frameworks.

One is the theory of Rayleigh scattering (after Lord Rayleigh) that is, strictly speaking as originally formulated, applicable to small, dielectric (non-absorbing), spherical particles [Bohren and Huffman, 1983; Narayana and Ophir, 1983].

The second is the theory of Mie scattering (after Gustav Mie, [Mie, 1908]) that encompasses the general spherical scattering solution (absorbing or non-absorbing) without a particular bound on particle size. Accordingly, Mie scattering theory has no size limitations and converges to the limit of geometric optics for large particles. Mie theory, therefore, may be used for describing most spherical particle scattering systems, including Rayleigh scattering. Nevertheless, Rayleigh scattering theory is generally preferred if applicable, due to the complexity of the Mie scattering formulation.

In order for Rayleigh scattering to be valid, the size of the particle must be much smaller than the wavelength of the incident radiation, both inside and outside of the particle [Van de Hulst, 1981]. These conditions can be expressed as:

$$d << \lambda, \qquad d << \lambda/|n| \tag{2.1.20}$$

where d is the diameter of the particle, λ the wavelength of the incident radiation, n is the refractive index and λ/|n| is the wavelength inside the particle. The above Rayleigh criteria (Equation (2.1.20)), physically correspond to the assumptions that the particle is sufficiently small such that it encounters a uniform electric field at any moment, accordingly the time for penetration of the electric field is much less than the period of oscillation of the EM wave.

It is well-known that the intensity I of the EM wave scattered by a single small particle from a beam of unpolarized wave of wavelength λ and intensity I_0 can be written as follows:

$$I(\theta) = I_0 \frac{1+\cos^2\theta}{2R^2}\left(\frac{2\pi}{\lambda}\right)^4\left(\frac{n^2-1}{n^2+2}\right)^2\left(\frac{d}{2}\right)^6 \tag{2.1.21}$$

where R is the distance of the observer to the particle, θ is the scattering angle, n is the refractive index of the particle, and d is the diameter of the particle. The angular distribution of Rayleigh scattering, governed by the $(1+\cos^2\theta)$ term, is symmetric in the plane normal to the incident direction of the light, thereby the forward scatter equals the backwards scatter. Then, the Rayleigh scattering cross-section is given by:

$$\sigma_s = \frac{2\pi^5}{3}\cdot\frac{d^6}{\lambda^4}\cdot\left(\frac{n^2-1}{n^2+2}\right)^2 \tag{2.1.22}$$

Analytically, the Rayleigh scattering cross section is proportional to the sixth power of particle size, and inversely proportional to the fourth power of wavelength. The intensity of the Rayleigh scattered radiation increases rapidly as the ratio of particle size to wavelength increases. Furthermore, the intensity of Rayleigh scattered radiation is identical in the forward and reverse directions.

The Rayleigh scattering model breaks down when the particle size becomes larger than around 10% of the wavelength of the incident radiation. In the case of particles with dimensions greater than this, Mie's scattering model can be used to find the intensity of the scattered radiation. The intensity of Mie scattered radiation is given by the summation of an infinite series of

terms rather than by a simple mathematical expression. Nevertheless, it can be shown that Mie scattering differs from Rayleigh scattering in several respects; it is roughly independent of wavelength and it is larger in the forward direction than in the reverse direction. The greater the particle size, the more of the light is scattered in the forward direction.

3. Volumetric water content evaluation in pavement

3.1 Introduction

Subsurface spatial distribution of moisture is a primary factor in many fields of application ranging from Earth and Planetary Science [Lambot et al., 2010; Pettinelli et al., 2007a], civil and environmental engineering [Benedetto and Pensa, 2007; Knight, 2001; Saarenketo and Scullion, 2000], geology [Greaves et al., 2005], and agriculture [Hubbard et al., 2002, 2005]. It is well-known that small-scale variability in soil hydraulic properties at the centimeter scale affects the spatial variability of moisture content [Ritsema and Dekker, 1998], and large-scale variability is of great concern at the kilometer scale [Jackson and Le Vine, 1996; Weihermüller et al., 2007].
In pavement engineering, applications focused on moisture content evaluation can be broadly classified according to the type of pavement and construction material, whereby different radar systems and processing techniques are specifically used.

3.1.1 Moisture content evaluation in subgrade soils

It is well-known that strength and deformation properties of the road structure and subgrade soils are deeply affected by moisture content.
In this regard, many GPR applications rely on the knowledge of soil moisture content such as stability [Benedetto et al., 2011; Benedetto et al., 2012a; Ékes and Friele, 2004] and compressibility of subgrade soils [Jung et al., 2004], mostly when monitoring in clayey areas.
When rehabilitation and widening of an existing road is needed, compressibility of the subgrade soil can be surveyed directly on site. In this respect, Saarenketo [2009] argued that such approach can be useful within important engineering practices such as settlements' estimation in a new road or in preloading embankments design over clay, silt or peat subgrade [Saarenketo et al., 1992; Saarenketo and Scullion, 2000].

Road sections with excess moisture in the subgrade can be therefore detected in order to optimize drainage design [Al-Qadi et al., 2004; Wimsatt et al., 1998].

As regards monitoring of subsurface moisture content in natural unpaved soils, such as subgrade soils prior to the construction of the overlying layers, techniques with different temporal and spatial scales capabilities are increasingly developing [Robinson et al., 2008a,b; Vereecken et al., 2008]. In particular, moisture in soils is widely evaluated by using high-frequency electromagnetic techniques, due to the large influence brought by the permittivity of water on the relative dielectric permittivity of soils [Topp et al., 1980]. Results and potentialities of remote sensing investigations in large-scale areas ($\geq$ 100 m^2) can be found in Wagner et al. [2007]. However, the huge footprint of such instruments is linked to a low resolution of radar sensors (~10 m) even when considering high-resolution active radar sensors. Shallow-depth measurements and the inability to detect moisture content in a densely vegetated environment are additional drawbacks to be taken into account for remote sensing [Ulaby et al., 1996]. Conversely, point information can be obtained at much finer scales (area $\leq$ 0.01 m^2) using different techniques, such as time domain reflectometry (TDR) [Fellner-Feldegg, 1969], and capacitance probes [Wobshall, 1978], or thermo-gravimetric measurements from core drilling. These methods allow to collect a large amount of data at a tiny temporal resolution in a fine-scale domain (from ~10^{-2} m to 10^{-1} m), although they are time-consuming for effective mapping of large areas. In addition, such techniques are intrusive to the soil structure, and frequently revealing as inaccurate for volumetric water content measurements [Lunt et al., 2005].

In respect of this general framework, the demand for measurement techniques providing numerous, time-efficient, and detailed values of soil water content at the intermediate scale domain (from ~10^{-1} m to 1 m) can be solved by using GPR.

Different surveying techniques exist to estimate θ from GPR. Traditionally, an estimation of ε_r at the GPR measurement scale is carried out and a petrophysical relationship is used to convert ε_r to θ. More recently, research efforts have been devoted to find more self-consistent methods in order to directly evaluate near-surface moisture in soils without the need of petrophysical relationships and calibration of the GPR system.

Overall, five main classes of GPR surveying techniques for permittivity estimation can be identified, as illustrated in Figure 3.1 (a-f): *i)* reflection

methods (Figure 3.1 (a-b)), *ii)* ground-wave measurements (Figure 3.1 (c)), *iii)* borehole transmission measurements (Figure 3.1 (d)), *iv)* surface reflection methods (Figure 3.1 (e)), *v)* inverse modeling of off-ground mono-static GPR systems (Figure 3.1 (f)).

3.1.1.1 Petrophysical relationships

It is well-known by literature that the permittivity of liquid water ranges from 78 to 88 as a function of temperature, while considerably lower values are encountered for the permittivity of air, equal to 1, and the permittivity of solid grains of sand and loamy soils, that typically ranges between 4 and 6 [Cassidy, 2009].

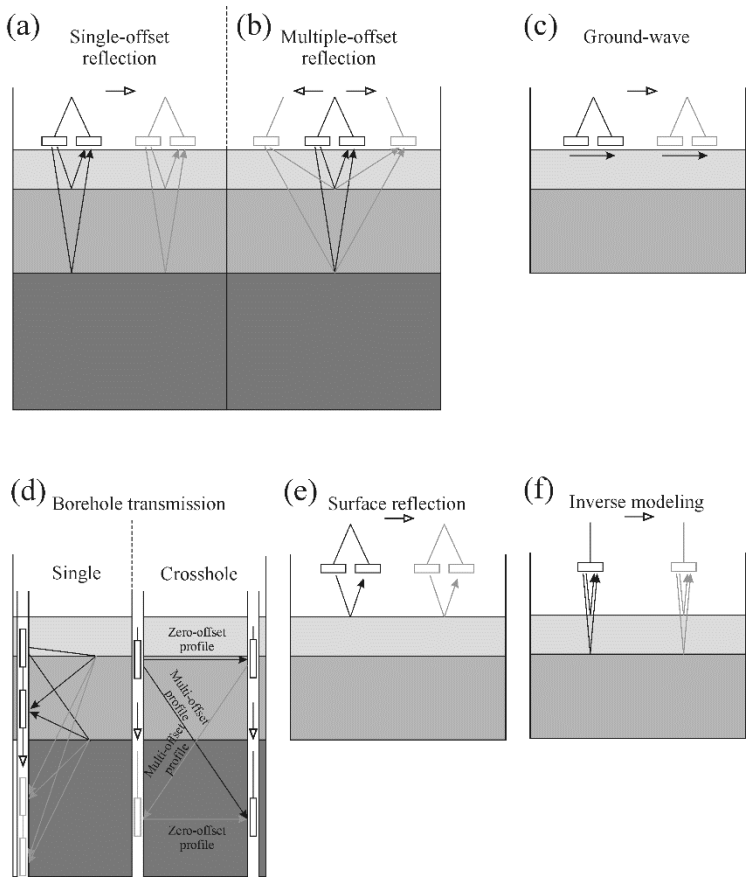

Figure 3.1: Sketch of GPR inspection techniques for moisture evaluation through permittivity measurement: (a) single-offset reflection method; (b) multi-offset reflection method; (c) ground-wave method; (d) single- and cross- borehole transmission measurement; (e) surface reflection method; (f) inverse modelling.

This large dielectric contrast among these three phases, mostly due to the high polarizability of water molecules, has led to the use of different types of approach for predicting volumetric soil water content. Overall, three classes of petrophysical relationships are commonly used, namely *i)* the empirically-based relationships, *ii)* the volumetric mixing formulae, and *iii)* the effective medium approximations.
It is worth noting that the use of an appropriate petrophysical relationship between the permittivity of the bulk material and its volumetric soil water content needs to be selected for a reliable estimate of water content. In that respect, practitioners and end-users can rely on a wide range of studies and research on various types of soil with different textural properties that may effectively lead to the best method to be used. A comprehensive comparison of petrophysical relationships for soil moisture estimation can be found in Steelman and Endres [2011].

Empirical relationships are based on field and laboratory measurements. The main advantage from their use consists of a lower complexity with respect to physical models, thus a higher ease of implementation is achieved according to specific soil textures and water content conditions. In this regard, very limited information about soil textural properties (e.g., porosity, bulk density, pore structure) are required.
Over the last decades, many relationships between θ and ε_r have been developed by numerous researchers using different range of soil textures.
Topp et al. [1980] proposed the most used empirical relationship in the form of a third-order polynomial:

$$\theta = -5.3\times10^{-2} + 2.92\times10^{-2}\varepsilon_r - 5.5\times10^{-4}\varepsilon_r^2 + 4.3\times10^{-6}\varepsilon_r^3 \qquad (3.1.1)$$

Such relationship was obtained by using four different fine-grained soil textures ranging from sandy loam to clay with a range of fresh and saltwater mixtures and saturation levels. The dielectric properties of soil samples placed in a coaxial transmission line were measured through a TDR probe. Results demonstrated that the above petrophysical relationship was suited to moisture conditions ranging from air dry to water saturated, with an error of estimate of 0.013 $m^3\ m^{-3}$. In addition, they found the independence of permittivity measurement from soil density, texture, dissolved salt content, and temperature within the range of soil conditions tested.
The effects of water content layering (e.g., dry over wet, wet over dry) in silt loam soil through different TDR probe designs were investigated by

Nadler et al. [1991]. As in the Topp relationship, a third-order polynomial equation was obtained. The authors demonstrated the accuracy of soil water content estimates from the TDR method regardless of probe type and soil layering, with the exception of very dry soil overlying very wet soil, wherein difficult interpretations of traces were encountered.
More recently, the frequency dependent effects of measurements on water estimation in the GPR frequency range were faced by Curtis [2001] and Patriarca et al. [2013].
More enhanced empirical relationships incorporating the effects of soil texture, density, and organic matter on permittivity measurements were developed by Jacobsen and Schjønning [1993] and Malicki et al. [1992], finding prediction errors of the same order of magnitude as Equation (3.1.1).

A more theoretical approach for relating θ to ε_r is based on volumetric mixing formulae, which use the volume fraction and the dielectric permittivity of each soil constituent to derive a relationship [Dobson et al., 1985; Jones and Friedman, 2000; Roth et al., 1990].
Generally, the form of these relationships in a system accounting for n dielectric components can be expressed as follows:

$$(\varepsilon_r)^{\alpha} = \sum_{i=1}^{n} f_i \left(\varepsilon_{r,i}\right)^{\alpha} \tag{3.1.2}$$

where α is a geometrical fitting parameter describing the structure within the heterogeneous medium [Lichtenecker and Rother, 1931], f_i and $\varepsilon_{r,i}$ represent the volume fraction and the permittivity of the i^{th} constituent, respectively.
As regards near-surface soil, it can be modeled as a typical three-phase system of air, solid, and water constituents as follows:

$$\theta = \frac{\varepsilon_r{}^{\alpha} - (1-\phi)\varepsilon_s{}^{\alpha} - \phi\varepsilon_a{}^{\alpha}}{\varepsilon_w{}^{\alpha} - \varepsilon_a{}^{\alpha}} \tag{3.1.3}$$

where ϕ is the soil porosity, ε_r is the permittivity of the bulk material, ε_a, ε_s, ε_w are the permittivities of air, soil matrix, and water components, respectively. Enhanced versions of volumetric mixing formulae considered a four-phase mixing model incorporating the contribution given by bound

water on the solid mineral grain to the bulk permittivity [Dobson et al., 1985]. It is worth mentioning that the geometric fitting parameter ranges between -1 and 1 for electric fields oriented perpendicular and parallel to a layered medium, respectively. The geometric factor is equal to 0.5 by assuming the travel time through the mixture equivalent to the sum of the volume-weighted travel times through the individual components. In addition, if ε_a is assumed to be equal to 1, Equation 3.1.3 becomes the complex refractive index model (CRIM) [Birchak et al., 1974; Dobson et al., 1985; Gorriti and Slob, 2005; Heimovaara et al., 1994; Roth et al., 1990] given by:

$$\theta = \frac{1}{\sqrt{\varepsilon_w} - 1}\sqrt{\varepsilon_r} - \frac{(1-\phi)\sqrt{\varepsilon_s} - n}{\sqrt{\varepsilon_w} - 1} \tag{3.1.4}$$

The CRIM model has been found to produce adequate results in most cases. Over the past years, different values of the geometric parameter α have been proposed, ranging from 0.46 for a three-phase medium [Roth et al., 1990], or 0.65 for a four-phase medium [Dobson et al., 1985]. More recently, Brovelli and Cassiani [2008] showed α values spanning from 0.25 to 0.8 on the basis of geometry of mineral grains and pore fluids. Furthermore, Patriarca et al. [2013] presented a method for evaluating the optimal α values for two saturated sandy-textured soils at different clay rates from 2% to 25% by weight. Such method revealed to be relatively helpful in three-phase systems (i.e., sand, air, and clay), and in four-phase systems (i.e., sand, clay, air, and water) in the dry end-member cases with 10% clay content. The authors demonstrated that the application of a mixing model may fail for clayey soils in the presence of water, because of the swelling properties of clay. In particular, the use of such model in clay-rich soils may lead to an under-prediction in the correct estimation of electrical properties.

The effective medium approximation (EMA) approach takes into account the textural and structural contribution of each component to the permittivity of a composite material.
Effective medium approximations are based on microscale geometric models incorporating textural and structural information about the heterogeneous system into the prediction of dielectric properties.
Research works based on such methods have proved that the assumption of considering the dielectric properties of the medium as a function of porosity

and water content is not sufficient for a comprehensive modeling, thus unreliable moisture content may be estimated.

Many researchers have used effective medium approximations [Fiori et al., 2005] by incorporating pore structure or geometry [Endres and Bertrand, 2006], grain shape [Jones and Friedman, 2000; Sen, 1984], and fluid distribution at the pore scale [Chen and Or, 2006; Endres and Redman, 1996].

Amongst the various effective medium approximations, the EMA approach proposed by Fiori et al. [2005] provides an approximate water content-permittivity relationship obtained by employing the effective medium approximation in a random mixture of phases. The latter is modeled through the Multi-Indicator model with spherical elements of variable radii. The following equation was proposed:

$$\theta = \frac{(\varepsilon_w + 2\varepsilon_r)[(\varepsilon_a + 2\varepsilon_r)(\varepsilon_r - \varepsilon_s) + 3\varepsilon_r\phi(\varepsilon_s - \varepsilon_a)]}{2\varepsilon_r(2\varepsilon_r + \varepsilon_s)(\varepsilon_w - \varepsilon_a)} \tag{3.1.5}$$

where ϕ is the soil porosity, ε_r is the permittivity of the bulk material, ε_a, ε_s, ε_w are the permittivities of air, soil matrix, and water components, respectively. The relative volume fractions are $n_s = 1-\phi$ (solid volumetric fraction), $n_w = \theta$ (water volumetric content), $n_a = \phi-\theta$ (air volumetric fraction). The permittivities of air and water are kept fixed, and once the bulk porosity is given the proposed formula depends on one parameter, namely the permittivity of the solid phase ε_s.

Furthermore, another approach known as the differential effective medium (DEM) [Norris et al., 1985], has been widely used to examine the dielectric properties of soils and rocks [Endres and Bertrand, 2006; Sen, 1984]. Such method provides infinitesimally small volumes of the inclusions sequentially embedded into the heterogeneous system following an iterative inclusion embedding process. The electrical property of the effective medium resulting from the aforementioned embedding process accounts for the electrical property of the background material for the further embedding step. From a mathematical point of view, Endres and Bertrand [2006] used a homogenization variable p that monotonically increases from 0 to 1 at the beginning and at the end of the embedding process, respectively.

3.1.2 Moisture content evaluation in concrete pavement structure

The detection of moisture is important for the diagnosis of concrete structures at early stages of deterioration as it determines most of the physico-chemical pathologies, such as steel reinforcement corrosion, alkali-aggregate reaction, and freezing-and thawing-cycles [Bertolini et al., 2004; du Plooy, 2013; Hugenschmidt and Loser, 2008].

Under normal conditions, the high pH-value of the pore solution protects reinforcement in concrete from corrosion, such that a stable film is formed on the steel surface which passivates the reinforcing steel and prevents the electrochemical processes taking place during corrosion [Pourbaix, 1974]. Nevertheless, carbonation of concrete or penetrating chlorides can destroy such protective passivity [Neville, 2011; Neville and Brooks, 2010]. In this respect, corrosion of the reinforcement can take place when exceeding a certain threshold value of chlorides and, in combination with water and oxygen, the protective passivity layer on the steel surface is locally destroyed [Montemor et al., 2003]. Two main consequences of chloride inducing corrosion of steel can be encountered, namely *i)* cracking and spalling of the concrete cover as a volume several time larger than the original steel is occupied by the products of corrosion, and *ii)* pitting of the steel reducing its cross-sectional area due to the highly localized chloride-induced corrosion at a small anode. Corrosion of the reinforcement is the main cause of structural concrete deterioration, thus it is one of the main factors affecting the rising of rehabilitation costs.

Overall, techniques based on time domain and frequency domain analysis of radar signal are the two most used approaches in pavement engineering.

3.1.2.1 Time domain analysis

The EM wave propagation is governed by the concrete permittivity, which is influenced by free water [Soutsos et al., 2001] and chlorides [Al-Qadi et al. 1997; Robert, 1998]. On the basis of such approach, changes of the wave reflected by asphalt–concrete or concrete–rebar interfaces have been used to assess corrosion probability. In this regard, Laurens et al. [2000] used a high-resolution ground-coupled 1.5 GHz antenna for detecting the possibility of steel corrosion in a bridge deck. By relating the corrosion probability to the reflectivity rate of a bridge area, the authors compared the amplitude of a reflective signal with the amplitude of the emitted pulse. High attenuation areas were considered as slightly reflective; on the

contrary, low attenuation areas corresponded to highly conductive concrete. GPR and potential histogram analysis led to similar diagnosis concerning the general state of corrosion.
Hugenschmidt and Loser [2008] used an off-ground 2.5 GHz antenna to investigate the effects of moisture and chlorides in concrete on radar amplitudes through laboratory experiments. Nine concrete slabs from three concrete mixtures were built, with three different chloride contents being used for manufacturing the specimens. The base of the mould was covered with an aluminum sheet simulating the reflecting reinforcement. The change of the quotient of reflection amplitudes was evaluated as a possible method for mapping problem zones on concrete bridge decks covered with asphalt pavements.
Nevertheless, the presence of a reflector and a prior knowledge of its position is required for on-site applications of reflection methods. This issue can be considered as one of the main drawbacks of this technique as the exact position is difficult to determine in real conditions.

Direct-wave methods rely on the use of the direct-wave propagating in the first few centimeters of the concrete, such that an independence from the presence of any reflector could be provided. In addition, the distance between the transmitter and the receiver is fixed and known.
For reinforced concrete structures, the presence of steel bars in the near subsurface makes multi-offset radar measurements difficult to process and analyse. In particular, two main problems may be encountered namely the disturbance to the direct-wave propagation from reinforcements and, moreover, an overlapping of direct and reflected signals.
For single off-set measurements, when the receiving dipole is located in the near-field of the source [Roberts and Daniels, 1997], it is possible to use the plane wave approximation for calculating wave velocity and dielectric permittivity. Some authors have shown that the amplitude of the near-field direct-wave is affected by water content [Klysz et al., 2004; Laurens et al., 2002; Sbartaï et al., 2006a; Sbartaï et al., 2006b] and possible presence of chlorides [Sbartaï et al., 2006a]. Laurens et al. [2005] developed an experimental study on the effect of concrete moisture on radar waves propagating through concrete laboratory slabs. Attention was particularly focused on the amplitude, velocity, and frequency spectrum of the waveforms recorded. In particular, the behavior of the transmitter-receiver direct-wave was found to be greatly influenced by moisture in concrete: according to theoretical expectations, the greater was the saturation degree

of concrete slabs, the higher was the permittivity of the medium. Moreover, a linear increase was observed in the amplitudes of the two signals associated with the decrease in the degree of pore saturation.
According to Sbartaï et al. [2006a], a good correlation was demonstrated between direct-wave and reflected-wave attenuation concerning the physical state of the concrete. This correlation was validated on two bridges by comparison of direct-wave attenuation maps with reflection attenuation maps. In addition, Sbartaï et al. [2007] used single off-set radar measurements in order to compare information retrieved from direct-wave measurement to the electrical resistivity method. Results from laboratory tests showed that variations in concrete moisture and chloride contamination level strongly affect the radar direct signal. The tests performed in real road environment confirmed the good correlation between radar direct-wave attenuation and electrical resistivity and, thus, the possibility to detect concrete conditions leading to reinforcement corrosion through radar direct-wave measurements.

3.1.2.2 Frequency domain analysis

Research efforts on moisture content evaluation in concrete structures have been widely focused on time domain signal analysis, while limited studies exist about signal processing in the frequency domain.
Klysz et al. [2004] studied concrete moisture changes according to the velocity analysis of the direct-wave in frequency domain on the basis of Wide Angle Reflection Refraction (WARR) measurements, such that several profiles at the same place were taken using different distances between the two antennas. The authors demonstrated a difference between velocity values measured on dry and wet concretes in the 0.1–1.3 GHz frequency range. In addition, it was shown that the velocity of the radar direct-wave is not affected by a low dispersive medium (e.g., concrete) at the considered frequency range, due to the slight dispersion observed on frequency-velocity curves.
Laurens et al. [2005] analysed the relation between the spectral content of the signal reflected by the bottom of laboratory slabs and the degree of saturation of the concrete by using a high-resolution ground-coupled 1.5 GHz antenna. It was observed that the center frequency lies approximately between 1.18 GHz (saturated concrete) and 1.4 GHz (dry concrete). This behavior can be explained by the presence of water causing electromagnetic dispersion of concrete. Specifically, high frequencies are

generally more attenuated than low frequencies in concrete, and the presence of water contributes to amplify such behavior.

Sbartaï et al. [2009] developed frequency analysis of the direct-wave signal of a 1.5 GHz radar ground-coupled antenna in order to enhance the assessment of concrete water content in civil engineering structures. Several signals were recorded on concrete samples having various rates of saturation, from dry up to saturated conditions. A Fast Fourier Transform (FFT) algorithm was implemented to extract the frequency spectra of each signal, and the direct-wave recorded in air was used as a reference signal for calculating the attenuation-frequency curve. An empirical model was therefore developed by relating the frequency attenuation to the concrete water content. The authors found that the spectrum attenuation of the direct signal increased with respect to frequency in the range analysed (i.e., 0.5–1.8 GHz); in particular, a change of the direct-wave spectrum was induced by moisture variations in concrete, and more attenuation at high frequencies was observed if compared with low frequencies. Attenuation analyses on moisture variations in frequency domain seem to provide more detailed information with respect to attenuation analyses in time domain.

Dérobert et al. [2009] have focused on the electromagnetic characterization of hydraulic concretes within the ground-penetrating radar frequency band. The evaluation of the complex dielectric properties was carried out in laboratory environment on mixtures defined by a specific experimental design. Various parameters of the mixing namely the nature of the aggregates, the nature of the cement, the cement content, the water to cement ratio (w/c), and the chloride content were considered. A multi-linear polynomial model was used such that it was possible to evaluate the influence of every parameter and their interactions on the permittivity. It was demonstrated that the porosity has a relevant effect on the permittivity of the concretes, through their water content. Such effect was increased by chloride presence in the saturated mixing. In dry conditions, their effects remained negligible, with the nature of the aggregates being the most relevant. In this regard, completely different behaviors of chloride could be observed according to its ionic or crystallized state.

More recently, Ihamouten et al. [2012] has studied the validity of the various intermethod coupling by characterizing four concrete mixtures at different water contents. Such approach is based on a coupling between the results of the wave–field transforms (transformations from time–displacement plans to temporal-frequency–spatial-frequency plans) and those of the Q-estimation methods. Promising results were obtained: the

characterization of the hydric status of various concrete mixtures was possible by taking into account both the real and imaginary parts of permittivity over a large GPR bandwidth.

3.2 Methodology and objective

The main goal of the present study is to provide a contribution to the research for preventing structural damages caused by subsurface moisture content in load-bearing soils, as the evaluation of the spatial distribution of soil moisture is a key issue in this research field.
In particular, the ability of GPR to evaluate the spatial variation of shallow soil moisture at the large scale is analysed.
A pulse GPR system with ground-coupled antennae, 600 MHz and 1600 MHz center frequencies, was used over a 16m×16m study site to map the soil moisture with a relatively high spatial resolution. The reliability of GPR data was evaluated by two different methods for the estimate of soil water content.
First, soil moisture values were derived from the evaluation of the relative dielectric permittivity of soils assessed by the attenuation of reflection amplitudes from the soil surface (i.e., surface reflection method). The Topp petrophysical empirical relationship [Topp et al., 1980] was then used for converting dielectrics into moisture. Therefore, such moisture values were locally compared with the volumetric water contents from eight capacitance probes evenly placed over the entire surveyed area. From now on, this first approach will be referred to as the "surface reflectivity method".
The second method, which will be referred to as the "Rayleigh scattering method", uses a Rayleigh scattering-based approach for retrieving the peaks of the frequency spectra from the signals collected in the time domain [Benedetto, 2010], so that a proxy of the subsurface moisture spatial field can be generated.

3.3 Theoretical background

3.3.1 The surface reflectivity method

It is well-known that the electromagnetic characteristics of materials affect the amplitude of the received GPR signals. In particular, the relative dielectric permittivity of soil is widely influenced by the amount of water in soil pore spaces, due to much lower values of the solid matrix permittivity compared to the permittivity of water. Then, the variations of

signal amplitudes are very sensitive to moisture content, and the higher the differences between the dielectric permittivities of adjacent interfaces, the greater will be the reflected amplitudes.
Within the framework of surface reflection methods, θ is estimated by comparison between the reflection coefficient of the air-soil interface and the reflection coefficient of the air-perfect electric conductor (PEC) [Davis and Annan, 2002; Ghose and Slob, 2006; Serbin and Or, 2004-2005].
Theoretically, the reflection coefficient can be expressed as follows:

$$R = \frac{1-\sqrt{\varepsilon_r}}{1+\sqrt{\varepsilon_r}} \tag{3.3.6}$$

where ε_r is the soil permittivity that can be determined from the measured amplitude A_r, and the amplitude A_m of the wave reflected from a PEC (e.g., a metal plate larger than the footprint of the radar) [Davis and Annan 2002, Redman et al. 2002], following the relationship given by:

$$\varepsilon_r = \left(\frac{1+\frac{A_r}{A_m}}{1-\frac{A_r}{A_m}} \right)^2 \tag{3.3.7}$$

Evaluation of θ by this technique thus occurs as a function of wave amplitudes, and it is not related to measurement of travel time through the medium e.g., in case of the previous permittivity evaluation methods. According to Huisman et al. [2003], the depth domain of such technique can cover the top 20 cm of soil. On the contrary, Serbin and Or [2004] estimated that such influence is concerned to only the top 1 cm of soil. The main drawbacks of this technique concern *i)* the high dependence on surface roughness, such as in case of vegetation, as the reflection coefficient R is reduced by scattering from the combination of both varying θ profiles and roughness. Moreover, *ii)* in case of lower θ values, this technique is very sensitive to θ variation.

Once the relative dielectric permittivity is estimated using Equation (3.3.7), the volumetric water content θ [$m^3 \cdot m^{-3}$] can be retrieved by inverting the following site-specific petrophysical relationship [Topp et al., 1980]:

$$\varepsilon_r = 1.74 - 0.34 \cdot \theta + 135 \cdot \theta^2 - 55.3 \cdot \theta^3 \quad (3.3.8)$$

Amongst the various site-specific relationships proposed by Topp's research, such expression is characterized by one of the lower errors of permittivity estimate, e.g., 0.38, to which an error of 1.8×10^{-2} for the estimate of θ is associated.

3.3.2 The Rayleigh scattering method

A recent method based on signal processing in the frequency domain was proposed by Benedetto [2010]. The main point of strength relies on the not need for destructive core sampling to calibrate the system, such that the volume fractions of the three phases in the medium are not accounted for. In that regard, θ can be directly estimated by frequency analysis of the GPR signal without evaluating the dielectric permittivity. The main assumption concerns that in unsaturated soils electromagnetic waves are scattered by water droplets [Drude, 1902], thereby a shifting of the frequency of the waves occurs [Bekefi and Barrett, 1987; Bohren and Huffman, 1983].
Rayleigh scattering is used to explain the shifting of the frequency of the scattered signals. A shift in the frequency distribution of the reflected signals has already been observed in the past, although the cause of such shift was not identified or investigated. Narayana and Ophir [1983] analysed ultrasonic waves reflected by normal and fatty livers, thus noticing that different frequencies were attenuated in different media. The authors identified the Rayleigh scattering as the primary cause of the observed non-linear behavior of the reflected waves in fatty livers. In particular, Rayleigh scattering was originated by the presence of fat globules, which exhibit fourth-order frequency dependence. More recently and with respect to another field of application, Ho et al. [2004] showed that a frequency shift occurs for the detection of buried mines with different shapes and sizes.

It is well-known that scattering is generated by singularities or non-homogeneities in electromagnetic impedance. The process is described as Rayleigh scattering whether the dimensions of these non-uniformities are much smaller than the wavelength of the EM wave. The size of a scattering particle can be defined analytically by the ratio $x = 2\pi r / \lambda$, with r being the radius of the particle, and λ being the wavelength of the signal. By definition, Rayleigh scattering occurs in the small size parameter regime x

≪ 1. Scattering from larger spherical particles is explained by Mie [1908] for an arbitrary size parameter *x*. The Mie theory reduces to the Rayleigh approximation when small values of *x* are considered.
More details on this theory are thoroughly discussed in Chapter 2, Subsection 2.1.3.

By means of both several assumptions on the three-phase porous medium properties and simplifications of the physics, Benedetto [2010] defined the following formulation:

$$I(\theta, f) = I_0(f)\frac{1+\cos^2\theta_s}{2R^2}\left[\frac{2\pi f}{c_0}\sqrt{\mu_r\left(\varepsilon_\infty + \frac{\Delta\varepsilon}{1+f^2\tau^2}\right)}\right]^4\left[\frac{\mu_r\left(\varepsilon_\infty + \frac{\Delta\varepsilon}{1+f^2\tau^2}\right)-1}{\mu_r\left(\varepsilon_\infty + \frac{\Delta\varepsilon}{1+f^2\tau^2}\right)+2}\right]^2\left(\frac{d}{2}\right)^6 \quad (3.3.9)$$

where R is the distance between the observer and the particle, θ is the angle of scattering, f is the frequency of the electromagnetic signal, c_0 is the velocity of free space, μ_r is the magnetic permeability, ε_∞ is the dielectric constant of the full-polarized medium at an infinite frequency electromagnetic field, $\Delta\varepsilon = \varepsilon_{static} - \varepsilon_\infty$ is the difference between the permittivities of a steady and an infinite frequency electromagnetic field, τ is the relaxation time, and d is the diameter of the particle. A non-linear modulation of the electromagnetic signal is produced by scattering, as a function of the moisture content. In this regard, the peak of frequency has been demonstrated to be as a comprehensive indicator, negatively related to moisture. Overall, since scattering is caused by water in the medium, more scattering events are expected as the moisture content increases.
According to Equation (3.3.9), the various frequency components of the frequency spectra are differently scattered, depending on the soil type and water content. Then, the peak of the frequency spectrum f_p corresponds to the frequency component with the maximum scattered intensity of the EM wave. A regression law, based on experimental evidences, was proposed to predict moisture content θ, expressed in %, from the value of the peak of frequency f_p, expressed in Hz×10^8:

$$\theta = (A - f_P)/B \quad (3.3.10)$$

where A and B are regression coefficients. Table 3.1 lists the values of A and B and the regression coefficients for five different soils [Benedetto, 2010].

3.4 Experimental framework

3.4.1 Tools and equipment

A GPR with two ground-coupled antennas, 600 MHz and 1600 MHz center frequencies (RIS 2k-MF Multi Frequency Array Radar-System, manufactured by IDS Ingegneria dei Sistemi S.p.A., Italy) was used for the surveys. Measurements were carried out using 4 channels, 2 mono-static and 2 bi-static.

A detailed description of this radar instrument is provided in Appendix A, Subsection A.1.1.2.

Data were acquired in the time domain, with a 40 ns time window and a time step $dt = 7.8125\times10^{-2}$ ns. Horizontal sampling resolution amounted to 2.4×10^{-2} m. According to the main goal of this study, only the 600 MHz mono-static channel was processed. The 1600 MHz mono-static signal and the remaining two bi-static channels were used for cross-checking.

Capacitance probes WaterScout SM100 manufactured by Spectrum Technologies Inc. (Figure 3.2) were fairly evenly placed over the entire surveyed area, collecting data at depths of 0.15 m and 0.45 m below the ground surface to provide point information on subsurface moisture content. According to the depth domain of the soil dielectric permittivity assessed by Equation (3.3.7), only data related to 0.15 m deep were used for comparison.

Capacitance probes were calibrated by gathering undisturbed soil samples of the same volume of the support explored by the probe, the closer to the sampling points.

The gravimetric water content w [$g\cdot g^{-1}$] was measured in laboratory environment and transformed in volumetric water content θ, so that the site-specific calibration curve could be determined. A relatively good agreement was found between the direct (w) and indirect (θ) soil moisture measurements as the mean absolute relative error and the coefficient of determination were 13% and 0.89, respectively (Figure 3.3).

Table 3.1: Parameter values of the model from Equation (3.3.10) for five different types of soil [Benedetto, 2010].

	Sandy soil	Alluvial soil	Subgrade material (Sm)	Sm + 5% clay	Sm + 20% clay	Average value
$A\times10^{8}$	5.7	7.0	6.2	5.6	5.3	5.7
$B\times10^{7}$	1.1	2.1	2.3	1.7	1.5	1.4

Figure 3.2: Capacitance probe WaterScout SM100, manufactured by Spectrum Technologies, Inc., USA.

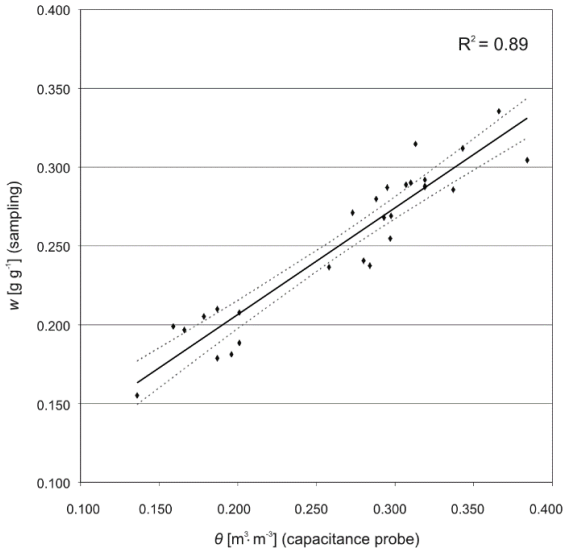

Figure 3.3: Site-specific calibration curve for capacitance probes relating gravimetric (*w*) and volumetric water content (θ).

3.4.2 Study site, weather conditions, and soil properties

The test site is situated in the Po valley in northern Italy, near the town of Landriano (9° 16' 12" E, 45° 19' 23" N), as illustrated in Figure 3.4.
The average elevation is 88 m a.s.l., with an almost flat ground along the entire surveyed field. The area is characterized by a semi-humid climate with mean annual precipitation and temperature of 880 mm and 12 °C, respectively. Soil type is a pretty uniform, bare, sandy loam characterized by a low surface roughness, with an average amplitude of 0.05 m. Table 3.2 lists the grain size distribution of a representative soil sample collected within the test site area.

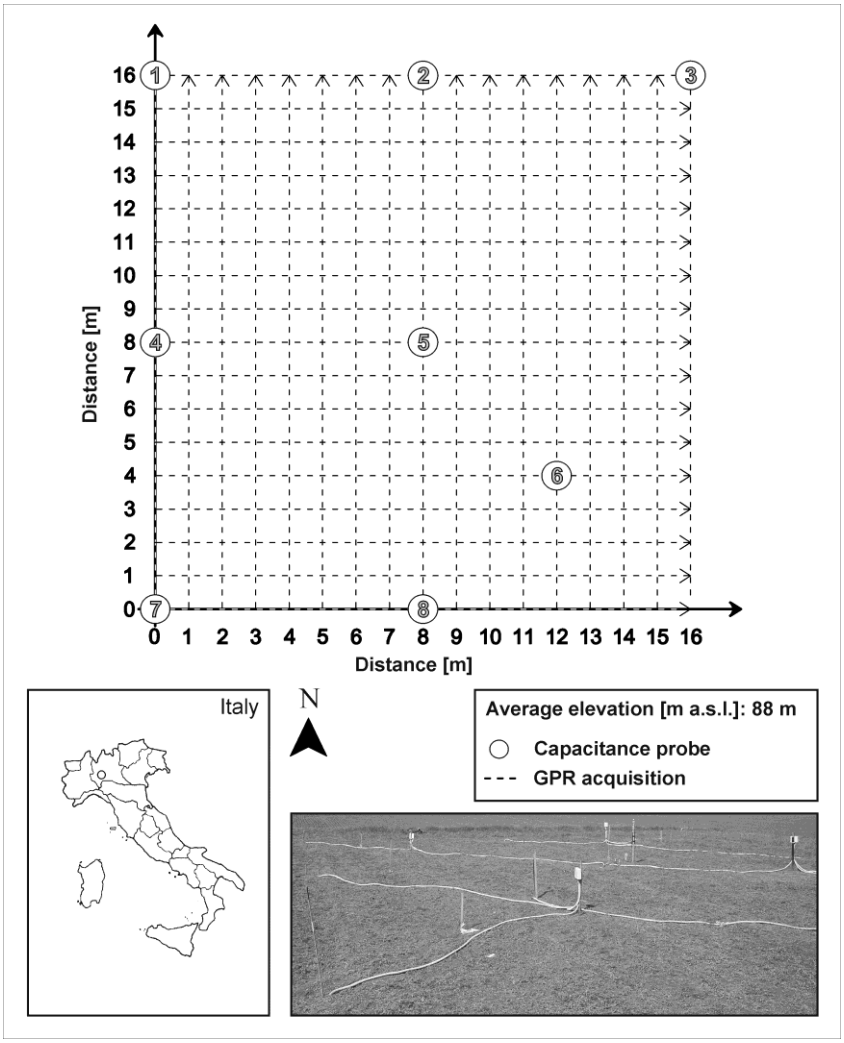

Figure 3.4: Study site for the GPR acquisition carried out over a 16m×16m area, 1-m spacing between the tracks (17×17 lines square grid pattern).

Table 3.2: Grain size distribution of a relevant soil sample collected within the test site area.

	Grain size			
Sieve [mm]	$P_{4.75}$	P_{2}	$P_{0.425}$	$P_{0.075}$
Soil Fraction [%]	99.03	98.51	91.66	53.23

The GPR campaign took place at the beginning of autumn, on October 2nd, 2012, in moderately wet conditions. According to the nearest rain gauge station, low rainfall was recorded during the previous seven days (≤ 8 mm/day, on the average), with a medium level of evaporation due to the medium-high temperatures in that period (17 °C, on the average).
A 16m×16m field was surveyed by using GPR, following a 17×17 lines square grid pattern with a spacing of 1 m between the acquisition tracks. The GPR system was dragged with a driving speed of about 3 km/h (almost 1 m/s). Overall, 21300 traces were gathered.
Furthermore, eight capacitance probes were fairly uniformly distributed over the surveyed area for collecting moisture 0.15 m depth below the ground surface in order to be compared with the soil moisture inferred through the surface reflectivity method.

3.5 Results and discussion

3.5.1 Punctual comparison of moisture data

A comparison between moisture data retrieved by GPR (θ_{GPR}) using the surface reflectivity method, and those inferred by eight capacitance probes (θ_{probe}) is shown in Figure 3.5.
An overall good agreement can be observed between the GPR-derived and the probe-measured moisture, with the exception of stations 5 and 6, where the absolute residuals are equal to 0.048 $m^3 \cdot m^{-3}$ and 0.067 $m^3 \cdot m^{-3}$, respectively. The average soil moisture from GPR over the eight probe stations amounts to 0.309 $m^3 \cdot m^{-3}$ with a standard deviation of 0.0105 $m^3 \cdot m^{-3}$. The same statistics concerning soil moisture from capacitance probes are equal to 0.318 $m^3 m^{-3}$ and 0.0292 $m^3 m^{-3}$, respectively.
In order to better analyse the reliability of GPR-derived soil moisture, the relative incidence of residuals [%], defined by the ratio between the relative value of the residual and the corresponding moisture value from capacitance probe, is taken into account. In that respect, residuals are considered as the differences between probe-measured and GPR-derived moisture data (Figure 3.6). Overall, with the exception of the two aforementioned outliers (i.e., stations 5 and 6), the variability of such incidences is observed within approximately the 8%. These mismatches can be reasonably due to the different support scale of the GPR-based technique, greater than the small-scale variability of soil moisture detected by capacitance probe.

3.5.2 Mapping of soil moisture spatial variability

3.5.2.1 Mapping of the normalized shallow subsurface dielectric water content from the surface reflectivity method

The field-average soil moisture inferred through the surface reflectivity method equals to 0.351 $m^3 \cdot m^{-3}$, with a standard deviation of 0.030 $m^3 \cdot m^{-3}$. Therefore, a slightly higher variability of near-surface moisture on the large scale is observed.

Concerning the spatial distribution of soil moisture, Figure 3.7 (a-b) illustrates the interpolated normalized subsurface soil moisture (θ_{NORM}) from the GPR acquisition. It is worth noting that given the rather homogeneous conditions of soil and vegetation, the surface roughness is not considered in the soil pattern.

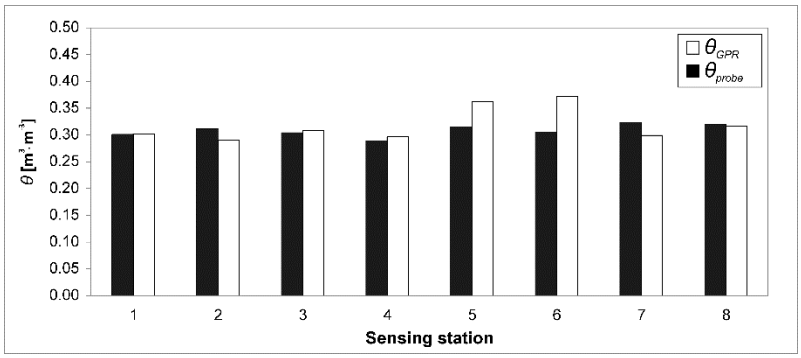

Figure 3.5: Bar graphs representing GPR-derived (θ_{GPR}) and probe-measured (θ_{probe}) soil moisture contents on the 8 probe sensing stations.

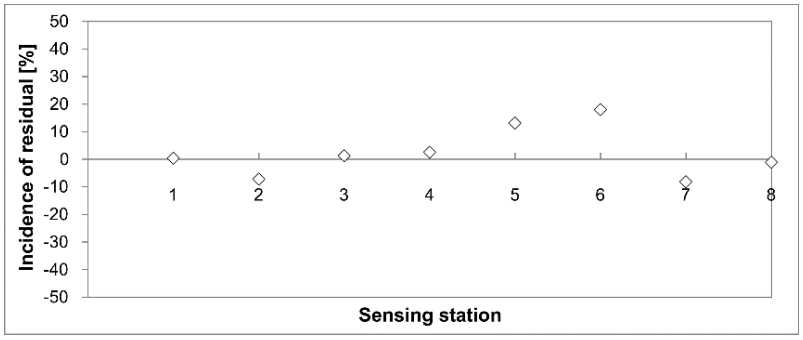

Figure 3.6: Incidence of moisture residuals on the 8 probe sensing stations.

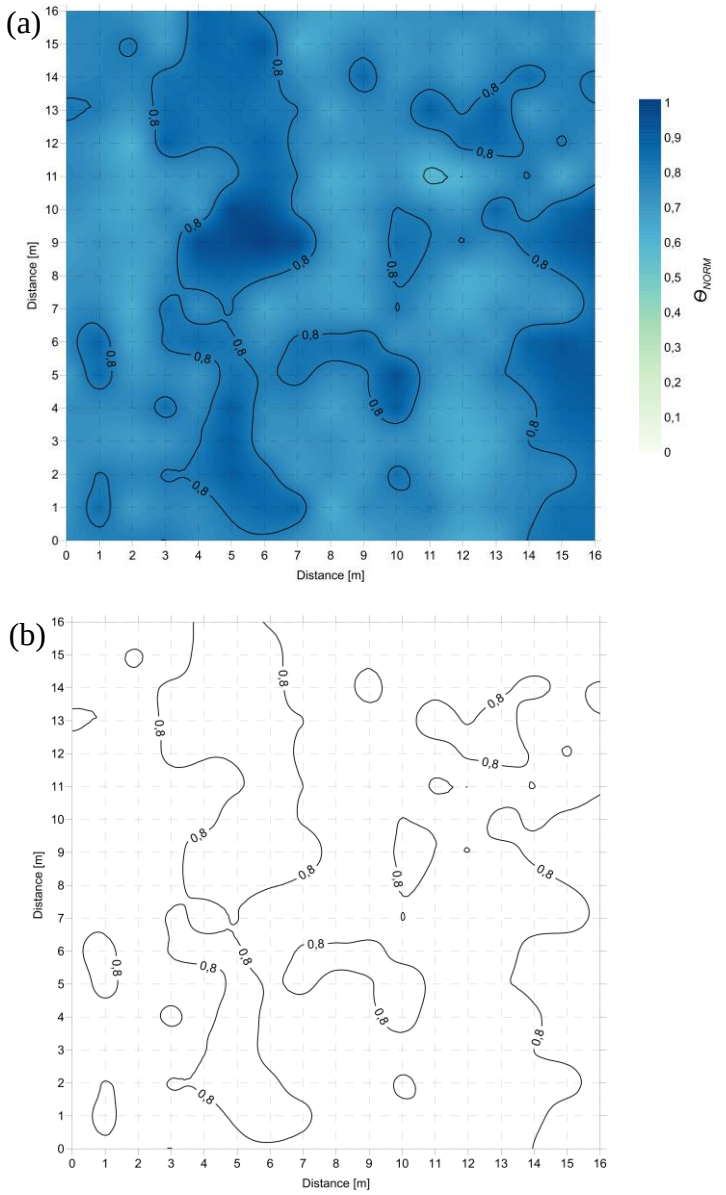

Figure 3.7: GPR-derived maps from the surface reflectivity method: (a) normalized shallow soil dielectric moisture (θ_{NORM}) map overlaid with iso-contour lines; (b) iso-contour lines of the normalized shallow soil dielectric moisture (θ_{NORM}) map.

The field-average normalized moisture amounts to 0.762, with a standard deviation of 0.082. The highest values of moisture content are encountered in two places, about 7 m from the northern edge of the surveyed area: one

spot is located at about 5.5 m from the western edge of the grid pattern, and the second one at the eastern edge. On the contrary, the driest areas can be observed in the middle of the western edge and close to the south-eastern corner of the area.

3.5.2.2 Mapping of the normalized frequency spectra peaks from the Rayleigh scattering method

Figure 3.8 shows the map of the interpolated normalized frequency peaks f_{PNORM} extracted from the frequency spectra of the received signals using the Rayleigh scattering method. According to the correlations found by Benedetto [2010] between shifts of frequency spectra peaks and subsurface moisture content variation, this map can be considered as a proxy of the near-surface moisture spatial field.

The field-average normalized frequency peak equals to 0.813, with a standard deviation of 0.068. Therefore, such method seems to account for a lower presence of wet spots over the entire area and a lower variability of moisture spatial distribution.

3.5.2.3 Comparison between maps from the GPR-based methods

Figure 3.9 shows the comparison between the iso-contour lines of subsurface moisture maps obtained by using both the methods overlaid over the normalized near-surface soil moisture map from the surface reflectivity method.

A good agreement with the theoretical expectations is demonstrated. In particular, a lowering of the peak of the frequency spectrum corresponds to an increase of dielectric permittivity, as the moisture content is expected to rise.

On the contrary, from a decrease of the relative dielectric permittivity and an increase of the value of frequency peak, a lowering of moisture content is expected. In this regard, a clear match can be found between the low normalized frequency peak values and the high normalized shallow subsurface dielectric moisture in the north-western part of the figure. Further matches can be observed in the middle of the western edge of the figure, as well as in the south-eastern corner. In such cases, high normalized frequency peaks values indicate low normalized volumetric water content. According to the theoretical expectations, as the water content in soil increases, the dimensions of the droplets increase and the film of water molecules around the solid particles becomes thicker.

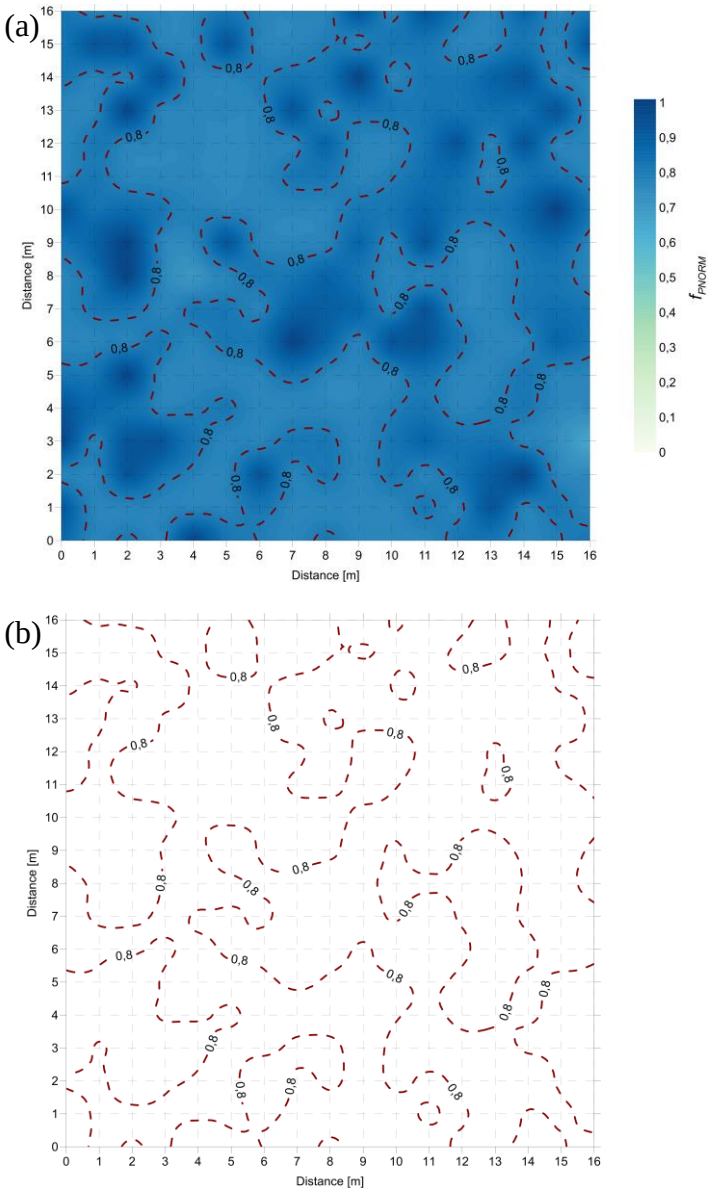

Figure 3.8: GPR-derived frequency peaks map from the Rayleigh scattering method: (a) normalized frequency peaks (f_{PNORM}) map overlaid with iso-contour lines; (b) iso-contour lines of the normalized frequency peaks (f_{PNORM}) map.

This produces a new distribution of the scattering centers in the medium, thereby causing the shift of the frequency component at the maximum intensity of the EM wave to lower values.

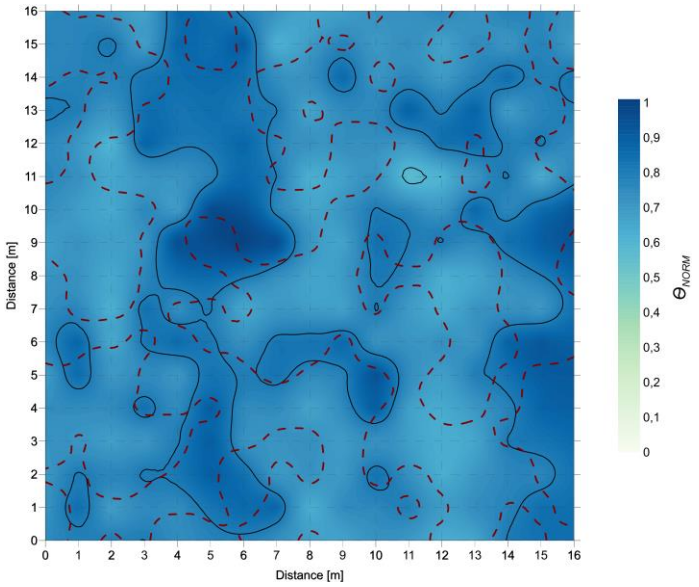

Figure 3.9: Normalized shallow soil dielectric moisture map overlaid with iso-contour lines from the "surface reflectivity" (solid black lines) and the "Rayleigh scattering" method (dashed red lines).

As regards mismatches between moisture spatial fields inferred from the amplitude and from the frequency of the GPR signal, differences can be reasonably related to possible dispersive effects of the soil affecting the frequency peaks, such as fine size particles.

3.6 Conclusion

The paper proposes the application of two GPR-based approaches for monitoring soil moisture spatial field in pavement inspections, to prevent structural damaging. A GPR survey, including 21300 records over a 16m×16m field, was carried out. Local comparisons were developed between the GPR-derived and the probe-measured moisture contents. Moreover, subsurface maps of both normalized shallow subsurface dielectric moisture and normalized frequency spectra peaks were processed.

Although some discrepancies are shown concerning local moisture comparisons, results demonstrate a greater effectiveness of the proposed GPR approaches for large-scale inspections, consistent with the dimension of the surveyed area.

Overall, this study, relying on the application of the two proposed approaches based on the amplitude analysis (i.e., surface reflectivity

method) and the frequency analysis (i.e., Rayleigh scattering method) of the GPR signal, proves that: *i)* subsurface moisture content at the small scale (area ≤ 0.01 m^2) can be effectively inferred by permittivity evaluation through GPR and the use of site-specific empirical petrophysical relationships from Topp; *ii)* estimation of spatial variability of subsurface moisture through the Rayleigh scattering method matches relatively well the prediction of moisture spatial distribution from the surface reflection method, thereby allowing for the use of a self-consistent method without the need of any petrophysical relationship. Such encouraging result follows recent findings from Benedetto et al. [2012a], wherein the Rayleigh scattering method was used to detect water content on a rural road network in order to identify landslide areas along road routes. Along with this high-performing processing technique, a high efficiency was also ensured by the use an off-ground radar system, whose details are described in Appendix A, Subsection A.1.2.1.

4. Clay content evaluation in pavement

4.1 Introduction

The evaluation of clay content in soils is significant for many applications such as agriculture [Robinson and Phillips, 2001], construction [Miqueleiz et al., 2012], geotechnical stability analyses [Abusharar and Han, 2011], and for the assessment of the bearing capacity of soils for structural foundations. Generally, the presence of clay in cohesive soils is strictly related to moisture, by virtue of its strong hygroscopic capacity [Sdiri et al., 2011]. This co-action, along with the variability of climatic and seasonal environmental conditions, can be considered as the main cause of instability behavior of soils under load.

Traditionally, the hydrodynamic behavior of plastic soils is modeled during wetting–drying cycles [Dudoignon et al., 2007]. The properties of clayey soils under compressive or drying stress cycles are greatly influenced by particle arrangements and their mineralogical nature [Richard et al., 2001]. Beroya et al. [2009] demonstrated that the cyclic behavior of silt–clay mixtures is mainly governed by clay minerals abundance. In particular, given the same amount of clay/clay mineral and/or the same value of plasticity index, the montmorillonitic soils have higher cyclic strength than the illitic and kaolinitic soils. Therefore, the clay fraction and plasticity index are unreliable indicators of the liquefaction susceptibility of cohesive soils, without considering the clay mineralogy and its different adhesive bond strength exerted on the boundary particles. Model-scale tests are generally used to assess the volumetric changes of clay materials in gravimetric moisture domains within the liquidity limit (w_L) and the shrinkage limit (w_S) [Chertkov and Ravina, 2000]. In the unsaturated domain, the shrinkage curves and the associated size of cracks vary with respect to the scale of investigation [Voltz and Cabidoche, 1995]. Therefore, in-situ consequences of clayey soils drying typically are: development of shrinkage cracks with associated vertical prism-like structure [Chertkov, 2005], and subsidence effects [Hallaire, 1987].

In pavement engineering, different procedures have been developed to constrain the effects of clay content in soils for both road construction and rehabilitation. Abdi et al. [2009] investigated the possibility of strength improvement of clays reinforced with geogrids embedded in thin layers of

sand. Treatments of soils with additives such as cement, lime, fly ash, and chemicals are also widely used [Pakbaz and Alipour, 2012]. Moreover, the use of extra reinforcing steel to foundations and slabs is widespread, as well as earthmoving operations to remove the unstable cohesive material [Wood et al., 1995]. Core sampling is the most used technique to evaluate clay content in soils. This method is characterized by a high accuracy, although it is invasive, expensive, and time-consuming. Moreover, the significance of such kind of punctual analysis is very low for road engineering purposes, due to the long distances to be surveyed.

Several non-destructive methods can be applied to indirectly monitor the clay fractions in soils. Measurements are provided by the light falling weight deflectometer (LFWD) [Benedetto et al., 2012c] and the time domain reflectometry minor destructive system (TDR) [Fellner-Feldegg, 1969]. LFWD is used to evaluate the resilient modulus of soils, for which correlations with fine-grained and cohesive soils have been provided [George, 2000]. Research have been also carried out with the TDR system for monitoring the water content in clayey soils [Stangl et al., 2009]. Several other methods have been developed to directly assess clay fractions in soils, on the basis of advanced very high-resolution radiometer (AVHRR) [Odeh and McBratney, 2000], and vis–NIR spectroscopy data [Viscarra Rossel et al., 2009]. However, most of these non-destructive tools for direct and indirect assessment of clay content are not time-efficient and not effective for wide roads inspection and maintenance, since they provide only local measurements.

Electromagnetic methods depend on the evaluation of the relative permittivity, generally assessed from the time delay of pulses reflections [Benedetto, 2004] or from the amplitudes and arrival times of the transmitted and reflected signals [Al-Qadi et al., 2004]. These approaches require preventive calibration to evaluate the EM wave velocity into the medium; hence, the use of core sampling is needed to define characteristics and conditions of materials. Nowadays, enhanced and self-consistent approaches are spreading out based on the GPR signal processing in the frequency domain, with the main objective to raise both the efficiency and effectiveness of subsurface surveys. Lambot et al. [2004] studied the imaginary part of the dielectric permittivity as a function of the frequency of investigation, to assess the electrical properties of soils. In particular, the GPR response in the frequency and time domains is processed using Green's functions combined with an intrinsic antenna model in a full-wave inversion framework. The validation of this method demonstrated an

excellent agreement between the GPR-derived values and reference TDR measurements of permittivity. In addition, this technique also showed high effectiveness for non-destructive testing of building materials [Patriarca et al., 2011].
Another approach was based on the use of a non-linear inversion algorithm in the frequency domain for the evaluation of shallow soil properties [Oden et al., 2008]. In particular, the early-time arrivals of signals were analysed, based on their amplitude and shape modulation with different configurations of antenna standoff and soil dielectric characteristics [Pettinelli et al., 2007b]. More recently, Benedetto [2010] presented another self-consistent method without the need of a petrophysical relationship and calibration of the GPR system. The details of this technique are thoroughly discussed in Subsection 3.3.2.

4.2 Methodology and objective

In this Chapter, the ability of GPR to evaluate clay content in soils is analysed using different signal processing techniques. Three types of soils classified by AASHTO [2011] as A1, A2, and A3 were used and bentonite clay was gradually added from 2% to 25% by weight. The consistency of results was validated by the Rayleigh scattering method, the full-waveform inversion, and the time-domain signal picking techniques.
The main objectives of this work are *i)* to provide a contribution to road safety by preventing the risk of severe damage of pavement, which is induced by clay content in sub-asphalt layers, and *ii)* to improve the operations of rehabilitation and maintenance through effective GPR inspections.
The specific objective of the research is the evaluation of clay content with GPR, through different signal processing techniques. These methods are applied in subgrade and sub-base soil samples using different GPR systems.

4.3 Theoretical background

4.3.1 Rayleigh scattering technique

The details of this technique are thoroughly discussed in Subsection 3.3.2.2. In this Chapter, the Rayleigh scattering method is applied for the evaluation of clay content in soils under dry conditions, according to recent research on the behavior of clay particles in atmospheric air, under the application of an external EM field [Rozynek et al., 2012].

Therefore, the regression law used to predict clay content can be expressed as follows:

$$clay = (A - f_P)/B \tag{4.3.1}$$

where *clay* is the clay content, expressed in %, *A* and *B* are regression coefficients, and f_p is the value of the peak of frequency, expressed in Hz×10^8.

4.3.2 Full-waveform inversion technique

4.3.2.1 Antenna equation in the frequency domain

In the intrinsic far-field antenna model of Lambot et al. [2004], which applies to planar layered media, a local plane wave field distribution is assumed for the backscattered field over the antenna aperture, and hence, an equivalent single electric dipole approximation holds for describing the antenna radiation properties. Relying on the linearity of Maxwell's equations, wave propagation between the point source or field point and the radar transmission line reference plane is accounted for by means of complex, frequency-dependent global reflection, and transmission coefficients. These reflection and transmission coefficients determine the antenna and transmission line internal transmissions and reflections, and thereby antenna–medium interactions are inherently accounted for. The radar equation expressing the relation between the radar-measured field and the 3-D layered medium Green's functions is described in the frequency domain as follows [Lambot et al., 2004]:

$$S_{11}(\omega) = \frac{b(\omega)}{a(\omega)} = R_i(\omega) + \frac{T(\omega)G_{xx}^{\uparrow}(\omega)}{1 - R_s(\omega)G_{xx}^{\uparrow}(\omega)} \tag{4.3.2}$$

where $S_{11}(\omega)$ denotes the raw radar signal expressed here as the ratio between the backscattered field $b(\omega)$ and incident field $a(\omega)$ at the radar transmission line reference plane, with ω being the angular frequency, $R_i(\omega)$ is the global reflection coefficient of the antenna in free space, $T(\omega)=T_i(\omega)T_s(\omega)$ with $T_i(\omega)$ being the global transmission coefficient for fields incident from the radar reference plane onto the point source and $T_s(\omega)$ being the global transmission coefficient for fields incident from the field point onto the radar reference plane, $R_s(\omega)$ is the global reflection coefficient for the field incident from the layered medium onto the field point, and $G_{xx}^{\uparrow}(\omega)$ is the layered medium Green's function.

4.3.2.2 Green's function

The Green's function is defined as the scattered *x*-directed electric field $E_x(\omega)$ at the field point for a unit-strength *x*-directed electric source $J_x(\omega)$ at the source point. The Green's function can be derived using a recursive scheme to compute the global reflection coefficients of the multi-layered medium in the spectral domain. The transformation back to space domain is performed by evaluating the semi-infinite integral with a fast numerical procedure [Lambot et al., 2007]. The antenna characteristic coefficients can be determined by solving a system of equations similar to Equation (4.3.2) with different known Green's functions corresponding to different configurations for which the radar measurements are performed (e.g., measurements with the antenna at different heights over a copper sheet). It is worth noting that once the antenna characteristic functions are known, the antenna effects can be fully filtered out from the raw radar data $S_{11}(\omega)$ to derive the measured medium Green's function $G_{xx}^{\uparrow}(\omega)$.

4.3.2.3 Model inversion and objective function

The application of inverse modeling for subsurface parameter assessment is a problem of non-linear optimization, with the main goal to find the parameter vector $\mathbf{b} = [\varepsilon_n, \sigma_n, h_n]$, $n = 1,\ldots, N$, where N is the number of medium layers, by the minimization of an objective function $\varphi(\mathbf{b})$. Regarding the components of vector **b**, the combination of them for the n^{th} layer includes ε_n as the dielectric permittivity, σ_n [Sm^{-1}] as the electrical conductivity, and h_n [m] as the thickness of the layer. In particular, the electrical conductivity σ is frequency-dependent assuming a linear relationship, valid if the bandwidth is not too large [Lambot et al., 2005]:

$$\sigma(f) = \sigma_{f\min} + a(f - f_{\min}) \tag{4.3.3}$$

where $\sigma_{f\,min}$ is the reference apparent electrical conductivity at the minimum frequency, and the medium-specific constant a is the linear variation rate of $\sigma(f)$.

The objective function $\varphi(\mathbf{b})$ to minimize is given by:

$$\varphi(\mathbf{b}) = \left(\frac{\sum_{f_{\min}}^{f_{\max}} \left| G_{xx}^{*\uparrow} - G_{xx}^{\uparrow} \right|^2}{\sum_{f_{\min}}^{f_{\max}} \left| G_{xx}^{*\uparrow} \right|^2} \right)^{\frac{1}{2}} \tag{4.3.4}$$

where $\boldsymbol{G}_{\boldsymbol{xx}}^{*\uparrow} = G_{xx}^{*\uparrow}(\boldsymbol{\omega})$ and $\boldsymbol{G}_{\boldsymbol{xx}}^{\uparrow} = G_{xx}^{*\uparrow}(\omega\ \mathbf{b})$ are the vectors accounting the observed and simulated Green's functions, respectively. The solution of this minimization is found by using the global multilevel coordinate search (GMCS, [Huyer and Neumaier, 1999]) sequentially combined with the Nelder-Mead Simplex algorithm [Lambot et al. 2002], as the non-linearity of the problem usually lead to multiple local minima.

4.3.3 Time-domain signal picking

This technique relies on the fundamentals of the electromagnetic theory, whose details can be found in Chapter 2, Subsection 2.1.2. According to this theory, it is possible to express the following relationship:

$$v = c \Big/ \sqrt{\varepsilon_r^{'}} \tag{4.3.5}$$

where c is the speed of light in free space, ε_r' is the real part of the relative dielectric permittivity, and v is the EM wave propagation velocity in the medium.

Therefore, by considering that the time delay Δt between two reflected pulses at the layer interfaces depends on the medium thickness h according to the following expression:

$$h = (v \cdot \Delta t)/2 \tag{4.3.6}$$

it is possible to estimate v from Equation (4.3.6), thus to retrieve the value of the ε_r' from Equation (4.3.5).

4.4 Experimental framework

4.4.1 Experimental design

The experimental design is aimed to obtain a reliable evaluation of clay content in sub-asphalt layers and subgrade soils. Typical road material for sub-base and subgrade construction was used. Clay was gradually added at different known contents.

Preliminary procedures were carried out for adequately mixing and compacting the investigated soil samples. The mixing protocol provides the use of a known quantity of iron filings, mixed with the undisturbed loose material at different time steps, and randomly sampled to assess the homogeneity of the mixture.

Tests showed that a clay initial rate at 2% by weight was uniformly distributed into the investigated volume. Moreover, different time steps of vibration were carried out to analyse the grade of compaction of the samples. The obtained values of density showed that beyond 60 s of vibration, compaction remains fairly constant. Further comparisons with the values of compaction by Standard Proctor tests [American Society for Testing and Materials, 2007a], demonstrated a high consistency of the outcomes from the mixing procedure with those arising from the modified Proctor with large mold. The bulk density of each soil sample was collected, as well as the real density of the mixtures, for cross checking. Measurements were carried out using two different GPR instruments, as will be described later.

4.4.2 Test devices and equipment

Two different GPR systems were used for the analysis. An ultra wideband (UWB) stepped frequency continuous wave (SFCW) radar was set-up using a vector network analyzer (VNA) HP 8573C, manufactured by Hewlett Packard Company, USA. Data were acquired in a bandwidth from 1 GHz to 3 GHz. The signal was sampled in the frequency domain at 1282 frequencies with a ~1.56 MHz frequency step.

Another radar with ground-coupled antennas (pulseEKKO PRO 500, manufactured by Sensors & Software Inc., Canada), 500 MHz center frequency, was used in a bi-static configuration and common offset. Data were acquired in the time domain, with a 40 ns time window and a time step $dt = 5\times10^{-2}$ ns.

More details about both these radar systems are described in Appendix A, Subsections A.1.1.3 and A.2.1.

Radar measurements were carried out under controlled laboratory conditions (laboratory temperature 19°C ± 2.5°C; relative humidity 45% ± 15%; absolute pressure about 1 atmosphere). Soil samples were located in electrically and hydraulically isolated boxes that measure 0.45 m×0.55 m×0.12 m, so that their reference useful dimension is 0.40 m×0.47 m×0.105 m.

Beneath each soil sample, a perfect electric conductor consisting of a copper sheet, allowed to completely reflect the waves propagating through the investigated material. In particular, this small layer prevents from the propagation of the EM waves through the floor, thereby preventing noise or disturbances that may arise from undesired reflections of the underneath load-bearing material.

4.4.3 Materials and laboratory testing

Road material, typically employed for unbound pavement layers and subgrade soils was used. In particular, three different soil types, classified by AASHTO [2011] as A1, A2, and A3 were tested. Figure 4.1 (a), (b), and (c) show gravel (A1 AASHTO group, grain size 4-8 mm), coarse sand (A2 AASHTO group, grain size 1-2 mm), and fine sand (A3 AASHTO group, grain size 0.125-0.250 mm), respectively. Bentonite clay (Figure 4.1 (d)) was gradually added from 2% to 25% by weight, in steps of 2% and 5%.
The mineralogy of this clay is mainly composed by smectite, whose mineral consists of silica (62% by weight) and alumina (21% by weight) sheet-like units, tied together. Moreover, a chemical analysis showed a considerable rate of crystal water (5.5% by weight). Table 4.1 summarizes the main physical properties (assuming ρ_s as the particle density, and ρ_{bulk} as the bulk density of materials, both expressed in [$10^6 \times g/m^3$]), and the grade of the bentonite clay.

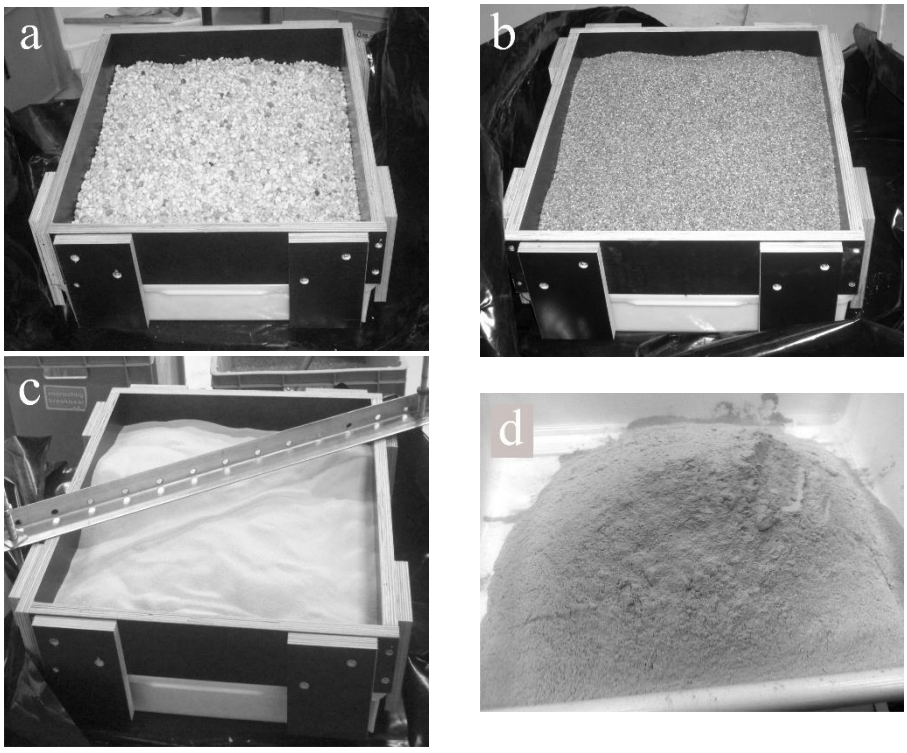

Figure 4.1: Typical road materials used for the tests: (a) A1 gravel; (b) A2 coarse sand; (c) A3 fine sand; (d) bentonite clay.

Table 4.1: Main physical properties, grade, and classification of the bentonite clay used for the experiments.

Material	Granulometric analysis			Main physical properties			
	$P_{0.125}$	$P_{0.090}$	$P_{0.063}$	ρ_s	ρ_{bulk}	Water absorption	
	[%]	[%]	[%]	$10^6\times$ [g/ m^3]	$10^6\times$ [g/ m^3]	$10^{-3}\times$ [g/g]	$10^{-5}\times$ [l/g]
Bentonite clay	98	95	88	2.410	0.910	290	1000

Overall, twenty-seven tests were carried out, under dry conditions. By taking into account each soil type, growing percentages of clay amounting to 2 % by weight were added, from 0% up to 10% by weight. Subsequently, 5% amounts by weight of this material were gradually added, up to the final investigated rate of 25% by weight of clay content. At the end of the mixing and compacting procedures, the bulk density of each soil sample was measured.

Moreover, the particle density of the samples was measured with a gas pycnometer (Ultra pycnometer 1000, manufactured by Quantachrome). Table 4.2 lists the main physical properties (being *n* and *e* the porosity [%] and the void ratio [%], respectively), particle size references, and AASHTO classifications of the tested soil samples.

4.5 Results and discussion

4.5.1 Clay content estimation–Rayleigh scattering method

In order to remove noise from the signal, low-pass and high-pass filters were used. A fast Fourier Transform (FFT) was employed to extract the frequency spectrum of the GPR signal collected through the pulsed radar system.

The frequency peak of the spectrum f_P, which is the element of the signal characterized by the largest intensity, was measured for different clay contents.

To improve the accuracy of the processing, an average value of the frequency peaks $f_{\bar{P}}$ was considered in case of non-unique values extracted from the FFT in the same test, sample by sample. This operation can be described as follows:

$$f_{\bar{P}} = \frac{1}{n}\sum_{i=1}^{n} f_{P_i} \tag{4.5.7}$$

Table 4.2: Main physical properties, particle size references, and AASHTO classifications of the surveyed soil samples.

Soil sample identification	Grade, classification, and clay content			Main physical properties			
	Grain size range (undisturbed) [m×10^{-3}]	AASHTO group (undisturbed)	Clay content [%]	ρ_s 10 ^{6}×[g/ m^3]	ρ_{bulk} 10 ^{6}×[g/ m^3]	n [%]	e [%]
Sample 1	4 - 8	A1	0	2.652	1.515	42.876	75.058
Sample 2	4 - 8	A1	2	2.652	1.544	41.777	71.755
Sample 3	4 - 8	A1	4	2.649	1.541	41.845	71.954
Sample 4	4 - 8	A1	6	2.648	1.547	41.572	71.150
Sample 5	4 - 8	A1	8	2.646	1.591	39.895	66.374
Sample 6	4 - 8	A1	10	2.643	1.592	39.751	65.979
Sample 7	4 - 8	A1	15	2.639	1.581	40.102	66.952
Sample 8	4 - 8	A1	20	2.629	1.587	39.620	65.619
Sample 9	4 - 8	A1	25	2.618	1.565	40.220	67.281
Sample 10	1 - 2	A2	0	2.657	1.598	39.859	66.275
Sample 11	1 - 2	A2	2	2.655	1.568	40.927	69.282
Sample 12	1 - 2	A2	4	2.651	1.568	40.860	69.091
Sample 13	1 - 2	A2	6	2.648	1.556	41.217	70.116
Sample 14	1 - 2	A2	8	2.644	1.539	41.768	71.728
Sample 15	1 - 2	A2	10	2.640	1.577	40.279	67.444
Sample 16	1 - 2	A2	15	2.638	1.591	39.698	65.831
Sample 17	1 - 2	A2	20	2.627	1.618	38.399	62.336
Sample 18	1 - 2	A2	25	2.620	1.611	38.536	62.697
Sample 19	0.125 – 0.250	A3	0	2.659	1.535	42.276	73.238
Sample 20	0.125 – 0.250	A3	2	2.656	1.550	41.647	71.370
Sample 21	0.125 – 0.250	A3	4	2.653	1.573	40.720	68.692
Sample 22	0.125 – 0.250	A3	6	2.651	1.555	41.370	70.561
Sample 23	0.125 – 0.250	A3	8	2.650	1.589	40.043	66.787
Sample 24	0.125 – 0.250	A3	10	2.646	1.594	39.746	65.965
Sample 25	0.125 – 0.250	A3	15	2.641	1.621	38.623	62.928
Sample 26	0.125 – 0.250	A3	20	2.628	1.634	37.829	60.847
Sample 27	0.125 – 0.250	A3	25	2.613	1.624	37.851	60.905

where n is the total amount of i replicas (i spectra), collected for each soil sample, and f_{P_i} is the frequency peak of the i^{th} spectrum. Figure 4.2 (a-b) illustrates two cases of stable (Figure 4.2 (a)) and unstable domain (Figure 4.2 (b)) values for the measured spectra.

The analysis of the measured data demonstrated that this variability of frequency peak values within the same test measurement, generally occurs in the boundary of two different and consecutive steps of frequency, wherein the shift of the spectrum approaches to be sensitive to the increase of clay content.

Hence, a problem of sampling resolution of the FFT occurs.

Figure 4.3 (a-c) shows the frequency modulations of the normalized spectra for the three investigated soils at different clay contents ranging from 0% (undisturbed soil sample) to 25% by weight.

It is evident that a systematic shift of the frequency peak to lower values of frequency occurs, for all the types of surveyed soils. In particular, an important negative correlation between the shift of the peak and the clay content is observed.

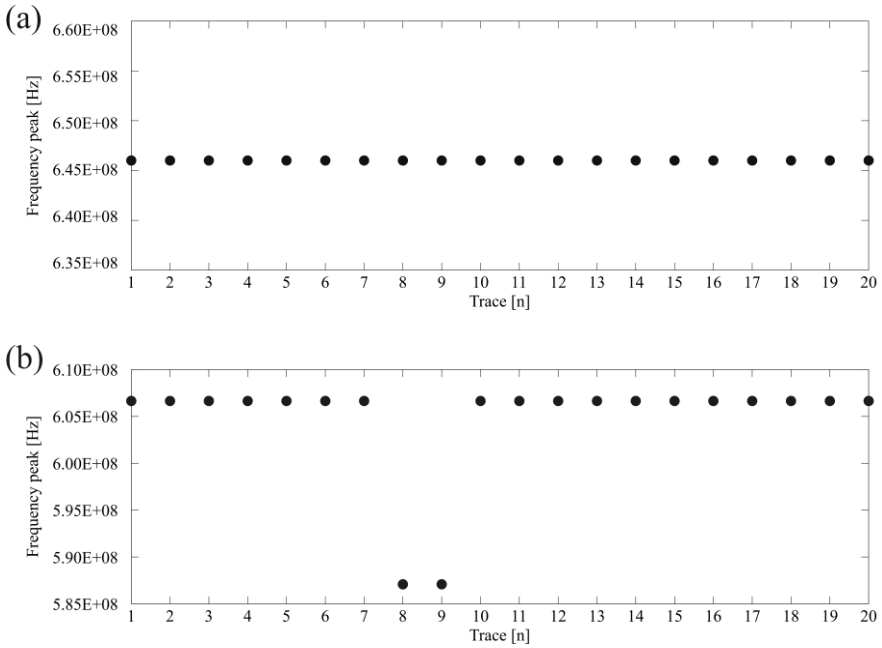

Figure 4.2: Measured frequency peak values extracted from the GPR signal spectra of each tested soil sample: (a) stable domain values, soil sample 21 (A3, 4% clay); (b) unstable domain values, soil sample15 (A2, 10% clay).

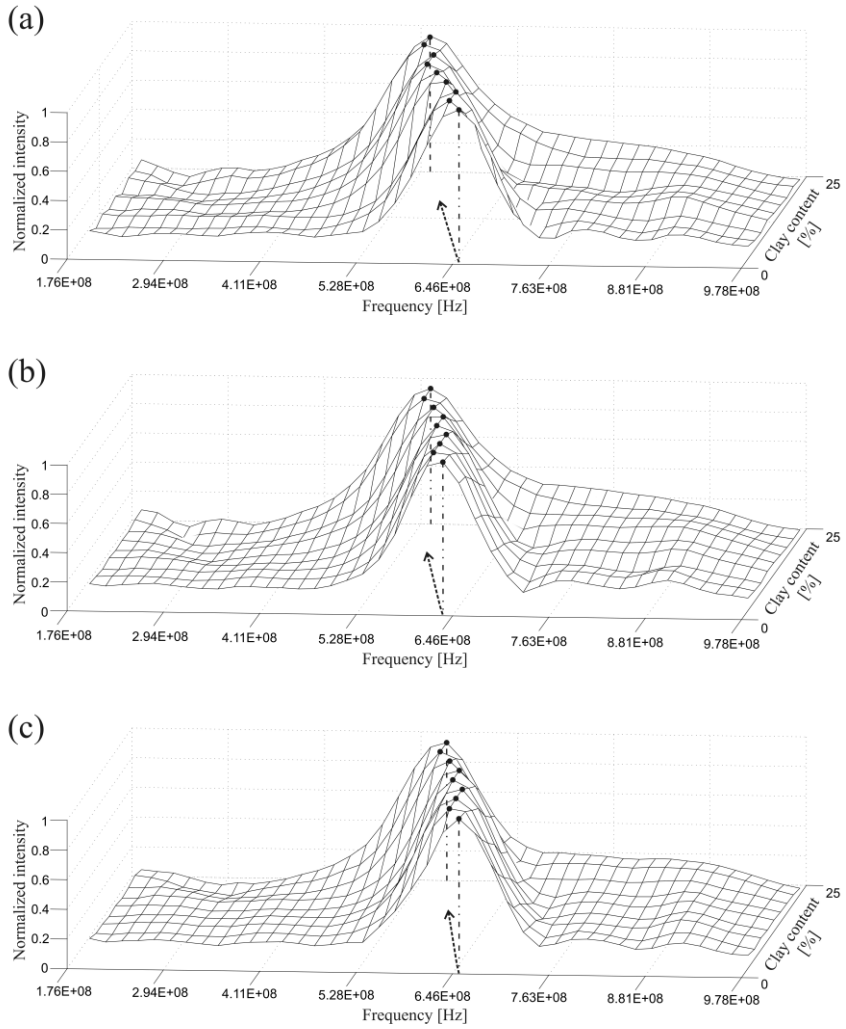

Figure 4.3: Modulation of the normalized frequency spectra with the change of clay content for A1 (a), A2 (b), and A3 (c) soil samples.

Table 4.3 lists the measured values of frequency peak, case by case. By considering the three types of soil, the highest range of frequency peaks variation Δf_P is observed in the case of material with maximum particle size. In this regard, Δf_P equals 0.97×10^8 Hz for gravel A1, and 0.78×10^8 Hz for both coarse sand A2 and fine sand A1.

Figure 4.4 shows that the value of f_P decreases as the clay intrusion increases. The mean squares fitting linear curves are characterized by high correlation coefficients R^2, greater than 0.85.

Table 4.3: Measured values of the peaks of frequency spectra (f_P) [Hz×10^8].

Soil sample identification	Clay content [%]	f_P [Hz×10^8]
A1		
Sample 1	0	6.65
Sample 2	2	6.46
Sample 3	4	6.46
Sample 4	6	6.26
Sample 5	8	6.07
Sample 6	10	5.87
Sample 7	15	5.87
Sample 8	20	5.68
Sample 9	25	5.68
A2		
Sample 10	0	6.46
Sample 11	2	6.26
Sample 12	4	6.26
Sample 13	6	6.26
Sample 14	8	6.07
Sample 15	10	6.05
Sample 16	15	5.87
Sample 17	20	5.68
Sample 18	25	5.68
A3		
Sample 19	0	6.65
Sample 20	2	6.47
Sample 21	4	6.46
Sample 22	6	6.46
Sample 23	8	6.26
Sample 24	10	6.26
Sample 25	15	6.07
Sample 26	20	5.87
Sample 27	25	5.87

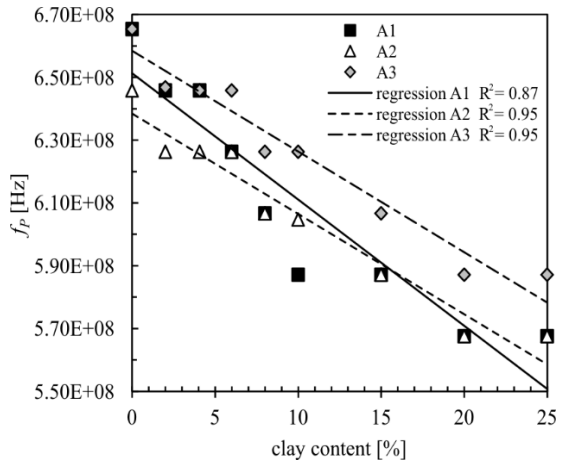

Figure 4.4: Trend of values of frequency spectra peak (f_P) for increasing rates of clay content.

The lowest fit is found for gravel A1, with a more scattered distribution of the points. Moreover, a steeper slope of the regression linear curve confirms a more remarked shift of frequency peaks in the case of coarser grade materials. The overall calibrated regression coefficients are listed in Table 4.4.

According to the main physical properties in Table 4.2 and to the values of frequency peak in Table 4.3, it can be argued that the frequency dependence of the surveyed soil samples in dry conditions is mostly related to the combination of clay rate and porosity of the mixture, whereas the measured bulk density is not consistent with the increase of clay content. In this regard, the greater porosity of gravel A1 along with the increase of clay, causes the highest measured interval Δf_P in the range 0%–15% of clay content, if compared with that observed for the other soil types. Moreover, results highlight an overall attenuation of the peak shifts for clay rates greater than 15%, which becomes zero over the 20%. This can be related to a higher concentration of clay particles within the voids of the porous material, which causes a jamming transition of charges among the contact surfaces of the aggregates, when applying the EM field. Following the research of Rozynek et al. [2012], it can be demonstrated that the mechanism of polarization in clays occurs along their silica sheets, and it is mainly due to the outer surface charges, rather than to the bulk density. Moreover, a large heterogeneity of clay particles (10 μm < d < 100 μm) contrasts their alignment with their longest axis along the EM field direction. This is sharpened at high concentrations of clay particles, wherein several particle aggregates result not able to completely re-orient with their longest axial dimension along the EM field lines, due to jamming. Therefore, a lowering of the value of the nematic order parameter is observed.

Analogously, the shift of the frequency spectrum results highly and sufficiently sensitive to lower percentages (clay [%] $\leq$ 10), and to intermediate rates (clay [%] $\leq$ 20) of clay content, respectively.

On the contrary, high clay contents (clay [%] $\geq$ 20) raise both the complexity and the concentration of clay particles system within the

Table 4.4: Values of the regression coefficients in Equation (4.3.1).

Parameter	Soil		
	A1	A2	A3
$A\times10^8$	6.51	6.38	6.58
$B\times10^6$	4.02	3.19	3.21
R^2	0.87	0.95	0.95

volumetric void fraction of the soil mixture, reducing the polarization of these particles as the EM field is applied. In such cases, the measured value of frequency peak remains constant. In fact, considering that the undisturbed gravel A1 is characterized by the highest measured porosity (e.g., Table 4.2), it is possible to consider a lower concentration of clay aggregate particles into the air voids of the mixture, thus a greater sensitivity of the dipolar ordering of clay particles to the application of an external EM field.

4.5.2 Clay content estimation from the full-waveform inversion and the time-domain signal picking techniques

4.5.2.1 Permittivity estimation using the full-waveform inversion technique

This method is applied to consider the frequency dependence of the electromagnetic parameters.

Inversions for the dielectric permittivity and the electrical conductivity were carried out for all the tested soils. For each soil samples, a constant value of dielectric permittivity and a linear behavior of conductivity are assumed to generate the impulse responses.

Inversions performed for the electrical conductivity revealed a negligible sensitivity with respect to this parameter (order of magnitude for $\sigma_{1GHz} \leq 1\times10^{-12}$ S·m^{-1}). Concerning the permittivity values, no frequency dependence was observed on the considered frequency range. Table 4.5 lists the values of relative dielectric permittivity ε_r and the corresponding normalized objective function $\varphi(\mathbf{b})$ for all the tested soils.

As it can be easily observed, results in terms of permittivity are highly consistent with the growth of clay percentage. In particular, the highest values are registered for coarse sand A2, whereas gravel A1 is characterized by the smallest relative permittivities. The overall normalized percentages of objective function range from approximately 26.5% and 55%, showing both more contained values and the lowest variability for the A1 gravel samples.

In general, it is possible to accurately evaluate the geometrical parameters by a preventive and accurate measure of the geometry of the model, such as the test box thickness, and the antenna height. A relatively large parameter space ($2 \leq \varepsilon_r \leq 6$; $-3 \leq \log\sigma_{1GHz} \leq -1$ Sm^{-1}; $-13 \leq \log\alpha \leq -1$ Sm^{-1}; $0.25 \leq h_0 \leq 0.35$ m) was used for running the inversions. The reference parameters were selected according to the expected values.

Table 4.5: Values of relative dielectric permittivity (ε_r) from laboratory measurements using the full-waveform inversion and the time-domain signal picking techniques.

Soil sample identification		Technique		
		Full-waveform inversion		Time-domain signal picking
	Clay content [%]	ε_r	φ(**b**) [%]	ε_r
A1				
Sample 1	0	2.47	35.37	2.44
Sample 2	2	2.66	50.28	2.62
Sample 3	4	2.69	30.21	2.68
Sample 4	6	2.95	39.47	2.86
Sample 5	8	3.21	26.49	3.19
Sample 6	10	3.48	33.15	3.46
Sample 7	15	3.49	36.43	3.49
Sample 8	20	3.63	31.84	3.63
Sample 9	25	3.72	31.46	3.74
A2				
Sample 10	0	2.83	54.88	2.76
Sample 11	2	2.92	53.58	2.88
Sample 12	4	3.16	41.36	3.15
Sample 13	6	3.20	38.60	3.23
Sample 14	8	3.22	49.23	3.15
Sample 15	10	3.41	41.86	3.39
Sample 16	15	3.80	28.98	3.81
Sample 17	20	3.93	33.26	3.90
Sample 18	25	3.86	29.78	3.92
A3				
Sample 19	0	2.66	52.46	2.58
Sample 20	2	2.69	43.91	2.67
Sample 21	4	2.81	53.72	2.77
Sample 22	6	2.85	48.21	2.84
Sample 23	8	3.06	44.96	3.09
Sample 24	10	3.11	46.68	3.13
Sample 25	15	3.40	48.78	3.39
Sample 26	20	3.63	47.79	3.61
Sample 27	25	3.83	38.61	3.81

The distance between the soil surface and the antenna phase center was accounted for in the data inversions. The equivalent point source of the antenna is located at approximately 0.07 m inwards from the antenna aperture. In this Subsection, the measured and modeled Green's functions are depicted in the frequency domain (Figure 4.5 (a-b)). Graphs related to these functions in time domain will be subsequently illustrated.

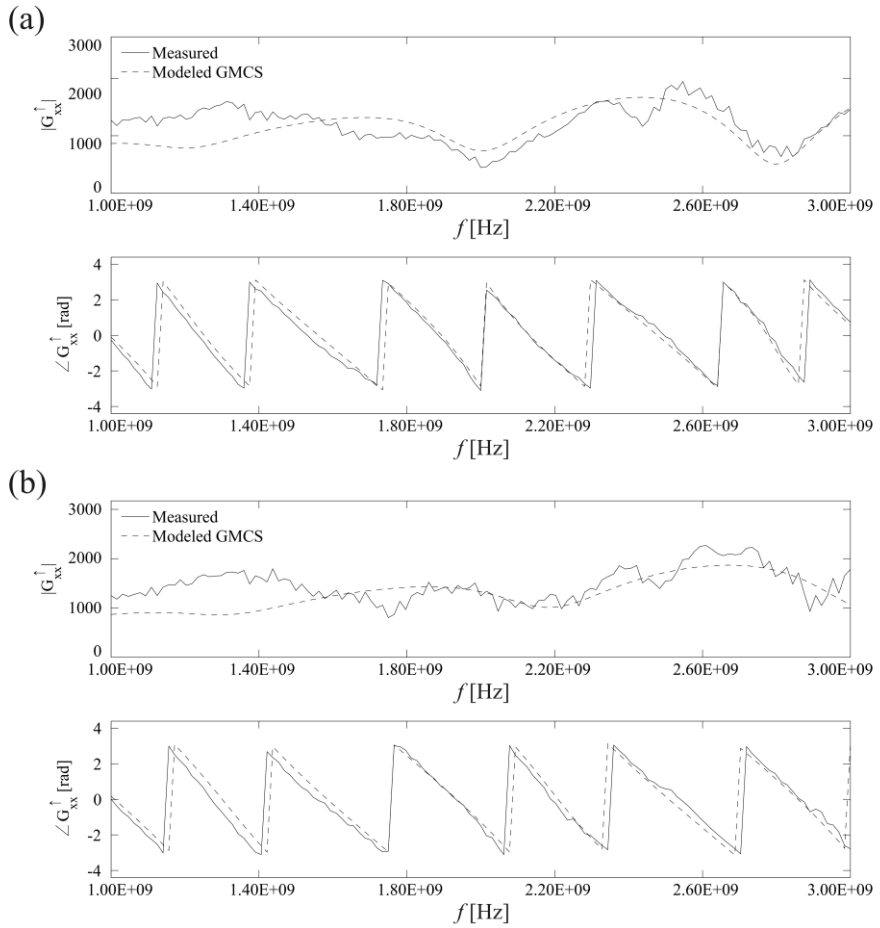

Figure 4.5: Measured and modeled Green's functions in the frequency domain (amplitude $\left|\mathbf{G}_{xx}^{\uparrow}\right|$ and phase $\angle\mathbf{G}_{xx}^{\uparrow}$) domain: (a) soil sample 13 (A2, 6% clay); (b) soil sample 20 (A3, 2% clay).

In these configurations, the propagation of EM waves can be described as simultaneous wave reflections occurring in the air layer, in the top layer, and in the bottom layer. In both cases illustrated in Figure 4.5 (a-b), it is shown a good description of the phase, except locally at lower frequencies. The overall trend of the Green's function amplitude is well reproduced by the forward model, although some discrepancies due to noise can be observed, especially in the range 1 GHz–1.6 GHz. Uncertainties can also be caused by impedance mismatches within the set-up elements, showing superimposed ripples on the measured data.

In the $\left| G_{xx}^{\uparrow} \right|$ plots, no linear behavior at higher frequencies is shown, due to a contained contrast between the air layer and the soil layer for these analysed clay contents. Amplitude in the case of soil A2 (Figure 4.5 (a)) is characterized by a higher value if compared to that observed for soil A3 (Figure 4.5 (b)). Moreover, soil A3 presents more regular and flattened oscillations.

4.5.2.2 Permittivity estimation using time-domain signal picking technique

In this Subsection, the inverse Fourier transform $g_{xx}^{\uparrow}$ of the measured and modeled responses in the frequency domain is applied. Signals can be therefore represented in the time domain (Figure 4.6 (a-b)). Therefore, in order to analyse the relative permittivity results from the application of the full-waveform inversion technique, estimates of dielectric permittivity from the measured signal are provided, following the time-domain signal picking technique.

Similarly to the case of estimates by full-waveform inversion method, a high consistency of results is shown (Table 4.5). In fact, the overall trend shows that the higher is the analysed clay content, the greater is the value of dielectric permittivity for all the tested soils.

In Figure 4.6 (a-b), two main reflections are depicted. By measuring the two-way time delay between the air/soil and the soil/air interfaces, it is therefore possible to evaluate the permittivity of the surveyed soil sample. A comparison between plots of Figures 4.6 (a) and 4.6 (b) reveals time arrivals of the main reflection peaks (air/soil interface) at 2.02 ns and 1.99 ns, respectively. The second reflection peaks occur respectively at 3.27 ns and 3.38 ns, giving a Δt = 1.25 ns for (a) and a Δt = 1.38 ns for (b). Generally, the main differences in time delay measurement are due to the second peak position, whereas the first arrival is approximately the same for all the analysed soils, as expected.

4.5.2.3 Comparison of the permittivity estimate methods

A comparison between the relative permittivity values from the full-waveform inversion and the time-domain signal picking technique (Table 4.5), indicates that the difference on the estimates performed through these two methods can reach the second decimal digit of the permittivity, with residuals less than 5%.

Nonetheless, due to the high variability of these values, the reliability of these two techniques is analysed.

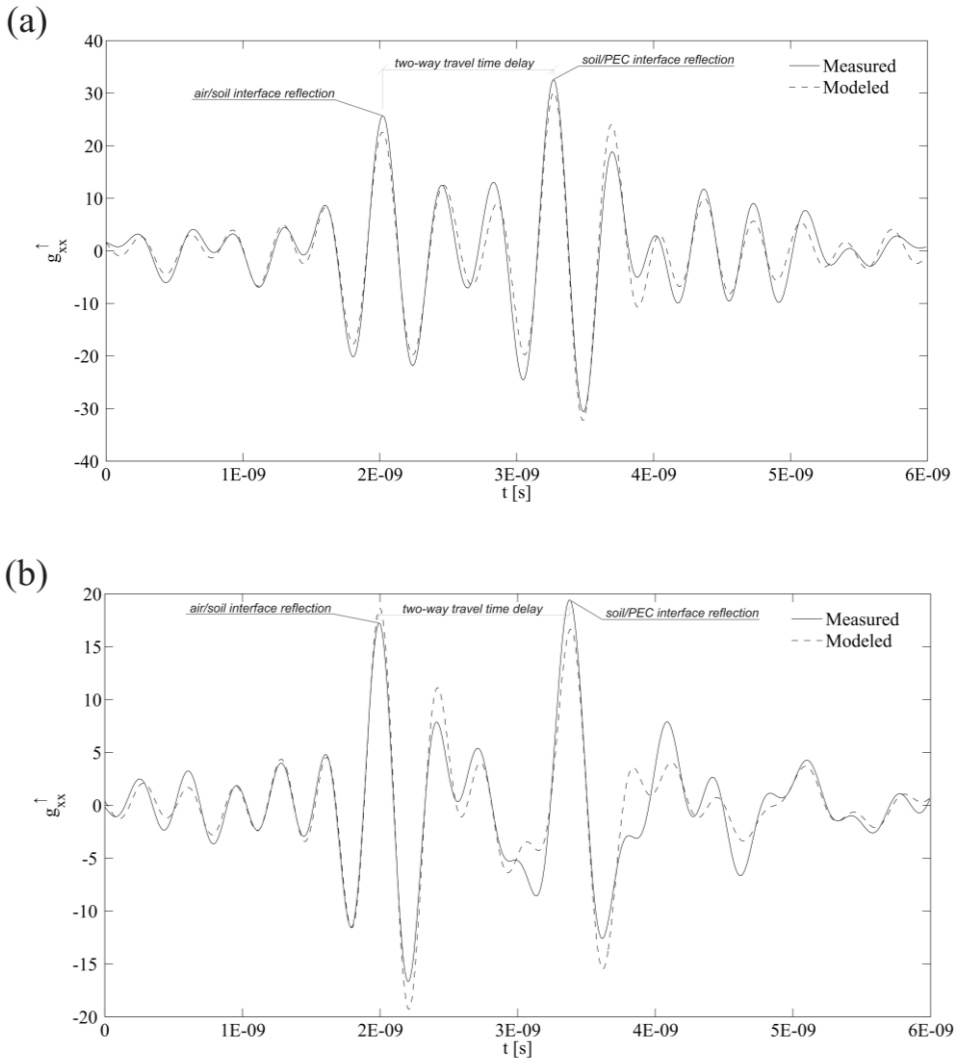

Figure 4.6: Measured and modeled Green's functions in the time $g^{\uparrow}_{xx}$ domain: (a) soil sample 5 (A1, 8% clay); (b) soil sample 17 (A2, 20% clay).

To provide a reliable comparison, the measured clay content [%] is compared to that predicted through a semi-empirical model. Basically, this model is implemented following two steps.

Firstly, fittings of the three soils specific empirical models (linear models) are performed.

Then, the general expression of a volumetric mixing formula is considered [Birchak et al., 1974].

Assuming a bi-phase configuration of the medium (i.e., dry condition of the material), the general expression is given by:

$$\text{clay} = \frac{\left[n + (1-n)\cdot \varepsilon_s^{\alpha}\right]^{\frac{1}{\alpha}} - k_2}{k_1} \tag{4.5.8}$$

where *clay* is the clay content [%], n is the normalized porosity, ε_s is the relative permittivity of the soil matrix, α is the geometric fitting parameter (assumed equal to 0.5, by literature), k_1 and k_2 are the calibrated regression coefficients (Table 4.6). In this study, Equation (4.5.8) is implemented using the porosity values in Table 4.2.

Figure 4.7 illustrates the capability of the proposed semi-empirical formula to provide estimates of clay percentage content within the range of soil textures considered in this study, using the full-waveform inversion and the time-domain signal picking technique. This formula is assumed to be valid for soils with a minimum content of clay (*clay* $\geq$ 0% by weight).

The overall distribution of the plotted points shows that the best fit is provided for low clay contents (clay $\leq$ 8% by weight), whereas greater mismatches are observed for increasing amounts of clay, wherein the regression formula mainly over-predicts the expected clay percentages. In particular, this behavior is shown to be dependent on the soil texture.

Table 4.6: Values of the regression coefficients in Equation (4.5.8) and the root-mean-square errors (RMSEs) between predicted and observed clay content.

Parameter	Technique	
	Full-waveform inversion	Time-domain signal picking
A1		
$k_1 \times 10^{-2}$	5.13	5.38
k_2	2.63	2.58
RMSE [%]	3.20	2.98
A2		
$k_1 \times 10^{-2}$	4.60	4.93
k_2	2.91	2.86
RMSE [%]	2.45	2.35
A3		
$k_1 \times 10^{-2}$	4.97	5.05
k_2	2.62	2.59
RMSE [%]	0.73	0.87

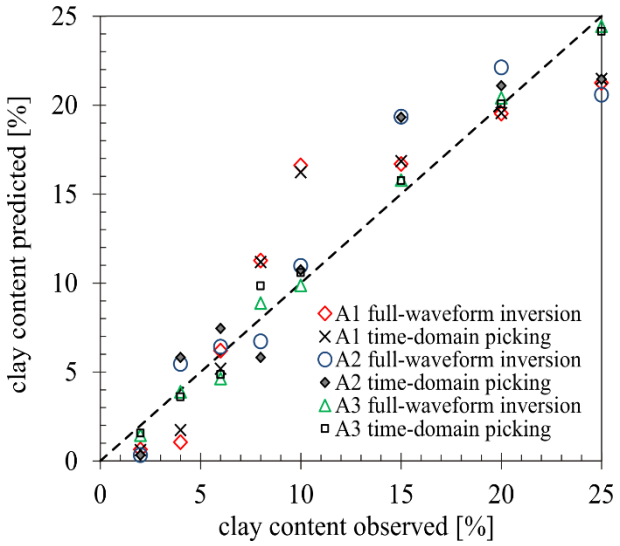

Figure 4.7: Correlation between clay content observed and predicted by fitting the permittivity estimates from the full-waveform inversion and the time-domain signal picking technique (A1, A2, and A3 soil type).

As it is listed in Table 4.6, the root-mean-square error (RMSE) is considerably higher for the A1 soil than that calculated for the A2 and A3 soils. Moreover, prediction is very accurate for the soil type with the lowest grain size. Concerning the applied techniques, the RMSE indexes show that the time-domain signal picking method yields slightly more accurate estimates of clay content in soil than those obtained through the full-waveform inversion technique.

4.6 Conclusion

In this study, GPR signal processing was carried out for the evaluation of clay content in unbound pavement layers and subgrade soils. Different GPR tools and techniques were used. Laboratory tests were carried out on different types of soil, classified as A1, A2, and A3 by AASHTO.

Firstly, results were analysed using the Rayleigh scattering technique. Considering the Fresnel theory and some recent innovative researches, it is experimentally showed the frequency dependence of clay content in heterogeneous soils. It is demonstrated that the variation of clay content affects the shift of the frequency spectra peaks. In particular, when clay content increases, the peak of the frequency spectrum shifts to lower values.

On the basis of the outcomes of laboratory tests and according to the relevant theoretical framework, an empirical approach to predict clay presence from the frequency analysis is investigated. Very promising results in terms of regression coefficients are obtained. The main benefit of this self-consistent method, is that any preventive calibration, such as core sampling, can be avoided. Nonetheless, further research, such as stochastic approaches, can be used to improve the reliability of this technique in accurately measuring the clay content.

Analogously, full-waveform inversion and time-domain signal picking techniques were used to estimate the relative dielectric permittivity of the investigated soils. Both methods show a high consistency of results. In particular, increasing rates of clay lead to increasing values of dielectric permittivity, as expected. Finally, the reliability of the outcomes from these two techniques was analysed, using a semi-empirical approach. In particular, a typical volumetric mixing formula was optimized using empirical parameters from soil specific curve fitting. Results show high reliable estimates of clay content in fine sand textured soils, as well as an overall promising prediction for all the tested soils at lower percentages of clay from both the methods. In this regard, further research is needed both for gathering larger amount of data and for best focusing on the use of more accurate predictive models.

Concerning the applicability of the used signal processing methods on real data, it is worth noting that the proper horizontal data sampling needs to be related to the scale of variation of clay content in soils. In that respect, recent GPR inspections in real road environment suggest to consider values of horizontal sampling within 0.3 m maximum.

5. Determining mechanical properties of pavement from electric parameters

5.1 Unbound pavement structures and subgrade soils

5.1.1 Introduction

Strength and deformation properties of soils and aggregates are mostly affected by inter-particle friction and cohesion, which exert outstanding effects on the bearing ratio of unbound materials in airfield and road pavements. According to Mitchell [1993], by considering that mechanical characteristics of soil depend on particles interactions and assuming that dielectric properties of materials are related to bulk density, a reasonable good correlation between dielectric and strength properties of soils would be expected.

On the basis of this idea, further research on dielectric properties and strength and deformation properties of road materials was followed since 1994 at the Texas Transportation Institute. In this regard, testing on dielectric properties of both good and problem quality Finnish and Texas aggregates were carried out [Guthrie et al., 2002; Saarenketo, 1995; Saarenketo and Scullion, 1995, 1996; Scullion and Saarenketo, 1997; Syed et al., 2000]. In particular, by the growing combined use of GPR and FWD within the same projects, observations on a certain type of reflection pattern during the summer months, were attributed to changes in the dielectric properties of the base material [Saarenketo, 1995]. According to Saarenketo [1995], the higher the dielectric value, the lower the bearing capacity of soils.

Results from the surveys have shown that the dielectric value, which is an indicator of the quality of the arrangement of water molecules around and between the aggregate mineral surfaces, and of the amount of free water or "loosely bound water" existing in materials, is a more relevant parameter of the strength and deformation properties of road aggregates than the moisture content. Moreover, a unique relation between material dielectric and moisture content must be taken into account.

More recently, researchers quantified a reference value of dielectric permittivity ($\varepsilon_r \geq 9$) as a good indicator for potential problems in the layer

[Saarenketo et al., 1998; Saarenketo and Scullion, 2000; Scullion, 2001; Scullion and Saarenketo, 2002].
The knowledge of pavement layers and subgrade soils moduli by GPR data, can provide better time-efficient measurements, mostly through the effective use of strength testing equipment, such as FWD, which can be integrated with GPR equipment and focused on surveying the most critical parts of the road. In addition, a lowering of the errors in backcalculation processing of layer moduli can be achieved.
In this regard, FWD principles can be also exploited by using its portable version, namely LFWD, mostly to favor the instrument handling in places difficult to reach. LFWD equipment is being increasingly used as an alternative in-situ device to the plate load test for the determination of the resilient modulus [Kavussi et al., 2010]. Several studies have been focused on the correlation of strength and deformation properties of load-bearing layers between standardized laboratory testing and LFWD-based in-situ measurements [George, 2000; George, 2003]. More recently, studies have been addressed to quality control surveys for testing unbound pavement structures, and subgrade soils [Alshibli et al., 2005].

5.1.2 Objective

In this Chapter, the possibility to infer mechanical characteristics of unbound compacted pavement materials and subgrade soils from their dielectric properties through GPR is investigated. Specifically, this study is aimed to provide a GPR-based approach for effective and efficient pavement management systems of Runway Safety Areas (RSAs). The proposed model was calibrated through laboratory tests conducted under controlled compaction conditions, and validated by using in-situ LFWD measurements collected on RSA unpaved soils.

5.1.3 Test devices

5.1.3.1 Ground-penetrating radar

In this work, two different GPR tools developed by IDS Ingegneria dei Sistemi S.p.A., Italy, with same electronic characteristics and different survey configurations were used for laboratory calibration (RIS 99-MF and Multi Frequency Array Radar-System) and in-situ validation (RIS 2k-MF Multi Frequency Array Radar-System) of the model. Each radar operates with two ground-coupled antennas, 600 MHz and 1600 MHz center frequencies. More details about both these radar systems are described in Appendix A, Subsections A.1.1.1 and A.1.1.2).

Data were acquired in the time domain, with a 40 ns time window and a time step $dt = 7.8125\times10^{-2}$ ns. Horizontal sampling resolution amounted to 2.4×10^{-2} m. According to the influence domain of LFWD [Benedetto et al., 2012c], only the 600 MHz mono-static channel was processed. The 1600 MHz mono-static and the remaining two bi-static channels were used for cross-checking.

5.1.3.2 Light falling weight deflectometer

The LFWD Prima 100 device manufactured by Carl Bro Pavement Consultants Kolding, Denmark, was used for the validation of the proposed model according to the relevant ASTM standards [American Society for Testing and Materials, 2007b]. It is composed of a base with loading plate, a falling mass (a 10 or 15 kg sliding hammer) and sensors with electronics and upper frame. The base contains two sensors, a load cell and a geophone, both connected to an electronic box for acquisition of deflection of the center of the plate δ_c, and data displaying. The available loading plates are circular, 100 mm, 200 mm, and 300 mm diameters. In this work, the 100 mm plate was used. This configuration provides a load pulse generated in the range 5-15 kN, within about 25-40 ms.
The dynamic deformation modulus E [MPa] is evaluated through the Boussinesq solution as follows:

$$E=\frac{k(1-\nu^2)\sigma r}{\delta_c} \tag{5.1.1}$$

where k equals 2 or $\pi/2$ for flexible and rigid plates, respectively, ν is the Poisson's ratio, δ_c is the center deflection [μm], σ is the applied stress [MPa], and r is the radius of the plate [mm].

5.1.4 Experimental framework

5.1.4.1 Laboratory materials and testing

The material used for testing is the so called "Misto della Magliana", namely a sandy alluvial heterogeneous material. Table 5.1 summarizes the main physical properties and classification of this material.
Material was tested in electrically and hydraulically isolated boxes that measure 0.36 m×0.36 m×0.12 m, so that their reference useful dimension is 0.32 m×0.32 m×0.10 m.
The GPR signal was totally reflected by a PEC at the bottom of the box (Figure 5.1).

Table 5.1: Classification of the sandy alluvial heterogeneous material used for the laboratory experiments.

Soil type	Atterberg Limits [%]		Granulometric Analysis [%]						Proctor Standard		AASHTO group
	L_L	PI	$P_{4.75}$	P_2	$P_{1.18}$	$P_{0.425}$	$P_{0.18}$	$P_{0.075}$	$\rho_{d\,max}$ [kN/m^3]	w_{opt} [%]	
Sandy soil	NP		99.9	78.7	72.5	60.5	18.8	1.6	16.50	8.05	A1

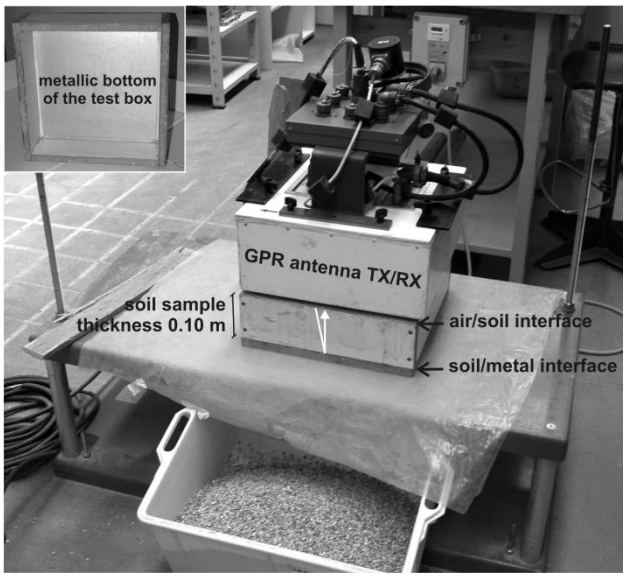

Figure 5.1: Set-up of laboratory measurements carried out using the RIS 99-MF Multi Frequency Array Radar-System.

Soil samples were gradually compacted using a vibrating table. GPR surveys were carried out for each compaction step up to the maximum density available (Table 5.2). All the samples were characterized by low amounts of water content ($w < 0.5\%$ by weight).

5.1.4.2 Survey area and in-situ soil properties

Field tests were performed at Roma-Urbe Airport in Rome, Italy. A vehicle of the Fire Department was preliminarily used to simulate runway overruns of an aircraft in the RSA. This area is defined as the surface at the lateral boundary of the runway required to reduce the risk of damage in case of landing or takeoff overruns.

GPR measurements were carried out along two trajectories of overrunning. The procedure was validated through CBR tests and twenty-nine LFWD measurements (Figure 5.2 (a-c)) were carried out every 10 m along the considered trajectory. Table 5.3 lists the main properties and the classification of the sampled soil.

Table 5.2: Bulk density values (ρ_{bulk}) of the surveyed soil samples.

Soil sample identification	ρ_{bulk} [kN/m^3]	Soil sample identification	ρ_{bulk} [kN/m^3]	Soil sample identification	ρ_{bulk} [kN/m^3]
Sample 1	16.46	Sample 8	17.68	Sample 15	17.90
Sample 2	16.46	Sample 9	17.75	Sample 16	17.94
Sample 3	17.41	Sample 10	17.77	Sample 17	17.97
Sample 4	17.52	Sample 11	17.78	Sample 18	17.98
Sample 5	17.56	Sample 12	17.84	Sample 19	18.00
Sample 6	17.59	Sample 13	17.85	Sample 20	18.07
Sample 7	17.60	Sample 14	17.89	Sample 21	18.14

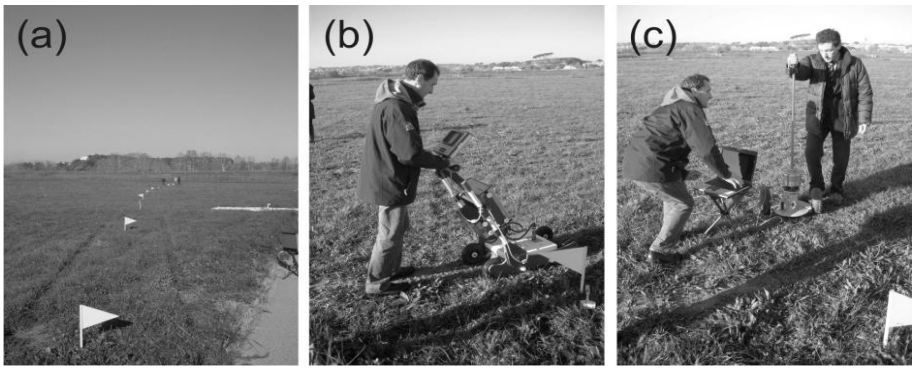

Figure 5.2: In-situ measurements at Roma Urbe Airport: (a) trajectory of overrunning; (b) RIS 2k-MF Multi Frequency Array Radar-System; (c) light falling weight deflectometer Prima 100.

Table 5.3: Classification of the RSA unpaved soil.

Soil type	Atterberg Limits [%]		Granulometric Analysis [%]						Proctor Standard		AASHTO group
	L_L	PI	$P_{4.75}$	P_2	$P_{1.18}$	$P_{0.425}$	$P_{0.18}$	$P_{0.075}$	ρ_{bulk} [kN/m^3]	w_{bulk} [%]	
Silty soil	35.7	5.1	99.9	99.4	99.2	98.2	84.8	64.9	18.20	14.90	A4

5.1.5 Theoretical background and semi-empirical model

5.1.5.1 Theoretical background

Overall, two main approaches are followed relying on, respectively, *i)* the potential dependence between dielectric and strength properties of compacted materials, and *ii)* the dependence of empirical equations for road pavement design on the bulk stress state within the pavement layer. By exploiting the common dependence of such two approaches on strength and deformation properties of unbound compacted materials and subgrade soils, a semi-empirical model is proposed.

Dielectric properties of materials were estimated according to the fundamentals of the electromagnetic theory, whose details can be found in Chapter 2, Subsection 2.1.2. As regards the processing of GPR laboratory data, permittivity estimates were carried out by measuring the two-way travel time between the two main reflections occurred, namely the air-soil and soil/PEC interfaces. By knowing the thickness of the sample, it was therefore possible to evaluate the relative dielectric permittivity, case by case.

On the contrary, validation by GPR data collected in real road environment has provided the use of surface reflection techniques for the evaluation of the relevant permittivity of the soil at each of the aforementioned twenty-nine stations. In order to provide more stable values of permittivity and according to the influence domain of LFWD [Benedetto et al., 2012c], the average of a number of traces in the range + 0.20 m and - 0.20 m from the station point, was performed.

On the other hand, empirical equations are widely used in pavement engineering for design purposes, as well as a reference for optimizing pavement conditions when planning maintenance and repair of roads through effective pavement management systems. Overall, these relationships inherently require a large number of observations in order to ascertain the relationship between input variables and outcomes. Traditionally, an important reference worldwide in case of flexible pavement design is the empirical equation provided by AASHTO [American Association of State Highway and Transportation Officials, 1993]. The expression takes into account for probabilistic and serviceability variables, as well as for geometrical indexes and mechanical properties of road layers. In particular, strength and deformation properties of pavement layers are both directly accounted for, i.e., when computing

the subgrade resilient modulus, and indirectly considered, i.e., by the use of the Structural Number (SN), being this latter expressed as follows:

$$SN=a_1 h_1+\sum_{j=2}^{n} a_j h_j m_j \quad (5.1.2)$$

where a_1 and h_1 are the layer coefficient and the layer thickness [in.] of the wearing surface layers, respectively, a_j is the j^{th} layer coefficient, h_j is the j^{th} layer thickness [in.], and m_j is the j^{th} layer drainage coefficient. The n apex indicates the number of layers underneath the intermediate course, and is usually referred to three layers [Pavement Interactive, 2008]. As regards the j^{th} layer, the relationship between the structural layer coefficient a_j and the resilient modulus E_j [psi] is given by:

$$a_j=b_j \log_{10} E_j-c_j \quad (5.1.3)$$

where b_j and c_j are empirical regression coefficients dependent on the considered layer. The value of E_j in Equation (5.1.3) is dependent on the stress state within the layer. In this regard, the relevant relationship is:

$$E_j=k_{1,j}\,\theta_j^{k_{2,j}} \quad (5.1.4)$$

where θ_j is the bulk stress [psi], $k_{1,j}$ [psi] and $k_{2,j}$ are coefficients calibrated as a function of material properties.

5.1.5.2 Prediction model

On the basis of the aforementioned empirical equations and assuming that dielectric properties are indirectly related to strength and deformation characteristics of soils, we propose herein a semi-empirical model to predict the resilient modulus of sub-asphalt layers from their relative permittivity ε_r.
The model follows the general equation:

$$E_i=\sum_{j=1}^{m} \alpha_j h_{j,i} \quad (5.1.5)$$

where E_i [MPa] is the i^{th} expected resilient modulus of the surveyed soil under the line of scan, $h_{j,i}$ [m] is the thickness of the j^{th} layer, being the subscript i referred to the i^{th} point along the longitudinal scan, and α_j is a dielectric parameter calibrated as a function of the relative permittivity.

In order to retrieve the permittivity values from the wave propagation in the medium for all the laboratory tests, the following relationship was considered:

$$h_{j,i} = v_{j,i}\Delta t_{j,i}/2 = c\Delta t_{j,i}/\left(2\sqrt{\varepsilon_{j,i}}\right) \tag{5.1.6}$$

where $\Delta t_{j,i}$ [s] is the two-way travel time between two following peaks of reflection at the j-1 and j+1 layer interfaces, which is therefore relevant for the propagation time of the GPR signal within the j^{th} layer, and $v_{j,i}$ [m/s] is the wave propagation velocity in the j^{th} medium (i.e., layer) at the i^{th} point along the longitudinal scan. Such velocity can be expressed as a function of the wave velocity in free-space c (2.99×10^8 m/s), and the unknown relative permittivity $\varepsilon_{j,i}$ of the j^{th} layer at the i^{th} point along the GPR scan. It is worth noting that, due to the single-layered configuration of test samples, the value of j is assumed to be equal to 1.
By knowing the thickness of the sample, and by measuring $\Delta t_{j,i}$, it is therefore possible to evaluate $\varepsilon_{j,i}$.
Conversely, permittivity retrieval from in-situ GPR data has been carried out by surface-reflection techniques, whose details are described in Section 3.3.1.1.
Thus, according to *i)* the structure of the medium to investigate (i.e., unpaved natural soil in RSAs), and *ii)* the influence domain of the ground-truth LFWD tool [Benedetto et al., 2012c], the following relationship was used [Maser and Scullion 1991]:

$$\varepsilon_{1,i} = \left(\frac{1 + \frac{A_{1,i}}{A_m}}{1 - \frac{A_{1,i}}{A_m}} \right)^2 \tag{5.1.7}$$

where $\varepsilon_{1,i}$ is the soil permittivity inferred as a function of the amplitude A_m of the wave reflected from a PEC, and the measured amplitude $A_{1,i}$ of the i^{th} reflection peak at the air–ground interface, which is relevant for retrieving dielectrics of layer j = 1.
Models for permittivity estimates in multi-layered sub-asphalt media, such as those used in quality control inspections of unbound sub-base laid on a subgrade soil, are thoroughly discussed in literature [Al-Qadi and Lahouar, 2004; Maser and Scullion 1991, Scullion et al., 1992].

5.1.6 Results and discussion

5.1.6.1 Model calibration

The α_j dielectric parameter was calibrated by laboratory tests. Firstly, bulk density $\rho_{j,i}$ [10^{-1} kN/m^3] and relative permittivity $\varepsilon_{j,i}$ of soil samples were related. For simplicity's sake and due to both the single-layered configuration of test samples (i.e., j = 1) and the static position of radar measurements in laboratory environment (i.e., i = 1), we will refer hereafter to the above two parameters as ρ_{bulk} and ε_r, respectively.
The least squares curve–fitting of data follows a decreasing exponential model expressed as:

$$\varepsilon_r = 1/(\beta\rho_{bulk} + \mu) \tag{5.1.8}$$

where β = -0.41, and μ = 0.86 are the relevant calibration coefficients.
Figure 5.3 illustrates the position of the measured parameters (i.e., ρ_{bulk} and ε_r) and the least squares reciprocal curve fitting of bulk density and permittivity values, as described by Equation (5.1.8). The measured values of permittivity range from 6.9 up to 8.2, thus confirming the literature reference values on subgrade soils with relatively low water contents. An overall growing trend of the relative dielectric permittivity is observed for increasing values of bulk density. According to Equation (5.1.6), the wave propagation velocity in the medium decreases, since the system becomes increasingly dissipative: the compaction of material (ε_s = 7–9) decreases the volume rate of air voids (ε_a = 1) amongst the grains of the sample, therefore the value of the relative permittivity increases, as expected.
Finally, the correlation between the α_j parameter and the relative permittivity of soil samples shows, within the surveyed density range (i.e., Table 5.2), a high consistency with the regression empirical curves used in literature to relate resilient modulus and bulk density of this type of soil [George, 2000]. Let j be the number of layers and i the number of points (traces) along the longitudinal GPR scan, the correlation can be expressed as follows:

$$\alpha_j = \pi \exp^{\tau - \omega/\varepsilon_{j,i}} \tag{5.1.9}$$

where π = 2.20, τ = 5.64, and ω = 6.55 are calibrated regression coefficients. Correlation expressed by Equation 5.1.9 between the α_j parameter and the values of permittivity $\varepsilon_{j,i} = \varepsilon_{1,i}$, assessed in laboratory environment, is shown in Figure 5.4. As mentioned, permittivity of the single-layered soil sample is expressed as ε_r.

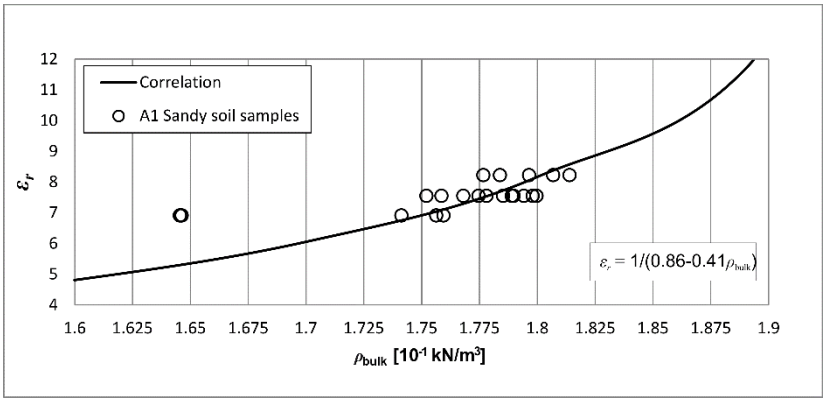

Figure 5.3: Correlation between bulk density (ρ_{bulk}) and relative dielectric permittivity (ε_r) of the surveyed soil samples.

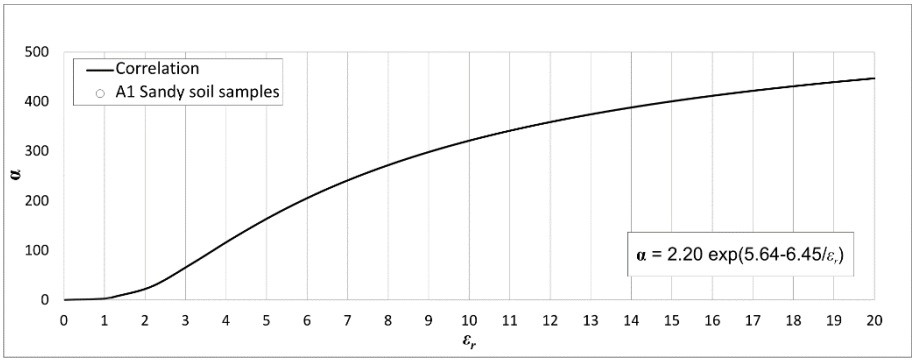

Figure 5.4: Correlation between the α parameter and the measured relative dielectric permittivity (ε_r) of the surveyed soil samples.

According to empirical relationships from literature [George, 2000], the least squares curve–fitting of data follows a decreasing exponential model. By considering a reasonable range of values accounting for the dielectric permittivity of this type of soil, α_j tending to 0 for ε_r tending to the dielectric permittivity of air ε_a, it is assumed that α_j values are lower than 450.
The trend of α_j is slightly increasing for growing values of ε_r, with negligible variations at $\varepsilon_r \geq 15$, when the maximum compaction is reasonably reached and the contribution to the value of elastic modulus decreases (e.g., Equation (5.1.9)).

5.1.6.2 Model validation

In-situ measured data of resilient modulus (E_{OBS}) from LFWD are compared to those predicted (E_{PRED}) using Equation (5.1.5) from the calibrated semi-empirical model, being $j = 1$ (Figure 5.5).

Overall, it is shown that the model underestimates the values of soil elastic modulus from LFWD, although the absolute residuals, considered as the absolute values of the difference between observed and predicted elastic moduli, are lower than 5 MPa in most of the surveyed station points.
The plot in Figure 5.6 is related to the relative incidence of residuals [%], defined by the ratio between the relative value of residual and the relevant observed elastic modulus. In this respect, relative residual is considered as the difference between observed and predicted elastic modulus. It is shown that the variability of these incidences is mostly included within approximately the 20%.

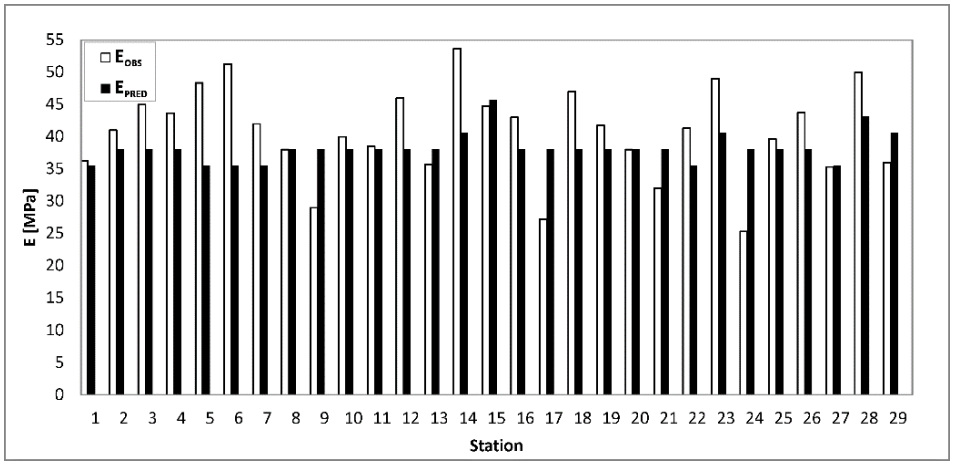

Figure 5.5: Comparison between observed (E_{OBS}) and predicted (E_{PRED}) values of elastic modulus.

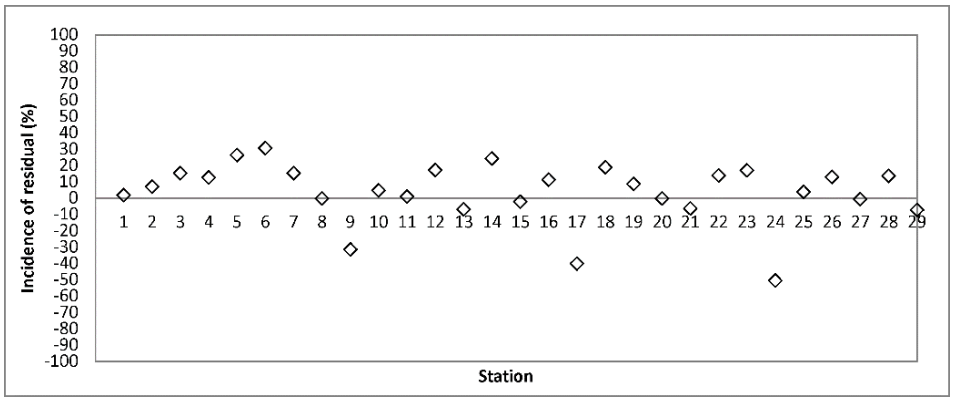

Figure 5.6: Incidence of residuals.

5.1.7 Conclusion

This study describes a GPR-based semi-empirical model for predicting strength and deformation properties of unbound compacted materials and subgrade soils from their dielectric properties.

Traditionally, mechanical characteristics of unbound pavement structures, and subgrade soils are determined through laboratory standard tests, i.e., CBR [American Society for Testing and Materials, 2009] and Proctor standard tests [American Society for Testing and Materials, 2007a], which broadly have proved to be highly reliable. Nevertheless, the significance of such analyses is very low for road engineering purposes, with respect to the long distances to be surveyed, whereby traditional techniques have also proved to be frequently not time-efficient.

On the contrary, the use of this approach relies on the possibility to include information on the bulk density of unbound materials and subgrade soils within their relative dielectric permittivity (e.g., Equation 5.1.8).

Therefore, the value of the dielectric parameter α_j (e.g., Equation 5.1.9) can be estimated as a function of the relative dielectric permittivity $\varepsilon_{j,i}$, and the layer modulus E_i of the investigated medium can be then inferred through continuous linear GPR data collection (e.g., Equation 5.1.5).

The prediction model was calibrated on the basis of the empirical equations for pavement design by using the outcomes of laboratory tests carried out on sandy soil samples, classified by AASHTO [2011] as A1, that were gradually compacted up to the maximum bulk density available. For each achieved compaction step, relative dielectric permittivity and bulk density of the soil sample were measured.

A good fit of laboratory data was shown. The model was then validated through twenty-nine in-situ measurements of soil elastic modulus, 10 meters spaced, by using LFWD. Promising results were obtained, being the absolute residuals between observed and predicted elastic moduli lower than 5 MPa in most of the surveyed station points, and the variability of residual incidences mostly included within approximately the 20%.

Prediction of strength properties of RSA unpaved soils can provide both time-efficient and cost-effective solutions, thereby improving the airport operability and favoring the decrease of runway maintenance and construction costs. As mentioned, the potential of this model can be also exploited for road purposes.

5.2 Bound pavement structures

5.2.1 Introduction

It is well-known that the loss of strength and deformation properties of road pavements and materials plays a key role in road safety issues as it brings to deep and surface damages that may cause car accidents [Tighe et al., 2000].

Overall, such event can be produced by several factors related to environmental conditions (e.g., annual precipitation, freezing index, moisture content of materials), type of material (e.g., fine or coarse grain size, subgrade soils susceptibility to frost), traffic loads, and construction aspects (e.g., pavement type, total thickness of layer structure, number of years since construction) [Haas et al., 1994; Samson and Fréchette, 1995].

Several traditional destructive techniques are used for evaluating strength and deformation properties both in laboratory and real road environment, although they can provide for time-consuming and low significant measurements.

In that respect, the use of falling weight deflectometer (FWD) has increased in the past decades [American Society for Testing and Materials, 2005; Belt et al., 2006; NCHRP, 2008], whereas more recently, the light falling weight deflectometer (LFWD) has been developed as a portable version of FWD to overcome accessibility problems of more cumbersome devices in roads under construction.

Similarly, ground-penetrating radar (GPR) is another powerful NDT increasingly used to detect the main physical properties of subsurface by transmitting and receiving electromagnetic waves in a given frequency band [Daniels, 2004; Slob, 2010].

Traditionally, such two NDTs are integrated in order to maximize the analysis capabilities of both systems [Liu and Scullion, 2006].

Starting from the first half of 1990s, the use of GPR has been focused on the possibility to infer information about mechanical properties of subgrade soils and unbound pavement structures from their dielectrics [Guthrie et al., 2002; Saarenketo, 1995; Saarenketo and Scullion, 1995, 1996; Scullion and Saarenketo, 1997; Syed et al., 2000].

In such context, new frontiers can be investigated from the use of GPR in pavement engineering, thereby representing a great opportunity to contain costs related to the use of further NDTs, and to provide more time-efficient measurements.

5.2.2 Objective

In this study, GPR was used for retrieving the Young's modulus of a flexible pavement structure in a 4m×30m test site. EM data collected by GPR were related to LFWD measurements in order to develop a prediction model. Overall, this is a contribution to the research for preventing the risk of pavement surface damages due to the loss of strength of bound materials. In addition, rehabilitation and maintenance operations can be improved through rapid and continuous GPR inspections.

5.2.3 Experimental framework

5.2.3.1 Tools and equipment

A GPR with two ground-coupled antennas, 600 MHz and 1600 MHz center frequencies (RIS 2k-MF Multi Frequency Array Radar-System, manufactured by IDS Ingegneria dei Sistemi S.p.A., Italy) was used for the EM inspections of pavement. A detailed description of this radar instrument is provided in Appendix A, Subsection A.1.1.2.

Data were acquired in the time domain, with a 40 ns time window and a time step $dt = 7.8125\times10^{-2}$ ns. Horizontal sampling resolution amounted to 2.4×10^{-2} m. According to the influence domain of LFWD [Benedetto et al., 2012c], only the 600 MHz mono-static channel was processed. The 1600 MHz mono-static and the remaining two bi-static channels were used for cross-checking.

The Prima 100 light falling weight deflectometer, developed by Carl Bro Pavement Consultants Kolding, Denmark, was used in this study. In particular, the 10kg sliding hammer and the 100mm loading plate were used for testing. Details on the operation of such tool and on the estimate of dynamic deformation modulus are described in Subsection 1.2.1 and Subsection 5.1.3.2, respectively.

5.2.3.2 Study site and survey methods

The surveyed test site is situated at the Department of Engineering of Roma Tre University in Rome, Italy (41° 51' 16.02" N, 12° 28' 06.02" E) (Figure 5.7). The surveyed area is composed of a flexible pavement structure. The average elevation is 11.5 m above the sea level, with no slope and a straight extension of the path. The test site location was selected in order to avoid surface metallic reflectors (e.g., sewer manholes) that might have provided unwanted EM reflections.

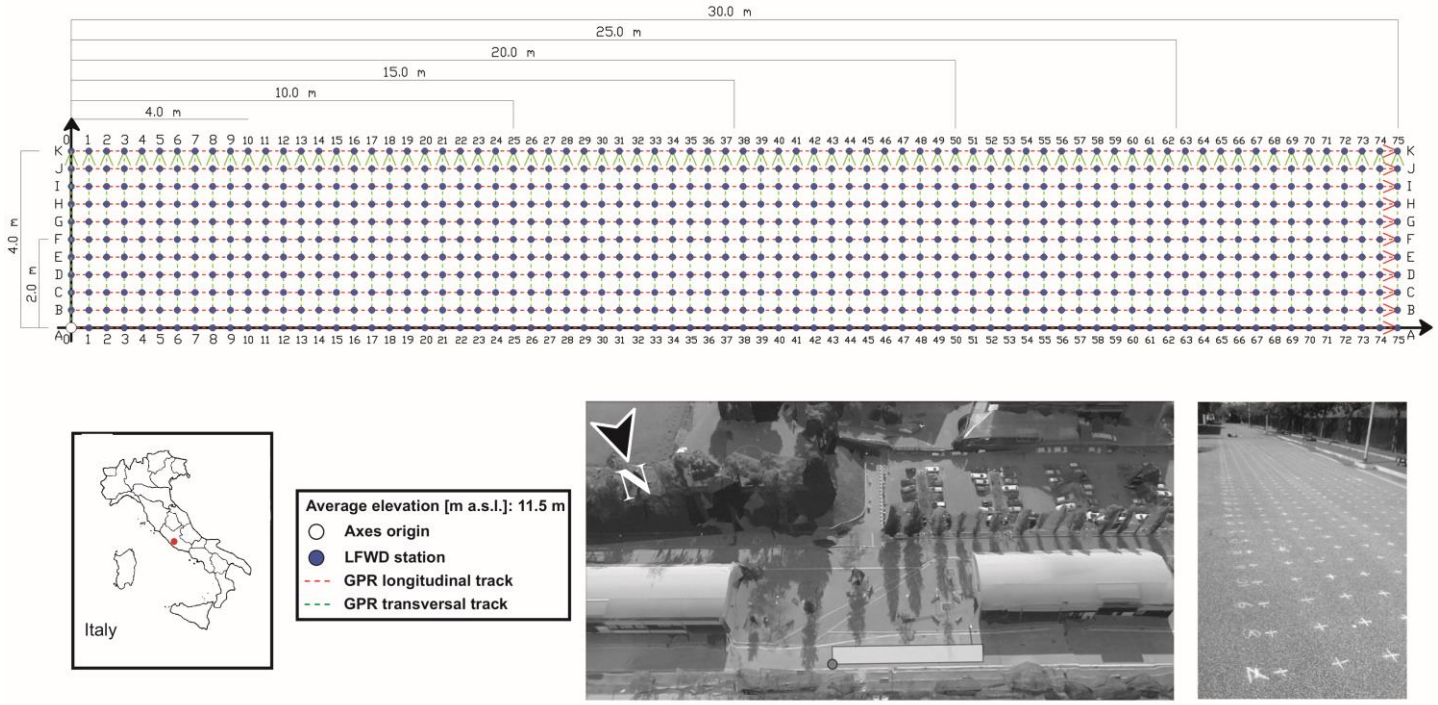

Figure 5.7: Test site for data acquisition carried out over a 4m×30m square regular grid mesh of 836 nodes.

Visual inspections of the pavement surface revealed relatively good conditions, with few early-stage cracked areas and a 62 m^2 repaved zone covering almost all of the last 12 m of the surveyed area.
The LFWD measurements took place in five days at the beginning of Autumn, on the second half of October 2013.
Overall, the points of loading were located above the 836 nodes of the 4m×30m square regular grid mesh. The instrument configuration provided the use of the 10kg hammer and the loading plate of 100 mm of diameter. According to the influence domain of such LFWD configuration [Benedetto et al., 2012c], a spacing of 0.40 m between each node was considered.
Each LFWD measure has provided for the running of 6 tests, so that more consistent *E* values could be inferred by subsequent statistical analyses. More details on the instrument testing procedures can be found in the ASTM 2583-07 standards [2007b].
The GPR data were acquired on November 8th 2013. The radar was dragged at a driving speed of about 3 km/h; 11 longitudinal tracks, 30 m long, and 76 transversal tracks, 4 m long, were acquired, thereby collecting 26415 traces in total, approximately.

5.2.4 Prediction model

The calibration of the model required a preliminary analysis of both LFWD and GPR data, mainly focused on statistical processing to increase both reliability and compatibility of electromagnetic and mechanical outputs.
Concerning the LFWD data processing, a 10% trimmed mean was applied to the six measurements carried out for each of the 836 nodes, so that the effects of outlier bias were reduced and more reliable values of observed elastic modulus (E_{OBS}) were inferred.
With regard to the GPR data, the average of a number of neighboring traces was considered for each node in order to reduce noise effects and to be more consistent with the LFWD influence domain. Mentioned traces were averaged alongside of each node with spatial lengths of + 0.20 m and - 0.20 m, and a depth zero filtering was consequently applied. A 3-D matrix was then built by considering a standard value of wave propagation velocity of the GPR signal into the medium equals to 10 cm/ns.
The model was developed by comparing the values of E_{OBS} within the investigated surface domain, and the values of amplitudes $A_{x,y,z}$ within a relevant volume of the processed 3-D matrix. It is worth mentioning that,

according to the LFWD survey configuration, such volume was defined by those amplitude values included in $z \leq 0.200$ m [Benedetto et al., 2012c].
In that regard, the value of predicted elastic modulus $E_{x,y}$ in a generic position x, y can be evaluated by Equation (5.2.10):

$$E_{x,y} = \left[\zeta\left(\iota \int_0^{z_{max}} A_{x,y,z_{[0,1]}}\, \chi_z dz\right) + \eta\right]^{-1} \qquad (5.2.10)$$

where $A_{x,y,z_{[0,1]}}$ is the value of normalized amplitude in the range [0, 1] in a generic position x, y, z; χ_z is a coefficient that takes into account the interaction between attenuation of the signal and trend of the LFWD influence domain in the depth range comprised within $z = 0$ *and* $z = z_{max}$; z_{max} is the maximum depth wherein deflections can be registered; ι is a scale coefficient from normalized to absolute values of predicted elastic modulus. Furthermore, ζ and η are amplification coefficients calibrated by minimizing errors between observed and predicted elastic modulus according to a reciprocal model regression function.

5.2.5 Results and discussion

5.2.5.1 Model calibration

In this study, calibration was carried out by sampling four x-y matrices in the range $0.000 \text{ m} \leq z \leq 0.200$ m. In particular $z_1 = 0.000$ m, $z_2 = 0.084$ m, $z_3 = 0.141$ m, and $z_4 = 0.188$ m planes were considered. Figure 5.8 (a-d) shows the normalized amplitude maps used for calibrating the model.
According to Equation (5.2.10), ζ amounts to $-9.48 \cdot 10^{-4}$, η and ι amount to 1.89 and 111.397, respectively, and χ_{z_1}, χ_{z_2}, χ_{z_3}, χ_{z_4} amount to 4.7, 3.0, 1.4, and 8.0, respectively. The final calibrated relationship can be expressed as follows:

$$E_{x,y} = \{-9.48 \cdot 10^{-4} \cdot [111.397 \cdot (4.7 \cdot A_{x,y,z1} + 3.0 \cdot A_{x,y,z2} + 1.4 \cdot A_{x,y,z3} + 8.0 \cdot A_{x,y,z4})] + 1.89\}^{-1} \qquad (5.2.11)$$

5.2.5.2 Model validation

The model was validated by taking into account E_{OBS} and $A_{x,y,z}$ values of 24 nodes of the grid, randomly selected amongst the statistical population of measured values.
Figure 5.9 shows the comparison between observed (E_{OBS}) and predicted (E_{PRED}) elastic moduli.

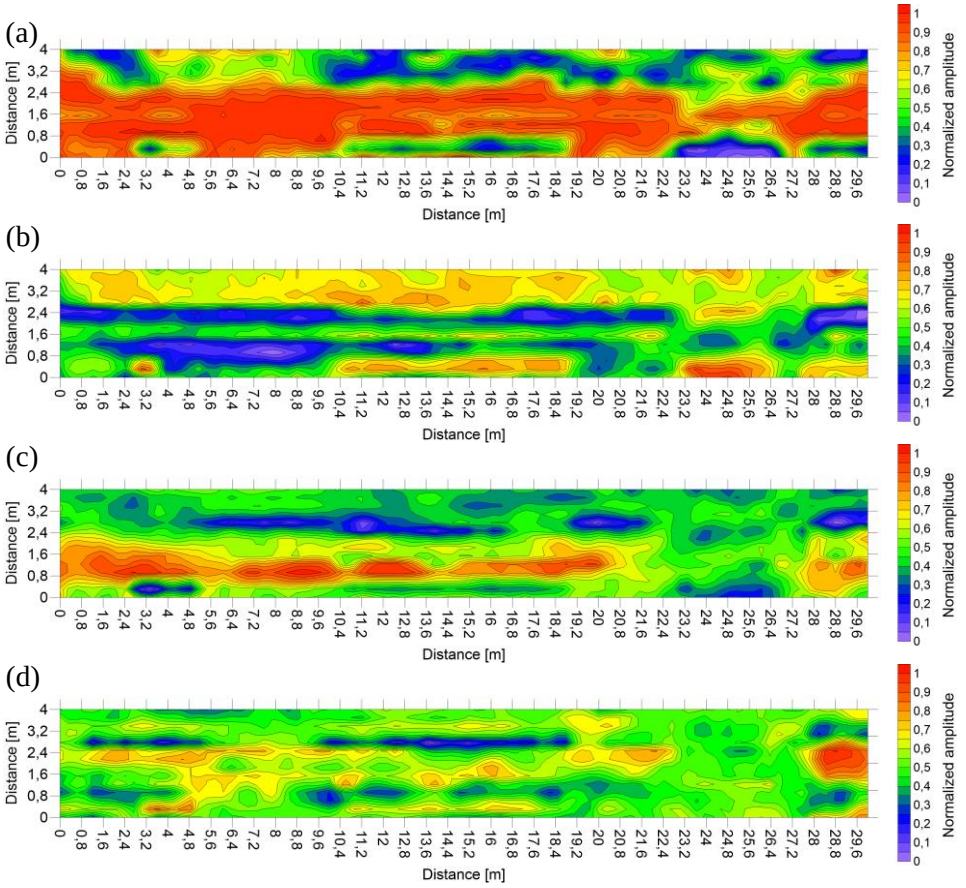

Figure 5.8: Normalized amplitude maps extracted from the 3-D matrix and used for the calibration of the prediction model: (a) z_1 = 0.000 m; (b) z_2 = 0.084 m; (c) z_3 = 0.138 m; (d) z_4 = 0.188 m.

With the exception of some few cases, a relatively good estimate of strength values is shown both for high and low values of observed elastic modulus. Furthermore, the range of interest of the predicted data seems to be consistent with that of the observed ones from LFWD. The average observed elastic modulus $E_{\overline{OBS}}$ equals to 1100.79 MPa, with a standard deviation $\sigma_{E_{\overline{OBS}}}$ of 380.86 MPa. Higher values of the same statistics are shown for the prediction model, being $E_{\overline{PRED}}$ equals to 1174.90 MPa, and $\sigma_{E_{\overline{PRED}}}$ equals to 436.65 MPa.

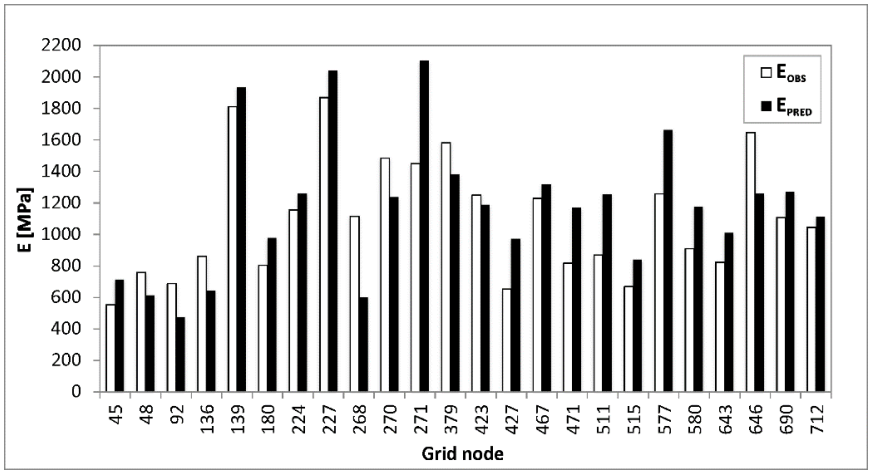

Figure 5.9: Comparison between observed (E_{OBS}) and predicted (E_{PRED}) elastic moduli for the validation of the model.

5.2.5.3 Elastic modulus mapping

Figure 5.10 presents the map of the interpolated elastic moduli from LFWD measurements.

The field-average observed elastic modulus $E_{\overline{OBS}}$ equals to 1021.71 MPa, with a standard deviation $\sigma_{E_{\overline{OBS}}}$ of 387.80 MPa. In addition, the maximum and minimum observed value of the population equals to 3178.12 MPa and 384.23 MPa, respectively. The highest grouping of strength values ranging from 2000 MPa up to 2800 MPa can be observed in four main places: x = 4.8 m, y = 2.0 m; x = 21.6÷22.8 m, y = 0.8÷1.6 m; x = 24.4 m, y = 4.0 m; x = 26.4÷29.6 m, y = 0.8÷2.0 m. Furthermore, a widespread longitudinal band of values ranging from 1300 MPa up to 1900 MPa can be found in the middle of the test site area from approximately 2.4 m < x < 17.6 m. Similarly, strength values of the same order of magnitude can be observed in the area bounded by y > 1.2 m and 18.4 m < x < 22.8 m. On the other hand, the lowest strength values are located alongside both the longitudinal edges of the surveyed area from x = 0.0 m up to x = 20.0 m, and from x = 23.6 m up to x = 30.0 m

Figure 5.11 shows the interpolated elastic modulus map as inferred from the prediction model.

The field-average predicted elastic modulus $E_{\overline{PRED}}$ equals to 1233.85 MPa, with a standard deviation $\sigma_{E_{\overline{PRED}}}$ of 435.09 MPa. The maximum and minimum predicted values of the population equal to 3006.90 MPa and 338.64 MPa, respectively.

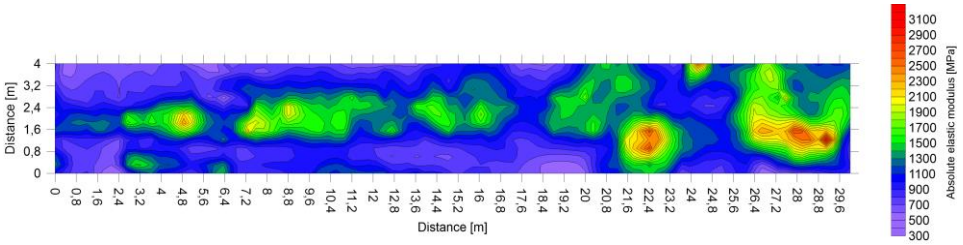

Figure 5.10: Observed elastic modulus (E_{OBS}) map from LFWD measurements.

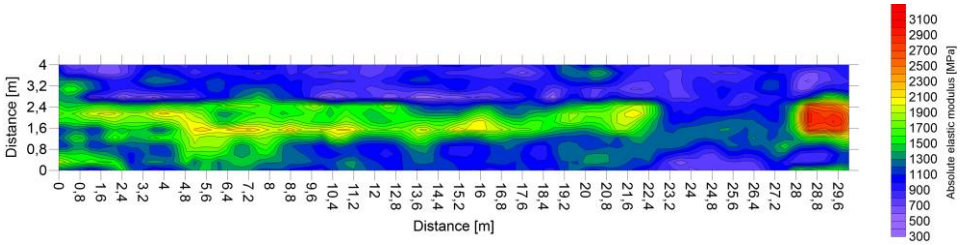

Figure 5.11: Predicted elastic modulus (E_{PRED}) map from the calibrated prediction model.

On a first sight, such statistics confirm a good accordance between observed and predicted data. Furthermore, the comparison between the two elastic modulus maps shows a relatively good agreement both in the layout and in the values of mechanical strength. A clear match can be found in the area bounded by 1.2 m < y < 2.0 m and 27.6 m < x < 29.6 m, wherein E > 2600 MPa are reached. Such highest strength values can be reasonably due to asphalt repaving works, as suggested by visual inspections of the pavement surface.

Another important match can be observed longitudinally, alongside the centerline of the test site area from x = 2.4 m up to x = 22.4 m. In this case, relatively high values of E ranging from 1300 MPa up to 1900 MPa can be reasonably related to compaction procedures under construction, that usually reveal the greatest effectiveness longitudinally, along the centerline of the pavement cross section, wherein edge effects of the roller compactors are minimum. Accordingly, promising matches can be found all along the left and right edges of the surveyed area.

5.2.6 Conclusion

This study proposes a prediction model for inferring mechanical properties of the bound pavement structure through GPR inspections in order to prevent the risk of surface damages due to the loss of strength.

In this regard, a 4m×30m test site composed of a flexible pavement structure was investigated. A square regular grid mesh, 0.40 m of side length, was built, thereby resulting in 836 nodes.

The model was calibrated by relating the observed elastic modulus from LFWD measurements, whose data were collected at each node, and the signal amplitudes from GPR traces considered within the depth of interest of the LFWD survey configuration.

The validation of the model demonstrates a relatively good agreement of both high and low strength values of observed and predicted elastic moduli. In addition, promising match is shown by comparing the two maps of elastic modulus, and a good consistency with visual surface inspections is proved. The use of 2-D tomography has shown great potential for identifying damaged areas in the top bituminous part of pavements. In this regard, promising results were found by Benedetto et al. [2012b] wherein a multi-channel high-frequency radar (see Appendix A, Subsection A.1.1.4) was used for mapping of pavement in road bridge decks.

Overall, although some mismatches are observed, results show greater perspectives of the proposed prediction model for large-scale inspections of mechanical properties of the top part of the pavement structure of roads using GPR, thereby resulting in a lowering of costs due to the use of other supporting techniques.

6. Conclusions and recommendations

The numerical and experimental results discussed in the previous Chapters are summarized here. This Chapter concludes the thesis and it gives recommendations for practical applications and usage in the field of interest.

6.1 Conclusions

Research objectives were addressed on the possibility to detect changes, by using GPR, in two relevant factors of great concern in road engineering purposes for the occurrence of damages, namely the physical and strength characteristics of road materials and subgrade soils. Accordingly, the first topic has included the analysis of *i)* water content and *ii)* clay content in subgrade soils and unbound pavement structures, while analyses of strength properties were focused on *iii)* the possibility to infer the elastic modulus of both bound and unbound pavement structures.

The first research objective consisted to validate the potential of a self-consistent method based on the analysis of the GPR signal in the frequency domain to describe the spatial variability of subsurface moisture in a natural unpaved soil. This method is of interest for a large variety of non-destructive applications. In addition, the applicability of GPR to small-scale measurements was tested. From Chapter 3 we can conclude that:

- Estimation of spatial variability of subsurface moisture through the Rayleigh scattering method matches relatively well the prediction of moisture spatial distribution from the surface reflection method. According to theoretical expectations, the peak of the frequency spectrum of the reflected signal has proved to be a comprehensive indicator, negatively related to soil moisture. In particular, a lowering of the value of the frequency spectrum peak corresponds to an increase of moisture, as the dielectric permittivity from the surface reflection method increases. On the contrary, from an increase of the value of the frequency peak, a decrease of the relative permittivity is observed.
- Subsurface moisture content at the small scale (area ≤ 0.01 m^2) can be effectively inferred by permittivity measurements through GPR and the use of a site-specific empirical petrophysical relationship

from Topp et al. [1980]. With the exception of a couple of cases, soil moisture is retrieved with a variability of residuals between probe-measured and GPR-derived data comprised within approximately the 8%.

In Chapter 4 it was discussed the capability of different GPR systems and processing techniques to provide quantitative estimation of clay content in unbound pavement layers and subgrade soils. A ground-coupled pulsed radar system was used for collecting GPR signals in time domain, whose frequency spectra were then analysed for growing amounts of clay. Furthermore, an ultra wideband SFCW radar set-up with a VNA was used for acquiring data in a bandwidth from 1 GHz to 3 GHz. Data were analysed based on full-waveform inversion and picking of GPR signals, in order to describe the material response to an applied EM field. The results of this study refer to common road materials used for construction of load-bearing layers, classified as A1, A2, and A3 by AASHTO. Tests were carried out in dry conditions and the clay range 2%–25% was investigated. The major findings are the following:

- The frequency spectra peaks of the GPR signals gathered by a ground-coupled pulsed radar system on clay-rich soils show a negative correlation with clay content. In particular, a systematic shift of the frequency peak to lower values is observed for increasing clay contents.
- The shift of the frequency spectra peaks is more sensitive to clay rate and porosity of a soil mixture than to its bulk density. In particular, the lowering of the value of frequency spectra peaks is not consistent with the trend of measured bulk density of soil samples at growing contents of clay. In this regard, the highest measured interval of variation Δf_P is observed for gravel A1 in the range 0%–15% of clay content, wherein the higher porosity of the medium along with the growing amount of clay emphasize this occurrence. Furthermore, an overall attenuation of such frequency shift for clay rates greater than 15% for all the surveyed soils is shown up to 20%, when Δf_P becomes 0.
- When an EM field is applied, a low concentration of clay within the air voids of a dry soil favors the alignment of clay particles with their longest axis along the EM field direction. With respect to the range of investigated soil texture and to the use of a ground-coupled pulsed radar, 500 MHz center frequency, this occurrence takes

place with a more or less high intensity, independently from its grain size. Thus, the Rayleigh scattering method can effectively detect variations in clay contents within 10%, rather effectively in the range 10%–20%, while few information can be retrieved by this method for clay rates greater than 20%.

- The dielectric permittivity increases in a bi-phase configuration of the soil as a function of clay content. Increases of about 1 unit of ε_r can be found amongst the undisturbed and the end-member case for all the three investigated soil types.
- Estimates of dielectric permittivity by implementing the two processing techniques on the signal measured through SFCW radars are very similar, being the differences lower than 5%.
- The proposed semi-empirical relationship for clay content prediction is appropriate for low clay amounts (clay $\leq$ 8%) within the three investigated soil types. For growing amounts of clay, the relationship mainly overestimates the expected clay percentages, independently from soil texture. In addition, the prediction is more accurate for fine-textured soils within the entire range of clay content surveyed.
- Slightly more accurate estimates of clay content can be reached through the application of the time-domain signal picking technique compared to the full-waveform inversion technique.

In Chapter 5 the problem of inferring strength and deformation properties of both bound, unbound pavement structures, and subgrade soils from their electric properties is addressed. As regards the research on unbound compacted road materials and subgrade soils (Section 5.1), a semi-empirical prediction model that exploits *i)* observations from past research on the relationship between elastic modulus and dielectric properties of soils, and *ii)* relationships on strength parameters suggested by empirical equations for the design of road pavements, was used. Concerning to the same research objective with respect to bituminous bound pavement structures (Section 5.2), a prediction model was calibrated by relating the amplitudes of the GPR signal to the relevant measured elastic modulus of the top part of a flexible pavement structure. Both methods were validated through LFWD measurements of the elastic modulus of the medium.
From Section 5.1, the following conclusions can be drawn:

- The relative dielectric permittivity increases as a function of the rate of compaction, quantified by the bulk density, of a loose sandy

alluvial material. In particular, the greater is the material compaction, the higher is its relative permittivity. Increases of about 1.3 unit of ε_r can be found amongst the minimum and maximum compacted sample.

- The proposed model matches relatively well the observed values of elastic modulus. Overall, underestimates of ground-truth data are observed, although the absolute errors are lower than 5 MPa in most of the surveyed station points. The variability of the incidences of such errors is included within the 20%.
- As regards sandy alluvial soils, A1 AASHTO group, a minimum number of twenty compaction measurements spanning the range 16.5 kN/m^3 (uncompacted loose material) – 18.2 kN/m^3 (maximally compacted loose material) is required to calibrate the model.

From Section 5.2, we can conclude that:

- The proposed model provides relatively good estimates of both high (~3300 MPa) and low (~300 MPa) observed elastic moduli. Overall, from the validation of the model on a robust number of station points, randomly selected amongst the overall nodes of the test site, overestimates of the ground-truth data are observed ($\Delta E_{\overline{PRED\text{-}OBS}}$ ~75 MPa), with a higher variability of layer moduli provided by the model ($\Delta\sigma_{E_{\overline{PRED\text{-}OBS}}}$ ~75 MPa). Statistics on the entire population of observed station points confirm such overestimate, being the difference $\Delta E_{\overline{PRED\text{-}OBS}}$ ~210 MPa; on the contrary, a slightly lower variability of layer moduli ($\Delta\sigma_{E_{\overline{PRED\text{-}OBS}}}$ ~65 MPa) is observed.
- Averages of the signal in a neighborhood of + 0.200 m and -0.200 m from the center of the station point are required when using this model. This operation has the twofold role to reduce noise effects and to make the amplitude data more consistent with the influence domain of LFWD.
- Amplitude data from a GPR trace are required to be extracted within the depth of interest of the LFWD, according to the survey configuration of the instrument. When using a LFWD configuration with a sliding hammer of 10 kg and a loading plate of 100 mm, a maximum depth of 0.200 m is provided for calibrating the model.

6.2 Recommendations

Ground-penetrating radar technology has the potential to characterize the subsurface for different non-destructive applications. In the field of pavement engineering, GPR has extensively proved its capability to provide a great contribution to road safety by preventing the risk of severe damage of pavement that may cause car accidents. In this regard, the awareness to become a national standard in continuous monitoring of road pavements is increasingly growing from countries worldwide, which aim to improve management of infrastructural asset through effective and efficient maintenance actions.

Accordingly, the development of application dedicated tools has increased over the last years, as well as the need for specific support to the design of such systems.

In that regard, this thesis is aimed to give a useful contribution to road safety issues by improving current processes of management and maintenance of road asset, along with the design of new roads, and provide effective support for the application and practical use of the tools described. Efforts have been focused on the possibility to detect and quantify those physical and strength characteristics of road materials and subgrade soils that are relevant causes of damage, such that an effective planning of supporting actions for maintenance, rehabilitation, and design of new roads may be timely performed.

In this Section, recommendations are given:

- Self-consistent frequency-based analyses of the spectrum of radar signal collected by a ground-coupled pulsed radar system, 600 MHz center frequency, are suggested for monitoring the spatial distribution of subsurface soil moisture. Furthermore and in order to quantify water content in soils at the small scale (area ≤ 0.01 m^2), the use of the surface reflection technique is suggested for retrieving soil relative dielectric permittivity to be then included within the most appropriate site-specific petrophysical empirical relationship from Topp et al. [1980].
- As regards the detection and quantification of clay content in dry load-bearing layers, both pulsed and SFCW radar systems can be used to effectively monitor materials with clay amounts lower than 8%, independently from their grain size. Frequency-based analyses of the spectrum of radar signal gathered by a common ground-coupled pulsed radar, 500 MHz center frequency, are particularly

encouraged for detecting clay in gravel-grained soil materials and, secondly, in coarse-grained materials. In such two cases, the expected potential of the instrument in detecting clay presence grows to 20% and 15%, respectively. In addition, SFCW radars can be used for accurate electric characterization of road materials which constitute load-bearing layers. By exploiting these findings and by knowledge of the main physical properties of materials, it is possible to exploit volumetric dielectric mixing formulae for retrieving the wanted quantity, e.g., clay content. In this study, the proposed semi-empirical model is particularly recommended for quantifying clay content in fine-grained materials over a wide spectrum of clay percentages, from 2% to 25%. In coarser grained materials, clay amount can be effectively estimated up to 8% by weight.

- The prediction models proposed for quantifying elastic moduli of both bound, unbound pavement structures, and subgrade soils are capable of retrieving strength and deformation properties in the range 35 MPa–45 MPa in case of unpaved natural soils, and 340 MPa–3000 MPa in case of bituminous pavement structure. Ground-coupled pulsed radar systems, having a center frequency in the neighborhood of 600 MHz, are recommended if the expected moduli are comprised within the above two ranges.
- Care must be taken when averaging GPR traces to be used as a reference signal for representing strength and deformation properties of the investigated medium. It is highly recommended to have the full knowledge of the influence domain of the instrument providing for the ground-truth measurement of elastic modulus. Accordingly, more reliable correlations can be obtained.

Bibliography

Abdi, M.R., Sadrnejad, A., Arjomand, M.A., 2009. Strength enhancement of clay by encapsulating geogrids in thin layers of sand. Geotextiles and Geomembranes 27, 447–455.

Abusharar, S.W., Han, J., 2011. Two-dimensional deep-seated slope stability analysis of embankments over stone column-improved soft clay. Engineering Geology 120, 103–110.

Al-Qadi, I.L., Haddad, R.H., Riad, S.M., 1997. Detection of chlorides in concrete using low radio frequencies. Journal of Materials in Civil Engineering 9 (1), 29–34.

Al-Qadi, I.L., Lahouar, S., 2004. Use of GPR for thickness measurement and quality control of flexible pavements. Journal of the Association of Asphalt Paving Technologists 73, 501–528.

Al-Qadi, I.L., Lahouar, S., Loulizi, A., 2002. Ground penetrating radar evaluation for flexible pavement thickness estimation. Proceedings of the Pavement Evaluation Conference 2002. pp. 1–16.

Al-Qadi, I.L., Lahouar, S., Louizi, A., Elseifi, M.A., Wilkes, J.A., 2004. Effective approach to improve pavement drainage layers. Journal of Transportation Engineering-Asce 130, 658–664.

Alani, A.M., Aboutalebi, M., Kilic, G., 2013. Applications of ground penetrating radar (GPR) in bridge deck monitoring and assessment. Journal of Applied Geophysics 97, 45–54.

Alani, A.M., Aboutalebi, M., Kilic, G., 2014. Integrated health assessment strategy using NDT for reinforced concrete bridges. NDT & E International 61, 80–94.

Alongi, T., Clemena, G.G., Cady, P.D., 1992. Condition evaluation of concrete bridges relative to reinforcement corrosion, Vol. 3, Report SHRP-S/FR-92-105, Washington, D.C.

Alshibli, K. A., Farsakh, M. A., Seyman E., 2005. Laboratory evaluation of the geogauge and light falling weight deflectometer as construction control tools. Journal of Materials in Civil Engineering, 17(5), 560–569.

American Association of State Highway and Transportation Officials (AASHTO), 1993. AASHTO Guide for Design of Pavement Structures. AASHTO, Washington, D.C.

American Association of State Highway and Transportation Officials (AASHTO), 2011. Roadside Design Guide, 4th edition. AASHTO, Washington, DC.

American Society for Testing and Materials (ASTM), 2005. Standard test method for deflections with a falling weight type impulse loading device. Annual Book of ASTM Standards 04.03, D4694.96.

American Society for Testing and Materials (ASTM), 2007a. Standard test methods for laboratory compaction characteristics of soil using standard effort. Annual Book of ASTM Standard 2007, D698-07e.

American Society for Testing and Materials (ASTM), 2007b. Standard test method for measuring deflections with a Light Weight Deflectometer (LWD). Annual Book of ASTM Standards 2007, E 2583.

American Society for Testing and Materials (ASTM), 2009. Standard test method for CBR (California bearing ratio) of soils in place. Annual Book of ASTM Standards 2009, D4429 - 09a.

Ballard, G., 1992. Under the skin. World Highways/Routes du Monde, 37–39.

Ballard, G., 1993. Non destructive assessment of pavement design & new build quality. Proceedings of Conference on Non-Destructive Testing in Civil Engineering. pp. 391–404.

Bekefi, G., Barrett, A.H., 1987. Waves in dielectrics. 6.5 in Electromagnetic Vibrations, Waves, and Radiation. MIT Press, Cambridge, MA, 426–440.

Belt, R., Morrison, T., Weaver, E., 2006. Long-term pavement performance program falling weight deflectometer maintenance manual. Report No FHWA-HRT-05-153. Georgetown Pike, VA.

Benedetto, A., 2004. Theoretical approach to electromagnetic monitoring of road pavement–applied geophysics and stochastic model. Proceedings of the Tenth International Conference on Ground Penetrating Radar, Vol. 2, pp. 623–626.

Benedetto, A., 2010. Water content evaluation in unsaturated soil using GPR signal analysis in the frequency domain. Journal of Applied Geophysics 71, 26–35.

Benedetto, A., 2013. A three dimensional approach for tracking cracks in bridges using GPR. Journal of Applied Geophysics 97, 37–44.

Benedetto, A., Benedetto, F., Tosti, F., 2012a. GPR applications for geotechnical stability of transportation infrastructures. Nondestructive Testing and Evaluation 27 (3), 253–262.

Benedetto, A., D'Amico, F., Tosti, F., 2014. Improving safety of runway overrun through the correct numerical evaluation of rutting in Cleared and Graded Areas. Safety Science, 1(62), 326–338.

Benedetto, A., Manacorda, G., Simi, A., Tosti, F., 2012b. Novel perspectives in bridges inspection using GPR. Nondestructive Testing and Evaluation 27 (3), 239–251.

Benedetto, A., Pensa, S., 2007. Indirect diagnosis of pavement structural damages using surface GPR reflection techniques. Journal of Applied Geophysics 62, 107–123.

Benedetto, A., Tosti, F., 2013. Inferring bearing ratio of unbound materials from dielectric properties using GPR: the case of Runaway Safety Areas. Proceedings of the Airfield and Highway Pavement 2013 Conference. pp. 1336–1347. doi: 10.1061/9780784413005.113.

Benedetto, A., Tosti, F., Di Domenico, L., 2012c. Elliptic model for prediction of deflections induced by a Light Falling Weight Deflectometer. Journal of Terramechanics 49 (1), 1–12.

Beroya, M.A.A., Aydin, A., Katzenbach, R., 2009. Insight into the effects of clay mineralogy on the cyclic behavior of silt–clay mixtures. Engineering Geology 106, 154–162.

Bertolini, L., Elsener, B., Pedeferri, P., Polder, R.B, 2004. Corrosion of steel in concrete. WILEY-VCH Verlag GmbH & Co. KGaA, Weinheim.

Beutel, R., Reinhardt, H.W., Grosse, C.U., Glaubitt, A., Krause, M., Maierhofer, C., Algernon, D., Wiggenhauser, H., Schickert, M., 2008. Comparative performance tests and validation of NDT methods for concrete testing. Journal of Nondestructive Evaluation 27, 59–65.

Binda, L., Lenzi, G., Saisi, A., 1998. NDE of masonry structures: use of radar tests for the characterisation of stone masonries. NDT & E International 31, 411–419.

Binda, L., Zanzi, L., Lualdi, M., Condoleo, P., 2005. The use of georadar to assess damage to a masonry Bell Tower in Cremona, Italy. NDT & E International 38, 171–179.

Birchak, J.R., Gardner, C.G., Hipp, J.E., Victor, J.M., 1974. High dielectric constant microwave probes for sensing soil moisture. Proc. IEEE 62, 93–102.

Biying, L., Qian, S., Zhimin, Z., Harming, W., 2011. A SFCWradar for through wall imaging and motion detection, in: Radar Conference (EuRAD), 2011 European, pp. 325–328.

Bohren, C.F., Huffman, D., 1983. Absorption and scattering of light by small particles. John Wiley, New York.

Brovelli, A., Cassiani, G., 2008. Effective permittivity of porous media: A critical analysis of the complex refractive index model. Geophysical Prospecting 56, 715–727.

Cardimona, S., Willeford, B., Webb, D., Hickman, S., Wenzlick, J., Anderson, N. 2003. Automated pavement analysis in Missouri using ground penetrating radar. Proceedings of the 2nd Annual Conference on the Application of Geophysical and NDT Methodologies to Transportation Facilities and Infrastructure. FHWA-WCR-02-001, pp. 1–10.

Carter, C.R., Chung, T., Masliwec, T., Manning, D.G., 1992. Analysis of Radar Reflections from Asphalt Covered Bridge Deck Structures. In: J Pilon (ed) Ground Penetrating Radar, Geological Survey of Canada Paper 90-4, 33–40.

Cassidy, N.J., 2009. Electrical and magnetic properties of rocks, soils and fluids. Chapter 5 in text book “Ground penetrating radar: Theory and applications” Ed- Harry M. Jol. Publisher Elsevier, pp. 41–72.

Chen, Y., Or, D., 2006. Geometrical factors and interfacial processes affecting complex dielectric permittivity of partially saturated porous media. Water Resources Research 42, W06423.

Chertkov, V.Y., 2005. The shrinkage geometry factor of a soil layer. Soil Science Society of America Journal 69, 1631–1683.

Chertkov, V.Y., Ravina, I., 2000. Shrinking–swelling phenomenon of clay soils attributed to capillary-crack network. Theoretical and Applied Fracture Mechanics 34, 61–71.

Curtis, J.O., 2001. Moisture effects on the dielectric properties of soils. IEEE Transactions on Geoscience and Remote Sensing 39, 125–128.

Daniels, D.J., 1996. Surface Penetrating Radar. The Inst. Electrical Eng., London.

Daniels, D.J., 2004. Ground Penetrating Radar, 2nd Edition. The Inst. Electrical Eng., London.

Davis, J.L., Annan, A.P., 2002. Ground penetrating radar to measure soil water content, in Dane, J.H. and Topp, G.C. (eds), Methods of Soil Analysis, Part 4, Soil Science Society of America (SSSA), pp. 446-463.

Dérobert, X., Berenger, B., 2010. Non-destructive evaluation of reinforced concrete structures: Non-destructive testing methods. Woodhead Publishing Series in Civil and Structural Engineering No. 35, Germany. Vol. 2. Chapter 25. pp. 574–584.

Dérobert, X., Fauchard, C., Cote, P., Le Brusc, E., Guillanton, E., Dauvignac, J.Y. Pichot, C., 2001. Stepped-Frequency Radar Applied on Thin Road Layers. Journal of Applied Geophysics 47 (3-4), 317–325.

Dérobert, X., Iaquinta, J., Klysz, G., Balayssac, J.P., 2008. Use of capacitive and GPR techniques for the non-destructive evaluation of cover concrete. NDT & E International 41, 44–52.

Dérobert, X., Simonin, J.M., Laguerre, L., 2002. Step-Frequency Radar Applied on Thin Pavement. Proceedings of the Ninth International Conference on Asphalt Pavements. pp. 1–16.

Dérobert, X., Villain, G., Cortas, R., Chazelas, J.L., 2009. EM characterization of hydraulic concretes in the GPR frequencyband using a quadratic experimental design. Proceedings of the NDT Conference on Civil Engineering, pp.177–182.

Diamanti, N., Redman, D., 2012. Field observations and numerical models of GPR response from vertical pavement cracks. Journal of Applied Geophysics 81, 106–116.

Diefenderfer, B., Galal, K., Mokarem, D., Council, V.T.R., Transportation, V.D.o., 2005. Effect of subsurface drainage on the structural capacity of

flexible pavement. Final Report No VTRC 05-R35. Virginia Transportation Research Council. Richmond, VA.

Dobson, M.C., Ulaby, F.T., Hallikainen, M.T., El-Rayes, M.A., 1985. Microwave dielectric behaviour of wet soil. Part II. Dielectric mixing models. IEEE Transactions on Geoscience and Remote Sensing 23, 35–46.

Doolittle, J.A., Rebertus, R.A., 1988. Ground-penetrating radar as means of quality control for soil surveys. Transportation Research Record 1192. pp. 103–110.

Drude, P., 1902. The theory of Optics. Longmans, Green, and Co, New York, 268–396.

Dudoignon, P., Causseque, S., Bernard, M., Hallaire, V., Pons, Y., 2007. Vertical porosity profile of a clay-rich marsh soil. Catena 70, 480–492.

du Plooy, L., 2013. The development and combination of electromagnetic and non-destructive evaluation techniques for the assessment of cover concrete condition prior to corrosion. PhD Thesis Dissertation. Université de Nantes.

Eide, E. 2002. Ultra-wideband 3d-Imaging Ground Penetrating Radar Using Synthetic Waveforms. Proceedings of 32nd European Microwave Conference, pp. 1–4.

Ékes, C., Friele, P., 2004. Ground penetrating radar and its use in forest road stability analysis. Proceedings of the Tenth International Conference on Ground Penetrating Radar, Vol. 2, 639–642.

Endres, A.L., Bertrand, E.A., 2006. A pore-size scale model for the dielectric properties of water-saturated clean rocks and soils. Geophysics 71, F185–F193.

Endres, A.L., Redmanm, J.D., 1996. Modelling the electrical properties of porous rocks and soil containing immiscible contaminants. Journal of Environmental & Engineering Geophysics 1, 105–112.

Federal Communications Commission (FCC), 2002. Title 47, Section 15 of the Code of Federal Regulations SubPart F: Ultra-wideband.

Fellner-Feldegg, H., 1969. Measurement of dielectrics in time domain. The Journal of Physical Chemistry 73, 616–623.

Fenning, P.J., McCannt, D.M., 1995. Sea defences: Geophysical and NDT investigation techniques. NDT & E International 28, 359–366.

Fiori, A., Benedetto, A., Romanelli, M., 2005. Application of the effective medium approximation for determining water contents through GPR in coarse-grained soil materials. Geophysical Research Letters 32, L09404.

Gary, W., 2003. Infrared Thermographic. CRC Press. Chapter 15. Second edition.

George, K.P., 2000. Subgrade characterization for highway pavement design. Final Report no MS-DOT-RD-00-131. University of Mississippi, Mississippi, MS.

George, K.P., 2003. Falling weight deflectometer for estimating subgrade resilient moduli. Final Report no MS-DOT-RD-03-153, University of Mississippi, Mississippi, MS.

Ghose, R., Slob, E.C., 2006. Quantitative integration of seismic and GPR reflections to derive unique estimates for water saturation and porosity in subsoil. Geophysical Research Letters 33 (5).

Gorriti, A.G., Slob, E.C., 2005. Comparison of the different reconstruction techniques of permittivity from S-parameters. IEEE Transactions on Geoscience and Remote Sensing 43, 2051–2057.

Greaves, R.J., Lesmes, D.P., Lee, J.M., Toksoz, M.N., 2005. Velocity variations and water content estimated from multi-offset, ground-penetrating radar. Geophysics 61, 638–695.

Guthrie, W.S., Sebesta, S.D., Scullion, T., 2002. Selecting optimum cement contents for stabilizing aggregate base materials, Technical Report no 7-4920-2. Texas Transportation Institute, College Station, TX.

Haas, R., Hudson, W.R., Zaniewski, J., 1994. Modern pavement management. Malabar, FL: Krieger Publishing Company.

Hallaire, V., 1987. Retrait vertical d'un sol argileux au cours du dessèchement. Mesures de l'affaissement et conséquence structurales. Agronomie 7 (8), 631–637.

Heimovaara, T.J., Bouten, W., Verstraten, J.M., 1994. Frequency domain analysis of time-domain reflectometry waveforms: 2. A four component complex dielectric mixing model for soils. Water Resources Research 30, 201–209.

Helmerich, R., Niederleithinger, E., Trela, C., Bien, J., Kaminski, T., Bernardini, G., 2012. Multi-tool inspection and numerical analysis of an

old masonry arch bridge. Structure and Infrastructure Engineering 8, 27–39.

Ho, K.C., Gader, P.D., Wilson, J.N., 2004. Improving landmine detection using frequency domain features from ground penetrating radar. Proceedings. 2004 IEEE International Geoscience and Remote Sensing Symposium, IGARSS '04, Vol. 3, pp. 1617–1620.

Hopman, V., Beuving, E., 2002. Repeatability, reproducibility and accuracy of GPR measurements. Proceedings of the 6th International Conference on the Bearing Capacity of Roads, Railways and Airfields. pp. 637–645.

Hubbard, S., Chen, J., Williams, K., Peterson J., 2005. Environmental and Agricultural Applications of GPR. Proceedings of the Tenth International Conference on Ground Penetrating Radar, pp. 45–49.

Hubbard, S., Grote, K., Rubin, Y., 2002. Mapping the volumetric soil water content of a California vineyard using high-frequency GPR ground wave data. The Leading Edge 21 (6), 552–559.

Hugenschmidt, J., Loser, R., 2008. Detection of chlorides and moisture in concrete structures with ground penetrating radar. Materials and Structures 41, 785-792.

Hugenschmidt, J., Mastrangelo, R., 2006. GPR inspection of concrete bridges. Cement and Concrete Composites 28, 384–392.

Huisman, J., Hubbard, S., Redman, J., Annan, A. Measuring soil water content with ground penetrating radar: A review. Vadose Zone Journal 2, 476-491.

Huston, D., Pelczarski, N., Esser, B., Maser, K., 2000. Damage detection in roadways with ground penetrating radar. Proceedings of the Eight International Conference on Ground Penetrating Radar. SPIE Vol. 4084: 91–94.

Huyer, W., Neumaier, A., 1999. Global optimization by multilevel coordinate search. Journal of Global Optimization 14, 331–355.

Ihamouten, A., Villain, G., Dérobert, X., 2012. Complex permittivity frequency variation from multioffset GPR data: hydraulic concrete characterization. IEEE Transactions on Instrumentation and Measurement, 61(6), 1636–1648.

Jackson, T.J., Le Vine, D.E., 1996. Mapping surface soil moisture using an aircraft-based passive microwave instrument: Algorithm and example. Journal of Hydrology 184, 85–99.

Jacobsen, O.H., Schjønning, P., 1993. A laboratory calibration of time domain reflectometry for soil water measurements including effects of bulk density and texture. Journal of Hydrology 151, 147–157.

Jol, H.M., 2009. Ground Penetrating Radar Theory and Applications. Elsevier, Amsterdam.

Jones, S.B., Friedman, S.P., 2000. Particle shape effect on the effective permittivity of anisotropic or isotropic media consisting of aligned or randomly oriented ellipsoidal particles. Water Resources Research 36, 2821–2833.

Jung, G., Jung, J., Cho, S.-M., 2004. Evaluation of Road Settlements on Soft Ground from GPR Investigations. Proceedings of the Tenth International Conference on Ground Penetrating Radar, Vol. 2, pp. 651–654.

Kavussi, A., Rafiei, K., Yasrobi, S., 2010. Evaluation of PFWD as potential quality control tool of pavement layers. Journal of Civil Engineering and Management 16(1), 123–129.

Klysz, G., Balayssac, J.-P., Laurens, S., 2004. Spectral analysis of radar surface waves for nondestructive evaluation of cover concrete. NDT & E International 37 (3), 221–227.

Knight, R., 2001. Ground penetrating radar for environmental applications. Annual Review of Earth and Planetary Sciences 29, 229–255.

Kolisoja, P., Saarenketo, T., Peltoniemi, H., Vuorimies, N., 2002. Laboratory Testing of Suction and Deformation Properties of Base Course Aggregates. Transportation Research Record 1787. Paper No. 02-3432. p. 83–89.

Koppenjan, S., 2009. Ground penetrating radar systems and design. Elsevier, Amsterdam. Chapter 3. pp. 73–97.

Kovacs, A., Morey, R.M., 1983. Detection of cavities under concrete pavement. CRREL Report No 83–18. US Army Corps of Engineers, Cold Region Research and Engineering Laboratory, Hanover, New Hampshire.

Laamrani, A., Valeria, O., Cheng, L.Z., Bergeron, Y., Camerlynck, C., 2013. The use of ground penetrating radar for remote sensing the organic layer–mineral soil interface in paludified boreal forests. Canadian Journal of Remote Sensing 39(1), 74–88.

Lahouar, S., Al-Qadi, I.L., Loulizi, A., Clark, T.M., Lee, D.T., 2002. Approach to determining in-situ dielectric constant of pavements. Transportation Research Record 1806, 81–86.

Lambot, S., Javaux, M., Hupet, F., Vanclooster, M., 2002. A global multilevel coordinate search procedure for estimating the unsaturated soil hydraulic properties. Water Resources Research 38(11), 1224, doi: 10.1029/2001WR001224.

Lambot, S., Pettinelli, E., Hubbard, S.S., Slob, E.C., 2010. Ground Penetrating Radar in hydrogeophysics. Chapter 10.4 in Subsurface Sensing Technologies.

Lambot, S., Slob, E.C., van den Bosch, I., Stockbroeckx, B., Vanclooster, M., 2004. Modeling of Ground-Penetrating Radar for accurate characterization of subsurface electric properties. IEEE Transactions on Geoscience and Remote Sensing 42, 2555–2568.

Lambot, S., Slob, E.C., Vereecken, H., 2007. Fast evaluation of zero-offset Green's function for layered media with application to ground-penetrating radar. Geophysical Research Letters 34, L21405.

Lambot, S., van den Bosch, I., Stockbroeckx, B., Druyts, P., Vanclooster, M., Slob, E.C., 2005. Frequency dependence of the soil electromagnetic properties derived from ground-penetrating radar signal inversion. Subsurface Sensing Technologies and Applications 6, 73–87.

Langman, A., Inggs, M.R., 1998. A 1-2 GHz SFCW radar for landmine detection, in: Communications and Signal Processing, 1998. COMSIG '98. Proceedings of the 1998 South African Symposium on, pp. 453–454.

Laurens, S., Balayssac, J.-P., Rhazi, J., Arliguie, G., 2002. Influence of concrete moisture upon radar waveform. RILEM Materials and Structures 35 (248), 198–203.

Laurens, S., Balayssac, J.P., Rhazi, J., Klysz, G., Arliguie, G., 2005. Non-destructive evaluation of concrete moisture by GPR: Experimental study and direct modeling. Materials and Structures 38 (283), 827–832.

Laurens, S., Rhazi, J., Balayssac, J.-P., Arliguie, G., 2000. Assessment of corrosion in reinforced concrete by Ground Penetrating Radar and half-cell potential tests. RILEM Workshop on Life Prediction and Aging Management of Concrete Structures.

Lichtenecker, K., Rother, K., 1931. Die herleitung des logarithmischen mischungsgesetzes aus allgemeinen prinzipien der stätionaren strömung. Physik Z. 32, 255–260.

Liu, W., Scullion, T., 2006. PAVECHECK: integrating deflection and ground penetrating radar data for pavement evaluation. Technical Report no 0-4495-1. Texas Transportation Institute, College Station, TX.

Loizos, A., Plati, C., 2007a. Accuracy of Ground Penetrating Radar horn-antenna technique for sensing pavement subsurface. IEEE Sensors Journal 7, 842–850.

Loizos, A., Plati, C., 2007b. Accuracy of pavement thicknesses estimation using different ground penetrating radar analysis approaches. NDT & E International 40 (2), 147–157.

Loizos, A., Plati, C., 2011. Assessment of HMA air-voids and stiffness based on material dielectric values. Road Materials and Pavement Design 12 (1), pp. 217–226.

Lunt, I.A., Hubbard, S., Rubin, Y., 2005. Soil moisture content estimation using ground-penetrating radar reflection data. Journal of Hydrology 307, 254–269.

Maierhofer, C., 2010. Planning a non-destructive test programme for reinforced concrete structures. Woodhead Publishing Limited. Vol. 2. Chapter 1. pp. 3–13.

Maierhofer, K., Kind, T., 2002. Application of impulse radar for non-destructive investigation of concrete structures. Proceedings of the Ninth International Conference on Ground Penetrating Radar. SPIE, Vol. 4758, pp. 382–387.

Malicki, M.A., R., Plagge, C.H., Roth, 1996. Improving the calibration of dielectric TDR soil moisture determination taking into account the solid soil. European Journal of Soil Science 47, 357–366.

Manning, D.G., Holt, F.B., 1983. Detecting deterioration in asphalt covered bridge decks. Transportation Research Record 899, pp. 10–19.

Maser, K.R., 1994. Highway speed radar for pavement thickness evaluation. Proceedings of the Fifth International Conference on Ground Penetrating Radar, Vol. 2, pp. 423–432.

Maser, K., 2002a. Non-destructive measurement of layer thickness of newly constructed asphalt pavement. Proceedings of the Pavement Evaluation 2002 Conference, pp. 1–24.

Maser, K., 2002b. Use of ground penetrating radar data for rehabilitation of composite pavements on high-volume roads. Transportation Research Record 1808, pp. 122–126.

Maxwell, J.C., 1865. A dynamical theory of the electromagnetic field. Philosophical Transactions of the Royal Society of London 155, 459–512.

Mie, G., 1908. Beiträge zur Optik trüber Medien, speziell kolloidaler Metallösungen. Annalen der Physik 330, 377.

Millard, S.G., Bungey, J.H., Shaw, M.R., 1993. The assessment of concrete quality using pulsed radar. Proceeding of the Non-Destructive Testing in Civil Engineering, Vol. 1, pp. 161–186.

Minet, J., Patriarca, C., Slob, E., Vanclooster, M., Lambot, S., 2010. Characterization of layered media using full-waveform inversion of proximal GPR data. Proceedings of the 2010 International Symposium on Electromagnetic Theory (EMTS 2010), pp. 1104–1107.

Minet, J., Wahyudi, A., Bogaert, P., Vanclooster, M., Lambot, S., 2011. Mapping shallow soil moisture profiles at the field scale using full-waveform inversion of Ground Penetrating Radar data. Geoderma 161, 225–237.

Miqueleiz, L., Ramirez, F., Seco, A., Nidzam, R.M., Kinuthia, J.M., Abu Tair, A., Garcia, R., 2012. The use of stabilised Spanish clay soil for sustainable construction materials. Engineering Geology 133–134, 9–15.

Mitchell, J.K., 1993 Fundamentals of Soil Behaviour. Second Edition. John Wiley & Sons, New York. 437 pp.

Montemor, M.F., Simoes, A.M.P., Ferreira, M.G.S., 2003. Chloride-induced corrosion on reinforcing steel: from the fundamentals to the monitoring techniques. Cement and Concrete Composites 25, 491–502.

Morey, R., 1998. Ground penetrating radar for evaluating subsurface conditions for transportation facilities. Synthesis of Highway Practice 255,

National Cooperative Highway Research Program, Transportation Research Board. National Academy Press.

Muller, W., 2012. Quantitative moisture measurement of road pavements using 3D noise-modulated GPR. Proceedings of the Fourteenth International Conference on Ground Penetrating Radar, IEEE Xplore Publisher, 517–523.

Nadler, A., Dasberg, S., Lapid, I., 1991. Time domain reflectometry measurements of water content and electrical conductivity of layered soil columns. Soil Science Society of America Journal 55, 938–943.

Narayana, P.A., Ophir, J., 1983. On the frequency dependence of attenuation in normal and fatty liver. IEEE Transactions on sonics and ultrasonics SU30 6, 379–383.

National Cooperative Highway Research Program (NCHRP), 2008. Falling weight deflectometer usage, National Cooperative Highway Research Program, Synthesis 381, Transportation Research Board, Washington D.C., USA.

Neville, A.M., 2011. Properties of Concrete. Pearson Education Ltd., Harlow, 5th edition.

Neville, A.M., Brooks, J.J., 2010. Concrete Technology. Pearson Education Ltd., Harlow, 2nd edition.

Nicolaescu, I., Van Genderen, P., 2008. Procedures to improve the performances of a SFCW radar used for landmine detection. Microwaves, Radar and Remote Sensing Symposium (MRRS 2008), pp. 250–255.

Norris, A.N., Callegari, A.J., Sheng, P., 1985. A generalized differential effective medium theory. Journal of the Mechanics and Physics of Solids 33, 525–543.

Odeh, I.O.A., McBratney, A.B., 2000. Using AVHRR images for spatial prediction of clay content in the lower Namoi Valley of eastern Australia. Geoderma 97, 237–254.

Oden, C.P., Olhoeft, G.R., Wright, D.L., Powers, M.H., 2008. Measuring the electrical properties of soil using a calibrated ground-coupled GPR system. Vadose Zone Journal 7 (1), 171–183.

Pakbaz, M.S., Alipour, R., 2012. Influence of cement addition on the geotechnical properties of an Iranian clay. Applied Clay Science 67–68, 1–4.

Patriarca, C., 2013. Electric characterization of construction materials through radar data inversion. PhD Thesis Dissertation. Published and printed in The Netherlands by Wohrmann Print Service. ISBN 978-94-6203-394-8.

Patriarca, C., Lambot, S., Mahmoudzadeh, M.R., Minet, J., Slob, E.C., 2011. Reconstruction of sub-wavelength fractures and physical properties of masonry media using fullwaveform inversion of proximal penetrating radar. Journal of Applied Geophysics 74, 26–37.

Patriarca, C., Tosti, F., Velds, C., Benedetto, A., Lambot, S., Slob, E.C., 2013. Frequency dependent electric properties of homogeneous multi-phase lossy media in the ground-penetrating radar frequency range. Journal of Applied Geophysics. 1(97), 81–88.

Pavement Interactive, 2008. 1993 AASHTO Flexible Pavement Structural Design. <http://www.pavementinteractive.org/article/1993-aashto-flexible-pavement-structural-design/> (Sept. 8, 2012).

Pettinelli, E., Burghignoli, P. Pisani, A.R., Ticconi, F., 2007a. Electromagnetic propagation of GPR signals in Martian subsurface scenarios including material losses and scattering. Geoscience and Remote Sensing 45 (5), 1271–1281.

Pettinelli, E., Vannaroni, G., Di Pasquo, B., Mattei, E., Di Matteo, A., De Santis, A., Annan, P.A., 2007b. Correlation between near-surface electromagnetic soil parameters and early time GPR signals: an experimental study. Geophysics 72 (2), A25–A28.

Plati, C., Loizos, A., 2012. Using ground-penetrating radar for assessing the structural needs of asphalt pavements. Nondestructive Testing and Evaluation 27 (3), 273–284.

Plati, C. Loizos, A., 2013. Estimation of in-situ density and moisture content in HMA pavements based on GPR trace reflection amplitude using different frequencies. Journal of Applied Geophysics 97, 3–10.

Pourbaix, M., 1974. Atlas of electrochemical equilibria in aqueous solutions. National Association of Corrosion Engineers, Houston, Texas.

Ranalli, D., Scozzafava, M., Tallini, M., 2004. Ground penetrating radar investigations for the restoration of historic buildings: the case study of the Collemaggio Basilica (L'Aquila, Italy). Journal of Cultural Heritage 5, 91–99.

Redman, J.D., Davis, J.L., Galagedara, L.W., Parkin, G.W., 2002. Field studies of GPR air-launched surface reflectivity measurements of soil water content. Proceedings of the Ninth International Conference on Ground-Penetrating Radar. SPIE 4758, pp. 156–161.

Reppert, P.M., Morgan, F.D., Tosoz, M.N., 2000. Dielectric constant determination using ground-penetrating radar reflection coefficient. Journal of Applied Geophysics 43, 189–197.

Richard, G., Cousin, I., Sillon, J.F., Bruand, A., Guérif, J., 2001. Effect of compaction on the porosity of a silty soil: influence on unsaturated hydraulic properties. European Journal of Soil Science 52, 49–58.

Ritsema, C.J., Dekker, L.W., 1998. Three-dimensional patterns of moisture, water repellency, bromide and pH in a sandy soil. Journal of Contaminant Hydrology 31, 295–313.

Robert, A., 1998. Dielectric permittivity of concrete between 50 MHz and 1GHz and GPR measurements for building materials evaluation. Journal of Applied Geophysics 40 (1–3), 89–94.

Roberts, R.L., Daniels, J.J., 1997. Modeling near-field GPR in three dimensions using the FDTD method. Geophysics 62 (4), 1114–1126.

Robinson, D.A., Binley, A., Crook, N., Day-Lewis, F.D., Ferre, T.P.A., Grauch, V.J.S., Knight, R., Knoll, M., Lakshmi, V., Miller, R., Nyquist, J., Pellerin, L., Singha, K. Slater, L., 2008a. Advancing process-based watershed hydrological research using near-surface geophysics: a vision for, and review of, electrical and magnetic geophysical methods. Hydrological Processes 22 (18), 3604–3635.

Robinson, D.A., Campbell, C.S., Hopmans, J.W., Hornbuckle, B.K., Jones, S.B., Knight, R., Ogden, F., Selker, J. Wendroth, O., 2008b. Soil moisture measurement for ecological and hydrological watershed-scale observatories: a review. Vadose Zone Journal 7 (1), 58–389.

Robinson, D.A., Phillips, C.P., 2001. Crust development in relation to vegetation and agricultural practice on erosion susceptible, dispersive clay soils from central and southern Italy. Soil and Tillage Research 60, 1–9.

Roth, K., Schulin, R., Fluhler, H., Attinger, W., 1990. Calibration of time domain reflectometry for water content measurement using composite dielectric approach. Water Resources Research 26, 2267–2273.

Rozynek, Z., Mauroy, H., Castberg, R.C., Knudsen, K.D., Fossum, J.O., 2012. Dipolar ordering of clay particles in various carrier fluids. Revista Cubana de Física 29, 1E37.

Saarenketo, T., 1995. Using electrical methods to classify the strength properties of Texas and Finnish base course aggregates. Center for Aggregates Research, 3rd Annual Symposium Proceedings, Austin, TX, pp. 1–19.

Saarenketo, T., 1996. Electrical properties of water in soils. Proceedings of the Sixth International Conference on Ground Penetrating Radar. pp. 129–134.

Saarenketo, T., 1998. Electrical Properties of Water in Clay and Silty Soils. Journal of Applied Geophysics 40(1–3), 73–88.

Saarenketo, T., 1999. Road Analysis, an Advanced Integrated Survey Method for Road Condition Evaluation. Proceedings of the COST Workshop on "Modelling and Advanced testing for Unbound and Granular materials". pp. 125–133.

Saarenketo, T., 2009. NDT Transportation. Chapter 13 in text book “Ground Penetrating Radar: Theory and Applications” Ed- Harry M. Jol. Publisher Elsevier, 524 p.

Saarenketo, T., Hietala, K., Salmi, T., 1992. GPR applications in geotechnical investigations of peat for road survey purposes. Geological Survey of Finland, Special Paper 16, pp. 293–305.

Saarenketo, T., Scullion, T. 1994. Ground Penetrating Radar applications on roads and highways. Research Report no 1923-2F. Texas Transportation Institute, College Station, TX. 36 pp.

Saarenketo, T., Scullion, T., 1995. Using electrical properties to classify the strength properties of base course aggregates. Research Report no 1341-2. Texas Transportation Institute, College Station, TX. 71 pp.

Saarenketo, T., Scullion, T., 1996. Laboratory and GPR tests to evaluate electrical and mechanical properties of Texas and Finnish base course aggregates. Proceedings of the Sixth International Conference on Ground Penetrating Radar. pp. 477–482.

Saarenketo, T., Scullion, T., 2000. Road Evaluation with Ground Penetrating Radar. Journal of Applied Geophysics 43, 119–138.

Saarenketo, T., Soderqvist, M.K., 1994. Ground-penetrating radar applications for bridge deck evaluations in finland. Insight 36, 496–501.

Samson, M., Fréchette, L., 1995. Seasonal variation of pavement strength based on Benkelman Beam rebounds. Canadian Strategic Highway Research Program (C-SHRP).

Sbartaï, Z.M., Laurens, S., Balayssac, J.-P., Arliguie, G., Ballivy, G., 2006a. Ability of the direct-wave of radar ground-coupled antenna for NDT of concrete structures. NDT &E International 39 (5), 400–407.

Sbartaï, Z.M., Laurens, S., Balayssac, J.-P., Ballivy, G., Arliguie, G., 2006b. Effect of concrete moisture on radar signal amplitude. ACI Materials Journal 103, 419–426.

Sbartaï, Z.M., Laurens, S., Rhazi, J., Balayssac, J.-P., Arliguie, G., 2007. Using radar direct-wave for concrete condition assessment: Correlation with electrical resistivity. Journal of Applied Geophysics 62, 361–374.

Sbartaï, Z.M., Laurens, S., Breysse D., 2009. Concrete moisture assessment using radar NDT technique–comparison between time and frequency domain analysis. Proceedings of non-destructive testing in civil engineering (NDTCE'09), 2009. pp. 1–8.

Scullion, T., 2001. Development and Implementation of the Texas Ground Penetrating Radar System. Proceeding of the 20th ARRB Conference, pp. 1–19.

Scullion, T., Lau, C.L., Chen, Y., 1992. Implementation of the Texas Ground Penetrating Radar system, Report No. FHWA/TX-92/1233-1, Texas Department of Transportation, TX.

Scullion, T., Lau, C.L., Chen, Y., 1994. Pavement evaluations using ground penetrating radar. Proceedings of the Fifth International Conference on Ground Penetrating Radar, Vol. 1, pp. 449–463.

Scullion, T., Saarenketo, T., 1997. Using suction and dielectric measurements as performance indicators for aggregate base materials. Transportation Research Record 1577, pp. 37–44.

Scullion, T., Saarenketo, T., 1998. Applications of ground penetrating radar technology for network and project level pavement management survey

systems. Proceedings of the 4th International Conference on Managing Pavements.

Sdiri, A., Higashia, T., Hattab, T., Jamoussic, F., Tasea, N., 2011. Evaluating the adsorptive capacity of montmorillonitic and calcareous clays on the removal of several heavy metals in aqueous systems. Chemical Engineering Journal 172, 37–46.

Sebesta, S., Scullion, T., 2002. Using infrared imaging and ground-penetrating radar to detect segregation in hot-mix asphalt overlays. Research Report no. 4126-1, Texas Department of Transportation, Texas A&M University, College Station, TX.

Sen, P.N., 1984. Grain shape effects on dielectric and electrical properties of rocks. Geophysics 49, 586–587.

Serbin, G., Or, D., 2003. Near-surface water content measurements using horn antenna radar: Methodology and overview. Vadose Zone Journal 2, 500–510.

Serbin, G., Or, D., 2004. Ground-penetrating radar measurement of soil water content dynamics using a suspended horn antenna. IEEE Transactions on Geoscience and Remote Sensing 42 (8), 1695–1705.

Sidney, M., 2003. Acoustic Emission. CRC Press. Doi:10.1201/9781420040050.ch16.

Slob, E., Sato, M., Olhoeft, G., 2010. Surface and borehole ground-penetrating-radar developments. Geophysics 75, A103–A120.

Soldovieri, F., Lopera, O., Lambot, S., 2011. Combination of advanced inversion techniques for an accurate target localization via GPR for demining applications. IEEE Transactions on Geoscience and Remote Sensing 49, 451–461.

Solla, M., Lorenzo, H., Riveiro, B., Rial, F.I., 2011. Non-destructive methodologies in the assessment of the masonry arch bridge of Traba, Spain. Engineering Failure Analysis 18, 828–835.

Soutsos, M.N., Bungey, J.H., Miljard, S.G., Shaw, M.R., Patterson, A., 2001. Dielectric properties of concrete and their influence on radar testing. NDT & E International 34 (6), 419–425.

Stangl, R., Buchan, G.D., Loiskandl, W., 2009. Field use and calibration of a TDR based probe for monitoring water content in a high-clay landslide soil in Austria. Geoderma 150, 23–31.

Steelman, C.M., Endres, A.L., 2011. Comparison of petrophysical relationships for soil moisture estimation using GPR ground waves. Vadose Zone Journal 10, 70–285.

Stryk, J., Matula, R., Pospisil, K., 2013. Possibilities of ground penetrating radar usage within acceptance tests of rigid pavements. Journal of Applied Geophysics. 1(97), 81–88.

Syed, I., Scullion, T., Randolph, R.B., 2000. Tube suction test for evaluating aggregate base materials in frost- and moisture-susceptible environments. Transportation Research Record 1709, pp. 78–90.

Tighe, S., Li, N.Y., Falls, L.C., Haas, R., 2000. Incorporating road safety into pavement management. 79th Annual Meeting of the Transportation-Research-Board, Transportation Research Board Nat Research Council. pp. 1–10.

Topp, G.C., Davis, J.L., Annan, A.P., 1980. Electromagnetic determination of soil water content: measurements in coaxial transmission lines. Water Resources Research 16, 574–582.

Tosti, F., Benedetto, A., 2012. Pavement pumping prediction using ground penetrating radar. Proceedings of the 5th International Congress on Sustainability of Road Infrastructures, Vol. 53, pp. 1045–1054.

Ulaby, F.T., Dubois, P.C., van Zyl, J., 1996. Radar mapping of surface soil moisture. Journal of Hydrology 184, 57–84.

Ulriksen, C.P.F., 1982. Application of impulse radar to civil engineering. Doctoral Thesis. Lund University of Technology. Department of Engineering Geology. 179 p.

Van Dam, R.L., Van Den Berg, E.H., Van Heteren, S., Kasse, C., Kenter, J.A.M., Groen, K., 2002. Influence of organic matter on radar-wave reflection: Sedimentontological implications. Journal of Sedimentary Research 72(3), 341–352.

Van de Hulst, H.C., 1981. Light Scattering by Small Particles, Ed. Dover, New York.

Vereecken, H., Huisman, J.A., Bogena, H., Vanderborght, J., Vrugt, J.A., Hopmans, J.W., 2008. On the value of soil moisture measurements in vadose zone hydrology: a review. Water Resources Research 44 (4), W00D06.

Viscarra Rossel, R.A., Cattle, S.R., Ortega, A., Fouad, Y., 2009. In situ measurements of soil colour, mineral composition and clay content by vis–NIR spectroscopy. Geoderma 150, 253–266.

Voltz, M., Cabidoche, Y.M., 1995. Non-uniform volume and water content change in swelling clay soil: I. Theoretical analysis. European Journal of Soil Science 46, 333–343.

Von Hippel, A., 1995. Dielectric materials and applications, Ed. Artech House, Boston.

Wagner, W., Blöschl, G., Pampaloni, P., Calvet, J.C., Bizzarri, B., Wigneron, J.P., Kerr, Y., 2007. Operational readiness of microwave remote sensing of soil moisture for hydrologic applications. Nordic Hydrology 38 (1), 1–20.

Weihermüller, L., Huisman, J.A., Lambot, S., Herbst, M., Vereecken, H., 2007. Mapping the spatial variation of soil water content at the field scale with different ground penetrating radar techniques. Journal of Hydrology 340 (3–4), 205–216.

Wimsatt, A., Scullion, T., Ragsdale, J., Servos, S., 1998. The use of ground penetrating radar in pavement rehabilitation strategy selection and pavement condition assessment. Transportation Research Board Paper 980129, pp. 1–21.

Wood, G.S., Osborne, J.R., Forde, M.C., 1995. Soil parameters for estimating the rolling resistance of earthmoving plant on a compacted silty cohesive soil. Journal of Terramechanics 32 (1), 27–41.

Appendix A

A.1 Pulsed radar systems

A.1.1 Ground-coupled antennas

A.1.1.1 RIS 99-MF Multi Frequency Array Radar-System– IDS Ingegneria dei Sistemi S.p.A., Italy

This radar (Figure A.1) includes two ground-coupled antennas, 600 MHz (MF) and 1600 MHz (HF) center frequencies.
Overall, four configurations can be used for gathering data, namely the two mono-static configurations (TX; RX = 600 MHz; TX; RX = 1600 MHz), and the two remaining cross polar bi-static (TX = 600; RX = 1600 MHz; TX = 1600 MHz; RX = 600 MHz).
Radar dimensions are 0.25 m × 0.36 m × 0.36 m.
Several time windows and signal sampling resolutions (samples/trace) can be set. The best combination must be set according to the type of survey and the center frequency of investigation. Within the framework of pavement engineering applications and according to the electronics of this

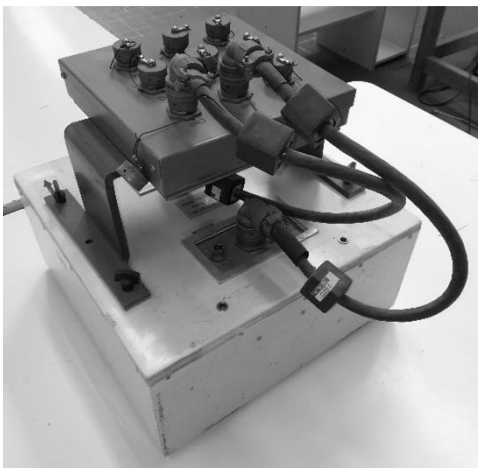

Figure A.1: RIS 99-MF Multi Frequency Array Radar-System, manufactured by IDS Ingegneria dei Sistemi S.p.A., Italy.

radar it is recommended to set a time window of 40 ns, wherein the signal is collected with a number of samples per trace amounting to 512, so that the sampling time step *dt* equals 7.8125×10^{-2} ns.
The wheel encoder indicates the position of the radar cart to the control unit within a single scan, in order to referencing information acquired. Encoder nominal resolution amounts to 2.4×10^{-2} m, which is definitely the minimum sampling resolution whereby data are collected. The maximum speed allowed for gathering data amounts to 7.9 km/h.
Further technical information about hardware and software characteristics can be found within the relevant instruction manual provided by manufacturer.

A.1.1.2 RIS 99-MF Multi Frequency Array Radar-System– IDS Ingegneria dei Sistemi S.p.A., Italy

This radar (Figure A.2) includes two ground-coupled antennas, 600 MHz (MF) and 1600 MHz (HF) center frequencies, manufactured by GSSI Geophysical Survey Systems, Inc., USA.
Overall, four configurations can be used for gathering data, namely the two mono-static configurations (TX; RX = 600 MHz; TX; RX = 1600 MHz), and the two remaining cross polar bi-static (TX = 600; RX = 1600 MHz; TX = 1600 MHz; RX = 600 MHz).

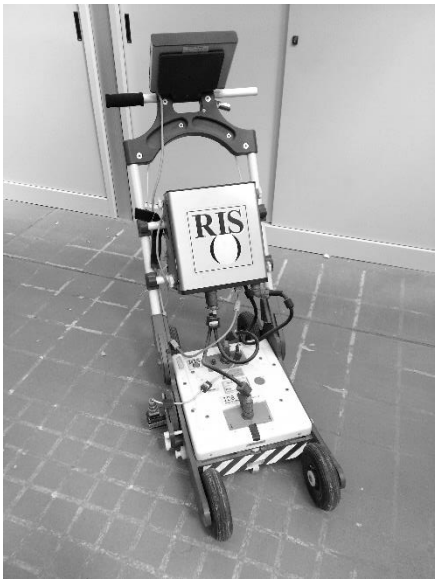

Figure A.2: RIS 2k-MF Multi Frequency Array Radar-System, manufactured by IDS Ingegneria dei Sistemi S.p.A., Italy.

Radar dimensions are 0.18 m×0.39 m×0.42 m. As regards time windows, signal sampling resolutions, and wheel encoder characteristics, they apply as described for the RIS 99-MF Multi Frequency Array Radar-System.
Further technical information about hardware and software characteristics can be found within the relevant instruction manual provided by manufacturer.

A.1.1.3 PulseEKKO PRO 500–Sensors & Software Inc., Canada

This radar (Figure A.3) is set-up in a bi-static configuration and common offset. For the research activity described in this thesis, transmitter and receiver transducers with the same center frequency of investigation of 500 MHz have been used.
Transducers units have antennas and electronics assembled into a monolithic package to optimize performance. A single transducer measures 0.20 m×0.38 m×0.38 m, and is provided with a metallic cable as a control connection and a low power warning of 10.2 V.
Power supply is 150 mA at 12 VDC for the transmitter, and 200 mA at 12 VDC for the receiver transducer. Transducer footprint measures 0.15 m×0.15 m, with a nominal spatial resolution length of 5×10^{-2} m.

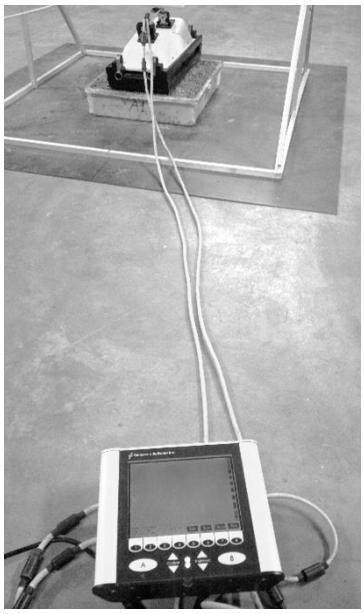

Figure A.3: PulseEKKO PRO 500, manufactured by Sensors & Software Inc., Canada.

The control module has a size of 0.172 m×0.146 m×0.037 m, and it is characterized by a pulse repetition frequency (PRF) variable to 100 kHz, a time window ranging from 1 ns to 200000 ns, and a number of samples per trace that ranges from 1 to 31000. Positioning is provided by a metric wheel and/or a GPS interface.

A.1.1.4 RIS Hi Bright–IDS Ingegneria dei Sistemi S.p.A., Italy

The equipment (Figure A.4) integrates two arrays of ground-coupled antennas, having a center frequency of 2 GHz. Such high frequency allows to reach a theoretical resolution of 1.25×10^{-2} m along vertical profile (quarter of wavelength criteria) for shallow objects. Each antenna includes transmitter, transmitting dipole, receiver, and receiving dipole. Basically, each antenna is therefore capable of emitting an electromagnetic pulse and collecting the signal reflected by buried objects.

Antennas are arranged with different polarisation. One array includes sensors with parallel polarisation with respect to the scanning direction (VV array); the other one provides sensors set in orthogonal polarisation with respect to the scanning direction (HH array). Overall, the system is capable to collect 16 profiles within a single longitudinal scan (8 HH + 8 VV). Distance between two adjacent profiles is 0.1 m, being VV and HH traces collected over the same line.

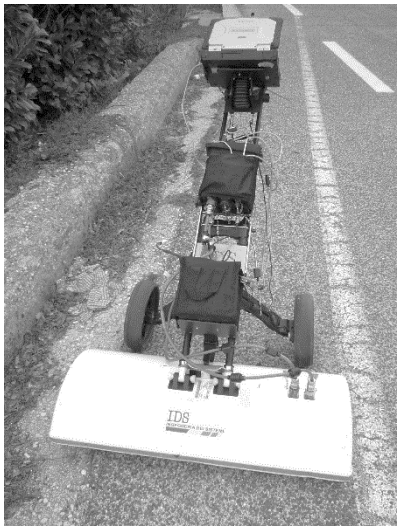

Figure A.4: RIS Hi Bright, manufactured by IDS Ingegneria dei Sistemi S.p.A., Italy.

The total scan width equals to 0.7 m. while the size of the radar on the ground is 0.98 m×0.42 m.
Two synchronised IDS DAD FastWave control units allow to collect 100 traces/m at 7 Km/h. Positioning is provided by a metric wheel and/or a GPS interface.

A.1.2 Air-coupled antennas

A.1.2.1 RIS Hi-Pave HR1 1000–IDS Ingegneria dei Sistemi S.p.A., Italy

The radar configuration (Figure A.5) provides a single air-launched antenna, 1000 MHz center frequency with one DAD K2_FW FastWave control unit.
Data density amounts to 5×10^{-2} m, if acquiring 512 samples per trace at 125 km/h. Nevertheless, acquisition is possible up to 250 km/h at 10 scans/meter and 512 samples per trace. Antenna dimensions are 0.53 m×0.23 m×0.50 m.
The control unit DAD K2_FW FastWave is capable of managing up to 8 channels, with a PRF of 400 kHz. Data are acquired with a frequency amounting to 400 kHz.
Time window can be set from 1 to 9999, with a maximum number of traces/s which amounts to 4760, when setting 128 samples/trace. The number of samples per trace can be set from 128 to 8192. Positioning is provided by a metric wheel and/or a GPS interface.
For pavement engineering applications, according to the electronics of this radar system it is recommended to set a time window of 25 ns, wherein

Figure A.5: GPR survey van mounting the air-launched antenna RIS Hi-Pave HR1 1000, manufactured by IDS Ingegneria dei Sistemi S.p.A., Italy.

signal is collected with a number of samples per trace amounting to 512, so that the sampling time step *dt* equals 4.8828×10^{-2} ns.
In addition, recommended survey configuration for pavement engineering applications provides the distance from the van body to be at least 1.20 m, and the heigth of the radar from the ground amounting to 0.40 m minimum.

A.2 SFCW radar systems

A.2.1 Vector network analyser HP 8573C–Hewlett Packard Company, USA

Within the framework of the research carried out in this thesis, an ultra wideband (UWB) stepped frequency continuous wave (SFCW) radar was set-up using a vector network analyzer (VNA), manufactured by Hewlett Packard (8753C, 300 KHz–3 GHz) (Figure A.6). The antenna used was a linear polarized double-ridged broadband TEM horn (BBHA 9120 A, manufactured by Schwarzbeck Mess-Elektronik, Germany), in a mono-static configuration.
A high quality SMA-type 50 Ω coaxial cable connected the VNA to the antenna through an SMA-N adaptor.

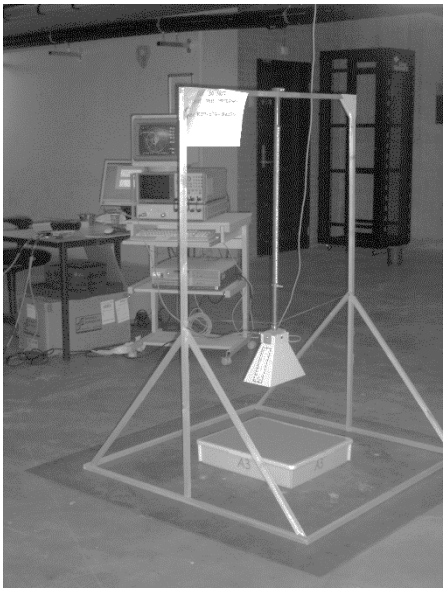

Figure A.6: SFCW radar set-up using a vector network analyzer HP 8573C (manufactured by Hewlett Packard Company, USA) and a linear polarized double-ridged broadband TEM horn BBHA 9120 A (manufactured by Schwarzbeck Mess-Elektronik, Germany), in a mono-static configuration.

Antenna dimensions are 220 mm length and the aperture area is 142 mm^2×245 mm^2; its nominal frequency range is 0.8 GHz–5 GHz, with an isotropic gain ranging from 6 dBi–14 dBi. The feasibility of far-field measurements is allowed by the small 3-dB beamwidth of the antenna.

About the author

Fabio Tosti was born in Perugia, Italy, on November 26th, 1982. After completing secondary education in 2001 at Liceo Scientifico Francesco Borromini in Rome, Italy, he obtained a BCs in Civil Engineering from Roma Tre University in Rome, Italy. He graduated *cum laude* in the 2008-2009 academic year from the same university in "Road Infrastructure and Transportation Engineering". He embarked into a PhD in the Department of Engineering at Roma Tre University in 2011. From August 2011 to November 2011 and from October 2012 to November 2012 he was a visiting PhD student in the Faculty of Civil Engineering and Geosciences at the Delft University of Technology in Delft, The Netherlands. During his post-graduate studies he served as assistant to review manager for the International Journal "Advances in Transportation Studies", and as Project Leader in Project 2.5 "Determination, by using GPR, of the volumetric water content in structures, sub-structures, foundations and soil" of COST Action TU1208 "Civil Engineering Applications of Ground Penetrating Radar". He served as co-Convener of Session GI3.1 "Civil Engineering Applications of Ground Penetrating Radar" at the EGU General Assemblies on 2013 and 2014.
Since February 2014 he is a research fellow at the Department of Engineering of Roma Tre University, Rome.

International journal publications

- Benedetto, A., D'Amico, F., Tosti, F., Improving safety of runway overrun through the correct numerical evaluation of rutting in Cleared and Graded Areas, *Safety Science*, **1**(62) (2014) 326–338.

- Tosti, F., Patriarca, C., Slob, E.C., Benedetto, A., Lambot, S., Clay content evaluation in soils through GPR signal processing, *Journal of Applied Geophysics*, **97** (2013) 69–80.

- Patriarca, C., Tosti, F., Velds, C., Benedetto, A., Lambot, S., Slob, E.C., Frequency dependent electric properties of homogeneous multi-phase lossy media in the ground-penetrating radar frequency range, *Journal of Applied Geophysics*, **1** (97) (2013), 81–88.

- Benedetto, F., Tosti, F., GPR spectral analysis for clay content evaluation by the frequency shift method, *Journal of Applied Geophysics*, **1** (97) (2013), 89–96.

- Benedetto, A., Benedetto, F., Tosti, F., GPR applications for geotechnical stability of transportation infrastructures, *Nondestructive Testing and Evaluation*, **27** (3) (2012), 253–262.

- Benedetto, A., Manacorda, G., Tosti, F., Novel perspectives in bridges inspection using GPR, *Nondestructive Testing and Evaluation*, **27** (3) (2012), 239–251.

- Benedetto, A., Tosti, F., Di Domenico, L., Elliptic model for prediction of deflections induced by a Light Falling Weight Deflectometer, *Journal of Terramechanics*, **49** (2011), 1–12.

Accepted for publication

- Benedetto, A., Tosti, F., Ortuani, B., Giudici, M., Mele, M., Mapping the spatial variation of soil moisture at the large scale using GPR for pavement applications, *Near Surface Geophysics*, ISSN: 15694445, DOI: 10.3997/NSG.

- Tosti, F., Umiliaco, A., FDTD Simulation of the GPR Signal for Preventing the Risk of Accidents due to Pavement Damages, International Journal of Interdisciplinary Telecommunications and Networking (IJITN), ISSN: 1941-8663, DOI: 10.4018/IJITN.

Conference publications

- Tosti, F., D'Amico, F., Calvi, A., and Benedetto, A., On-site inspections of pavement damages evolution using GPR, Geophysical Research Abstracts Vol. 16, EGU2014-12978, 2014 EGU General Assembly 2014.

- Benedetto, A., Tosti, F., and D'Amico, F., Investigation of mechanical properties of pavement through electromagnetic techniques, Geophysical Research Abstracts Vol. 16, EGU2014-13218, 2014 EGU General Assembly 2014.

- Pajewski, L., Benedetto, A., Loizos, A., Slob, E.C., and Tosti, F., COST Action TU1208 "Civil Engineering Applications of Ground Penetrating Radar: first-year activities and results", Geophysical Research Abstracts Vol. 16, EGU2014-16933, 2014 EGU General Assembly 2014.

- Tosti, F., Benedetto, A., and Calvi, A., Efficient air-launched ground-penetrating radar inspections in a large-scale road network. Proceedings of the 3rd International Conference on Transportation Infrastructure, Pisa, Italy, 22-25 April 2014.

- Umiliaco, A., Benedetto, A., and Tosti, F., Prediction of hydraulic and acoustic properties of open-graded mixes. Proceedings of the 3rd International Conference on Transportation Infrastructure, Pisa, Italy, 22-25 April 2014.

- Tosti, F., Benedetto, A., and Calvi, A., An effective approach for road maintenance through the simulation of GPR-based pavements damage inspection. Proceedings of the 2013 International Journal of Pavements Conference, São Paulo, SP, Brazil, 09-10 December 2013. 2013 IJPC Paper 124-1, pp. 1-9.

- Tosti, F., and Umiliaco, A., Preventing the risk of accidents through the simulation of GPR-based pavements damage inspection. Proceedings of the Road Safety and Simulation International Conference, Rome, Italy, 23-25 October 2013, pp. 243. ISBN: 978-88-548-6415-3.

- Umiliaco, A., and Tosti, F., A simulation approach to prevent the hydroplaning risk. Proceedings of the Road Safety and Simulation International Conference, Rome, Italy, 23-25 October 2013, pp. 244. ISBN: 978-88-548-6415-3.

- Tosti, F., Determination, by using gpr, of the volumetric water content in structures, substructures, foundations and soil. State of the art and open issues. Proceedings of the 1st COST Action General Meeting TU1208, Rome, Italy, 22-24 July 2013, pp. 99-105. ISBN: 978-88-548-6190-9.

- Benedetto, A., Tosti, F., Ortuani, B., Giudici, M., and Mele, M. Soil

moisture mapping using GPR for pavement applications. Proceedings of the 7th International Workshop on Advanced Ground Penetrating Radar 2013, Nantes, France, 02-05 July 2013, pp. 243-248. IEEE Digital Object Identifier: 10.1109/IWAGPR.2013.6601550, pp. 1-5.

- Ortuani, B., Benedetto, A., Giudici, M., Mele, M., and Tosti, F., A non-invasive approach to monitor variability of soil water content with electromagnetic methods. Proceedings of the International conference on: Four Decades of Progress in Monitoring and Modeling of Processes in the Soil-Plant-Atmosphere System: Applications and Challenges, Naples, Italy, 19-20 June 2013. Procedia Environmental Sciences, Vol. 19, pp. 446-55.

- Benedetto, A., and Tosti, F., Inferring bearing ratio of unbound materials from dielectric properties using GPR: the case of Runaway Safety Areas. Proceedings of the 2013 Airfield and Highway Pavement Conference, Los Angeles, CA (USA), 9-12 June 2013. pp. 1336-1347. doi: 10.1061/9780784413005.113.

- Tosti F., Patriarca C., Slob E.C., Benedetto A., and Lambot S., Evaluation of clay content in soils for pavement engineering applications using GPR, Geophysical Research Abstracts Vol. 15, EGU2013-12272, 2013 EGU General Assembly 2013.

- Benedetto, A., D'Amico, F., and Tosti, F., GPR-based evaluation of strength properties of unbound pavement material from electrical characteristics, Geophysical Research Abstracts Vol. 15, EGU2013-3648, 2013 EGU General Assembly 2013.

- Pajewski, L., Benedetto, A., Loizos, A., Slob, E.C., and Tosti, F., Civil Engineering Applications of ground Penetrating Radar: Research Perspectives in COST Action TU1208, Geophysical Research Abstracts Vol. 15, EGU2013-13941, 2013 EGU General Assembly 2013.

- Tosti, F., and Benedetto, A., Pavement pumping prediction using Ground Penetrating Radar. Proceedings of the 5th International Congress on Sustainability of Road Infrastructures SIIV 2012,

Rome, Italy, 29-31 October 2012. Procedia - Social and Behavioral Sciences, Vol. 53, pp. 1045-1054.

- Tosti, F., and Patriarca, C., Time and frequency GPR waveforms analysis for clay content evaluation in soils, Geophysical Research Abstracts Vol. 14, EGU2012-7780, 2012 EGU General Assembly 2012.

- Benedetto, A., Tosti, F., Schettini, G., and Twizere, C., Evaluation of geotechnical stability of road using GPR. Proceedings of the 6th International Workshop on Advanced Ground Penetrating Radar 2011, Aachen, Germany, 22-24 June 2011. IEEE Digital Object Identifier: 10.1109/IWAGPR.2011.5963858, pp. 1-6.

- Tosti, F., and Twizere, C., Potentiality of GPR for evaluation of clay content in soils, Geophysical Research Abstracts Vol. 13, EGU2011-7864, 2011 EGU General Assembly 2011.

Accepted for publication

- Tosti, F., Adabi, S., Pajewski, L., Schettini, G., and Benedetto, A., Large-scale analysis of dielectric and mechanical properties of pavement using GPR and LFWD, Proceeding of the 15th International Conference on Ground Penetrating Radar, Bruxelles, Belgium, June 30–July 4, 2014.

- Benedetto, A, Tosti, F., Pajewski, L., D'Amico, F., and Kusayanagi, W., FDTD Simulation of the GPR Signal for Effective Inspection of Pavement Damages, Proceeding of the 15th International Conference on Ground Penetrating Radar, Bruxelles, Belgium, June 30–July 4, 2014.

Book publications

- Tosti, F., Slob, E.C., Determination, by using gpr, of the volumetric water content in structures, substructures, foundations and soil. In. "Civil Engineering applications of Ground Penetrating Radar", Springer ed. (In press).

National journal publications

- Benedetto, A., Tosti, F., Di Domenico, L., Il dominio di significatività con il Light Falling Weight Deflectometer, *Strade e Autostrade*, **89** (5) (2011), 152–157. ISSN: 1723-2155

- Benedetto, A., Tosti, F., L'uso del Georadar per lo Studio delle instabilità della sovrastruttura e del corpo stradale, *Strade e Autostrade*, **84** (6) (2010), 155–160. ISSN: 1723-2155

Acknowledgements

In this thesis, I present some of the research results obtained in the framework of my PhD career.
I would firstly like to thank my supervisor Prof. Dr. Andrea Benedetto for introducing me on GPR and for his continual support, guidance, and encouragements throughout the duration of my studies. It was a great pleasure to learn about scientific topics, method, discipline, and human relations, that will be definitely something to be treasured for the future.
Many of the results described in this thesis would have not been possible without the fundamental help and technical assistance of Spartaco Cera. I would also thank Spartaco for creating a supportive environment for my research, and for the enjoyable time during laboratory experiments, fieldwork, lunch and coffee breaks.
I am very grateful to Dr. Alessandro Calvi and Dr. Fabrizio D'Amico who were always available to give me advice and guidance when I needed it. Many thanks also to Prof. Dr. Maria Rosaria De Blasiis and Prof. Dr. Francesco Bella for welcoming me over these three years within the research group of Road Infrastructure Engineering.
Thanks are expressed to Dr. Lara Pajewski for giving me an important role within the framework of COST Action TU1208.
I would like to single out the collaboration with Prof. Dr. Evert Slob who welcomed me in the Netherlands in 2011 and 2012, and stimulated my interest in electromagnetic geophysics. Those periods in TUDelft were very important for my personal enriching, since I could learn about science, international cultures of colleagues worldwide, and treasuring the efficiency of a lovely “cycling” country.
Thanks are expressed to my TUDelft colleagues for the unforgettable time spent together during lunch, coffee break and trips: Alex, Andrea, Andreas, Asiya, Carlos, Claudio, Michel, Niels, Panos.
Particular thanks go to Niels Grobbe and Carlos Almagro-Vidal for their hospitality and friendliness. My personal gratitude goes to Claudio Patriarca, which was fundamental for me during the time in the Netherlands. He introduced me to other colleagues, helped me with the hard work in laboratory, and was really patient in answering all my questions about new EM theory.

I also wish to thank Dr. Karl-Heinz Wolf for the permission to use the laboratory sites, as well as Ing. Karel Heller and Ing. Wim Verwaal for helping me with the equipment and installation of the set-up.
I would like to thank my external examiners, Prof. Dr. Amir Morteza Alani, Prof. Dr. Andreas Loizos that, together with mentioned Prof. Dr. Evert Slob, have agreed to embark on the task of evaluating the work presented in this document.
Finally, I wish to express my gratitude to my family, my father, my sister, Erica, and all my relatives from Umbria for helping me. Mostly, I owe a lot to Erica. When I look back to these three years, it would be hard to think that I could do all this without you. Thank you for introducing me to your joyful family, for believing in me unconditionally, for your patience and your support during hard times, that made me hope, and make me hope for a better future now, to spend together.